1996

Electromagnetic dissociation of Co and Au targets by a 10.2 GeV/nucleon Au beam

Lars Albert Ewell
Iowa State University

INFORMATION TO USERS

This manuscript has been reproduced from the microfilm master. UMI films the text directly from the original or copy submitted. Thus, some thesis and dissertation copies are in typewriter face, while others may be from any type of computer printer.

The quality of this reproduction is dependent upon the quality of the copy submitted. Broken or indistinct print, colored or poor quality illustrations and photographs, print bleedthrough, substandard margins, and improper alignment can adversely affect reproduction.

In the unlikely event that the author did not send UMI a complete manuscript and there are missing pages, these will be noted. Also, if unauthorized copyright material had to be removed, a note will indicate the deletion.

Oversize materials (e.g., maps, drawings, charts) are reproduced by sectioning the original, beginning at the upper left-hand corner and continuing from left to right in equal sections with small overlaps. Each original is also photographed in one exposure and is included in reduced form at the back of the book.

Photographs included in the original manuscript have been reproduced xerographically in this copy. Higher quality 6" x 9" black and white photographic prints are available for any photographs or illustrations appearing in this copy for an additional charge. Contact UMI directly to order.

UMI

A Bell & Howell Information Company
300 North Zeeb Road, Ann Arbor MI 48106-1346 USA
313/761-4700 800/521-0600

Electromagnetic dissociation of Co and Au targets by a 10.2 GeV/nucleon Au beam

by

Lars Albert Ewell

A Dissertation Submitted to the

Graduate Faculty in Partial Fulfillment of the

Requirements for the Degree of

DOCTOR OF PHILOSOPHY

Department: Physics and Astronomy
Major: Nuclear Physics

Approved:

Signature was redacted for privacy.

In Charge of Major Work

Signature was redacted for privacy.

For the Major Department

Signature was redacted for privacy.

For the Graduate College

Iowa State University
Ames, Iowa
1996

TABLE OF CONTENTS

CHAPTER 1. INTRODUCTION 1

Relativistic Heavy Ion Collisions 1

Practical Applications 2

CHAPTER 2. THEORY 4

Atomic 4

Nuclear 5

Electromagnetic Fields 5

Frequency Spectrum 10

Impact Parameter 13

Real - Virtual Photons 13

Real Photonuclear Cross Sections 14

On Multipoles 14

CHAPTER 3. BACKGROUND 17

Bevalac 17

Multiple Excitations 18

CHAPTER 4. EXPERIMENT 20

Description 20

Beam Monitoring 23

Target Counting 34

CHAPTER 5. DATA ANALYSIS 41

Computer Programs 41

Gamma-Ray Spectra 45

Corrections 52

CHAPTER 6. RESULTS 63

Cross Sections 63

Error Analysis 68

Interpretations 76

CHAPTER 7. TESTING OF LATE ENERGY TRIGGER BOARDS FOR STRANGELET SEARCH EXPERIMENT E864 83

Introduction to Strange Matter 83

Experiment E864 86

Late Energy Trigger (LET) 88

LET Board Testing 89

Test Setup 89

Impedance Matching 93

Triggering/Timing 96

Initial Board Inspection 98

Data Taking 100

Testing Results 102

Board Troubleshooting 107

Conclusion 108

BIBLIOGRAPHY 109

ABSTRACT

Collisions of relativistic heavy ions (RHI) can be broadly categorized as two types: central (nuclear force dominated) and peripheral (coulomb force dominated). The experiment described addresses the latter. Unlike the neutron removal cross section via the nuclear force σ_{nucl}, the neutron removal cross section via the coulomb force σ_{coul} is an increasing function of energy due to the Lorentz contraction of the electromagnetic fields. As more energetic and heavier (higher Z) RHI beams have become available, there appears to be an overestimation of the one neutron removal cross section by the virtual photon theoretical treatment of Weizsäcker, Williams and Fermi (WWF). An experiment was performed at the AGS at BNL using a 10.2 GeV/nucleon Au beam in order to determine the behavior of the phenomena referred to as Electromagnetic Dissociation (ED). Au and Co targets were irradiated, after which the yield of one and two neutron removal from Au and Co along with other isotopes was determined using gamma ray spectroscopy.

In addition, a testing program to evaluate the performance of a group of custom made circuit boards for use in the Late Energy Trigger (LET) in a strange matter search experiment (E864) will be described in Chapter 7.

CHAPTER 1. INTRODUCTION

Relativistic Heavy Ion Collisions

When two relativistic heavy ions (RHI's) "collide", there are a variety of possible outcomes. If they collide at a small impact parameter ($b \leq 7$ fm), among the physical processes possible are collective flow of nuclear matter, the formation of strange matter or the formation of a quark gluon plasma, depending upon the collision energy. This thesis will be concerned with collisions where the impact parameter is larger than the range of the nuclear forces. This is about 15 fm for Au and 13 fm for Co. In these peripheral collisions, among the physical processes possible are Electromagnetic Dissociation (ED) of the target and/or projectile nucleus, e^+e^- creation, or individual nucleonic excitation again depending upon the collision energy. This thesis will concentrate on the first of these phenomena, ED.

Two things characteristic of the RHI beam used to conduct these experiments are responsible for the prominent role that ED plays in these collisions. They are: 1) The high charge, Z=79, of the Au projectiles. 2) The extreme Lorentz contraction of the electric field of the Au projectile due to the high energy, E=10.2 GeV/nucleon, to which the projectiles are accelerated. While a proton beam would produce negligible ED (no measured effects) at available energies, beams of light nuclei do exhibit small, but not negligible, ED cross sections at energies above approximately 1

GeV/nucleon. The above discussion applies to stable nuclei. Indeed, ^{11}Li has significant ED cross sections (1.72 $\pm$ 0.65 b) at energies somewhat below 1 GeV/nucleon (0.8 GeV/nucleon). [1, 2]

Practical Applications

While the intrinsic interest is the most compelling reason to study ED phenomena, it is not the only one. There are practical applications of the knowledge gained in ED experiments. One application has to do with colliding beam accelerators. While relativistic heavy ion colliders ostensibly have as their main focus the study of central collisions, when two RHI beams cross, central collisions will be a relatively rare event. Since the cross section for ED processes is an increasing function of energy, at very high energies these processes will dominate. If a large extrapolation is made from the fixed target experiments to be discussed here (10 GeV/nucleon) to the planned energies (100 GeV/nucleon) of the Relativistic Heavy Ion Collider (RHIC), the cross sections for one neutron removal, for example, are on the order of 50 barns. Since any nucleus with a neutron removed will no longer have the proper acceleration due to the mass change, the measurements to be discussed are of obvious relevance. Another area in which ED has practical applications is related to astrophysics.

Using the concept of the WWF theory referred to above, the Lorentz contracted fields of the projectile nuclei can be thought of as a source of energetic pulsed

---

[1] J.P. Dufour *et al.*, p321 *Proceedings of The First International Conference of Radioactive Nuclear Beams, 16-18 Oct. 1989* Teaneck N.J.: World Scientific Publishing Co., 1990.

[2] T. Kobayashi, p325 *Proceedings of The First International Conference of Radioactive Nuclear Beams, 16-18 Oct. 1989* Teaneck N.J.: World Scientific Publishing Co., 1990.

photons in the lab frame. These energetic photons can be exploited to determine cross sections of astrophysical interest. As an example consider the reaction

$$\alpha + d \rightarrow {}^{6}Li + \gamma.$$

In the interior of a star, the temperature as well as the gravitational pressure combine to facilitate the reaction. However, since the cross-section for the $\alpha + d$ reaction in typical stellar processes is very low, the study of this reaction in any earth-bound laboratory is difficult. If the reverse reaction is considered

$${}^{6}Li + \gamma \rightarrow d + \alpha$$

one can see that ED can be useful. This is merely the coulomb induced (ED) break-up of a ^{6}Li atom. By use of the detailed balance theorem, one can relate the cross-section for ED of the Li nucleus to the deuteron-alpha capture cross-section.[3]

[3]C. Bertulani and G. Baur, *Physics Today*, **47**, 22 (March, 1994)

CHAPTER 2. THEORY

Atomic

The WWF theory of virtual quanta was pioneered by Fermi in 1924[4] and refined quantum mechanically ten years later independently by Weizsäcker and Williams.[5] In 1924 Fermi was attempting to relate the energy loss in the ionization of atoms to the absorption of (virtual) X-rays. Regarding this initial use of the concept of virtual quanta, consider a beam of particles of charge Ze (atomic ions) with kinetic energy 50 keV "colliding" with hydrogen atom targets. The collisions can be divided into two types: 1) Close - where the projectile passes through the target atom. 2) Distant - where the projectile passes outside of the target atom. In the distant collisions (type 2), the ionization of the target atom can be viewed as the photoelectric effect with the (virtual) photons supplied by the fields of the projectile. Using this model, Fermi found that although type 2 collisions happen much more frequently, type 1 collisions involve a much larger amount of energy transferred so that the total amount of energy transferred is approximately divided equally between the two types.

---

[4]E. Fermi, Zeit. Physik., **29**, 315 (1924).

[5]E. J. Williams, Proc. Roy. Soc., **A139**, 163 (1933).

Nuclear

Regarding the current RHI experiments, the WWF applies in much the same way. The differences are: 1) The distance scale is now nuclear dimensions (10^{-15}m) as opposed to atomic dimensions (10^{-10}m). 2) The energy scale requires virtual gamma ray photons as opposed to X-ray photons. 3) The reactions of interest are mainly one and two neutron removal as opposed to atomic ionization (electron removal).

The essence of the WWF approach is to exploit the similarity between the Lorentz contracted electric field of the projectile and a pulse of highly energetic real photons as seen by the target nucleus. In the course of implementing this method, many questions arise. Among them are: 1) What energy photons should be used? 2) How many photons should be used? 3) Where is the semi-classical/quantum distinction made? 4) What approximations are used in deriving the radiation (photon) fields? A natural place to start is the last question.

Electromagnetic Fields

In Fig. 2.1, we see the "collision" of two RHIs at an impact parameter b. The following follows closely the work of Jackson.[6] In Fig. 2.1(a) we see that the electric field of the projectile nucleus is Lorentz contracted. This results in the relatively large longitudinal pulse P_1 and the relatively small transverse pulse P_2 of equivalent radiation as can be seen in Fig. 2.1(b). It is important to note that the choice of the target reference frame is an arbitrary one. The first approximation used

[6] J.D. Jackson, *Classical Electrodynamics* chps. 11, 13, 14, 15, New York, John Wiley & Sons 1987.

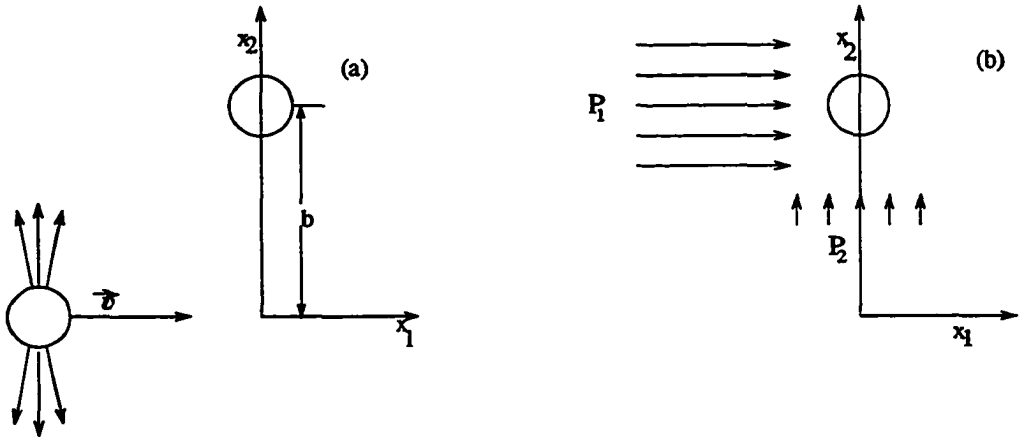

FIG. 2.1. (a) RHIC at impact parameter b. (b) Equivalent pulses of radiation.

to calculate the equivalent radiation fields of the projectile will be to assume that both the target and projectile nuclei behave as point-like particles. Assuming that the target is point-like necessitates the calculation of the projectile fields at just one point. This assumption is similar to the dipole approximation used in atomic physics in which the wavelength of the electromagnetic radiation is much larger than the size of the system which emits/absorbs it. The crucial point is that the electric field at a given time has a constant value for the area (point) under consideration. With this assumption, we have a situation described by Fig. 2.2.

In Fig. 2.2, the primed coordinate system is traveling along with the speed of the projectile, v, in the direction of the x_1' axis which is collinear with the x_1 axis. The unprimed coordinate system is at rest in the lab frame with the target. As can be seen in the figure, the distance of closest approach between the target and the projectile is b. We choose this to occur at time t=t'=0. In the primed system we

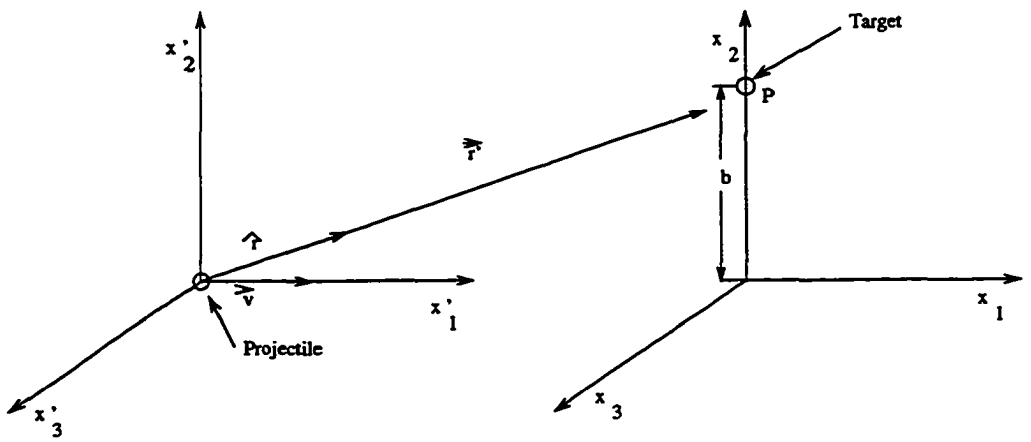

FIG 2.2. Coordinate System for RHIC

have for the electric field

$$\begin{aligned} \mathbf{E}' &= \frac{Ze\hat{r'}}{r'^2} \\ &= \frac{Ze}{r'^2}\left(\frac{vt'\hat{x_1'} + b\hat{x_2'}}{((vt')^2+b^2)^{1/2}}\right) \end{aligned}$$

since

$$r' = \sqrt{(vt')^2+b^2}$$

and

$$\begin{aligned} \hat{r'} &= \frac{\mathbf{r}'}{|\mathbf{r}'|} \\ &= \frac{vt'\hat{x_1'} + b\hat{x_2'}}{\sqrt{(vt')^2+b^2}}. \end{aligned}$$

So we have for the electric field components

$$\begin{aligned} E_1' &= \frac{Zevt'}{r'^3} \\ &= \frac{Zevt'}{((vt')^2+b^2)^{3/2}} \end{aligned}$$

$$
\begin{aligned}
E_2' &= \frac{Zeb}{r'^3} \\
&= \frac{Zeb}{((vt')^2 + b^2)^{3/2}} \\
E_3' &= 0.
\end{aligned}
$$

We are interested in the fields in the stationary lab frame due to the moving projectile. We now make the approximation that the projectile undergoes *no* acceleration in the coulomb collision with the target nucleus. With this approximation, we can calculate the electric and magnetic fields in the lab frame by simply applying the Lorentz transformations to the primed fields (note: for brevity and simplicity, we concentrate on just the electric fields here). With the four vector notation $x_0' = ct, x_1 = x$ *etc.* and the dynamics of Fig. 2.2. we have for the Lorentz transformations

$$
\begin{aligned}
x_0' &= \gamma(x_0 - \beta x_1) \\
x_1' &= \gamma(x_1 - \beta x_0) \\
x_2' &= x_2 \\
x_3' &= x_3
\end{aligned}
$$

with $\beta = v/c$ and $\gamma = 1/\sqrt{1-\beta^2}$. Looking at the equations for E_1' and E_2', we see that t' is the only coordinate that needs to be transformed. From the Lorentz transformations we see that $ct' = \gamma(ct - \beta x_1)$ but $x_1 = 0$ at the point of observation P, so that $ct' = \gamma ct$ or $t' = \gamma t$. Substituting this back into the expressions for the electric fields gives

$$
E_1' = \frac{Zev\gamma t}{((v\gamma t)^2 + b^2)^{3/2}}
$$

and

$$E_2' = \frac{Zeb}{((v\gamma t)^2 + b^2)^{3/2}}$$

Finally, there are the Lorentz transformations of the electric and magnetic fields themselves

$$\begin{aligned} E_1 &= E_1' \\ E_2 &= \gamma E_2' \\ B_3 &= \gamma\beta E_2' \end{aligned}$$

which gives for the fields in the unprimed frame

$$\begin{aligned} E_1(t) &= \frac{-Ze\gamma vt}{(b^2 + \gamma^2 v^2 t^2)^{3/2}} \\ E_2(t) &= \frac{Ze\gamma b}{(b^2 + \gamma^2 v^2 t^2)^{3/2}} \\ B_3(t) &= \beta E_2(t). \end{aligned}$$

It is worthwhile to graph the field components at different velocities. In Fig. 2.3(a) and 2.3(b) we see the components E_2 and E_1 respectively at relativistic and non-relativistic velocities. We see that for relativistic particles ($\beta \approx 1$) that E_2 and B_3 (βE_3) are indistinguishable from a pulse of plane polarized radiation (acceleration field) propagating in the x_1 direction. They are mutually perpendicular and also perpendicular to the direction of propagation (x_1). To form the transverse pulse P_2, an additional magnetic field is necessary. However, due to the Lorentz contraction of the static fields, the transverse pulse will make a negligible contribution to the energy. That this is true can be seen by comparing the amplitude of the longitudinal and transverse pulses. The longitudinal pulse (transverse field) has an amplitude proportional to γ while the amplitude of the transverse pulse is constant with respect

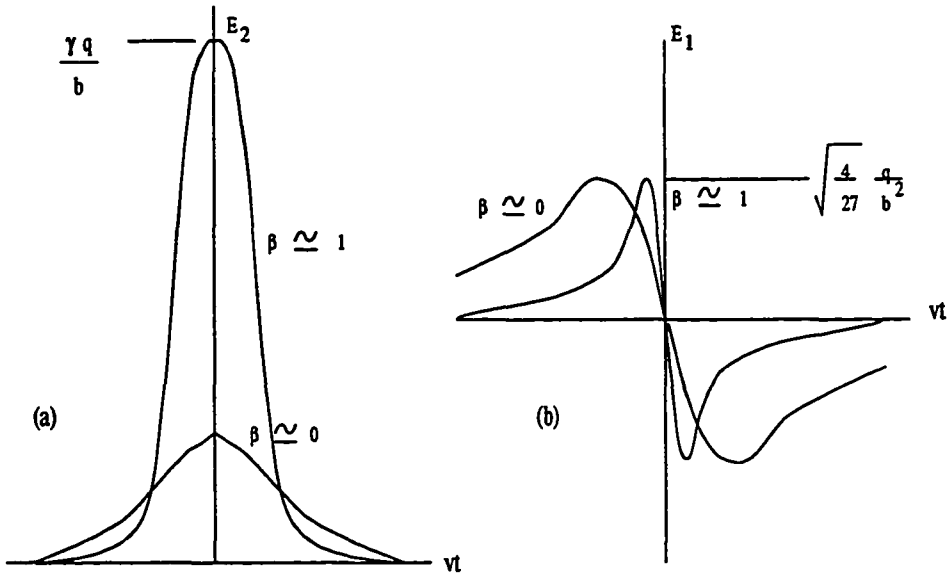

FIG. 2.3. (a) E_2 at target nucleus. (b) E_1 at target nucleus.

to projectile velocity. Therefore at high velocities ($\gamma \gg 1$) the longitudinal pulse will dominate .

Frequency Spectrum

We now see how the velocity fields of the projectile can be represented by a pulse of radiation at the target (and visa versa). This facilitates the implementation of the WWF method which states that

$$\sigma = \int \sigma(\omega) n(\omega) d(\omega)$$

where $n(\omega)$ is the virtual photon spectrum and $\sigma(\omega)$ are the empirically measured cross sections of interest. To calculate the frequency spectrum of the virtual photon fields we take the Fourier transform of the transverse field $E_2(t)$

$$E_2(\omega) = \frac{1}{\sqrt{2\pi}} \int_{-\infty}^{\infty} E_2(t) e^{i\omega t} dt$$

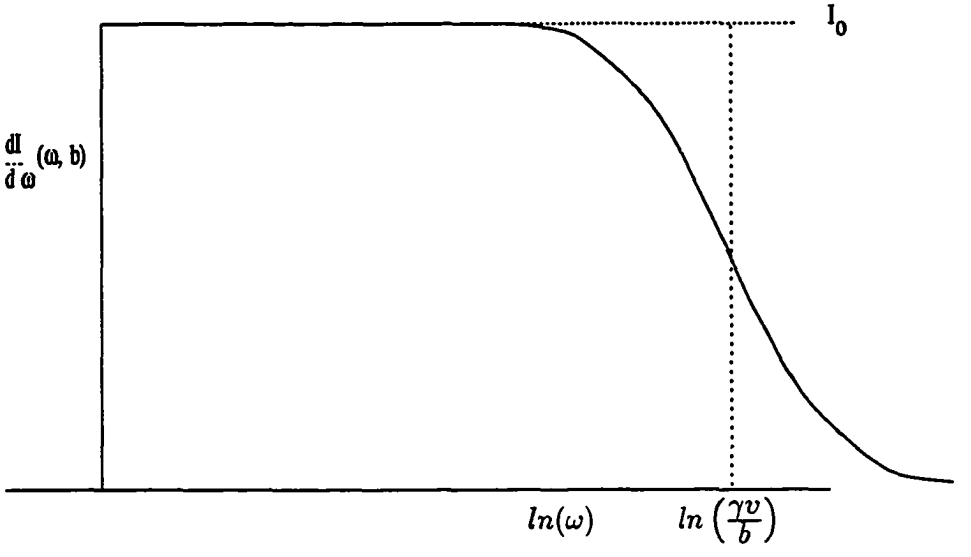

FIG. 2.4. Frequency spectrum for virtual photon fields with $I_0 = \frac{q^2}{\pi^2 c}\left(\frac{1}{\beta}\right)^2 \frac{1}{b^2}$.

$$= \frac{Ze\gamma b}{\sqrt{2\pi}} \int_{-\infty}^{\infty} \frac{e^{i\omega t}}{(b^2 + \gamma^2 v^2 t^2)^{3/2}} dt$$
$$= \frac{Ze}{bv}\left[\frac{2}{\pi}\right]^{1/2}\left[\frac{\omega b}{\gamma v} K_1\left(\frac{\omega b}{\gamma v}\right)\right]$$

where K_1 is a modified Bessel Function of the second kind. From the value of $E_2(\omega)$ we can find the frequency spectrum since

$$\frac{dI_1}{d\omega}(w, b) = \frac{c}{2\pi}|E_2(\omega)|^2$$
$$= \frac{q^2}{\pi^2 c b^2}\frac{1}{\beta^2}\left(\frac{\omega b}{\gamma v}\right)^2 K_1^2\left(\frac{\omega b}{\gamma v}\right)$$

where the subscript 1 on I indicates that this frequency spectrum is associated with the longitudinal pulse P_1 (see Fig. 2.1b). In Fig. 2.4 we see a plot of the frequency spectrum. From this figure, we can see that, at a given impact parameter b, for frequencies up to approximately $\omega = (\frac{\gamma v}{b})$ that there is an equal distribution of

energy between frequencies and that for frequencies greater than this the contribution begins to fall off. There are two things to consider when interpreting this graph: 1) This gives the behavior of the frequency distribution at only *one* impact parameter. To get a more complete picture, an integration over all possible impact parameters is required. 2) This virtual photon spectra is multiplied by an *empircally* determined real energy dependent photonuclear cross section and then integrated over frequencies to determine the WWF cross section. It is worthwhile to get an estimate of the frequency cut off. We make the assumption that $\gamma = 10$ (since E/nucleon $\approx$ 10 GeV). We then have that

$$1 - \beta^2 = 1/100 \rightarrow v = 0.99c.$$

If we choose an impact parameter of b=15fm we have for a frequency cut-off

$$\begin{aligned} \omega &= \frac{\gamma v}{b} \\ &= \frac{10 \times (0.99 \times 3.0 \times 10^8 m/s)}{15 \times 10^{-15} m} \\ &= 2.0 \times 10^{23} Hz \end{aligned}$$

or

$$\begin{aligned} E_{photon} &= \hbar\omega \\ &= (6.582 \times 10^{-16} eV \cdot s)(2.0 \times 10^{23} Hz) \\ &= 131 MeV \end{aligned}$$

or a cut off of approximately 130 MeV for the virtual photons.

Impact Parameter

To determine the virtual photon spectra we need to integrate over all possible impact parameters. The critical part of this integration is the choice of minimum impact parameter. The minimum impact parameter cannot be less than the distance at which the nuclear force predominates. This distance will be discussed in more detail in the results chapter. The choice of minimum impact parameter is related to the semi-classical nature of the approximation since specifying a minimum impact parameter necessarily locates the projectile exactly with respect to the target. If one speaks of momentum transfer as opposed to minimum impact parameter, the relationship between the two is via the uncertainty relationship

$$i.e.\ b_{min} = \frac{\hbar}{Q_{max}}$$

with Q_{max} being the maximum momentum transferred.

If an integration over impact parameters is performed the result obtained for the frequency spectrum of virtual photons is

$$\frac{dN(\omega)}{d\omega} = \frac{2}{\pi}\frac{q^2}{c}\left(\frac{1}{\beta}\right)^2 (xK_0(x)K_1(x) - \frac{v^2}{2c^2}x^2(K_1^2(x) - K_0^2(x)))$$

where $x = \frac{\omega b_{min}}{\gamma v}$. We will see the sensitivity of this function to minimum impact parameter when investigating the WWF predictions.

Real - Virtual Photons

The use of the term "virtual photons" has been widespread for many years. It is important not to confuse the context in which the term virtual is used. In the context of QED, a real photon is transverse, has only two polarizations and has zero

rest mass. A virtual photon, on the other hand can have four states of polarization. This is a different meaning than is used here in the WWF approximation. In the context of the WWF method, the term virtual refers to the fact that the static coulomb interaction (velocity fields) of the RHI is replaced by a pulse of "real" photons (acceleration fields). In this approximation, there is no sum over polarizations and the QED distinction between real and virtual photons is not considered. In the context of QED, the photons that represent the coulomb interaction are virtual and the pulse that they are replaced by (in the context of the WWF method) is real.

Real Photonuclear Cross Sections

As referred to earlier, an empirically determined real photon cross section is folded into the calculation of the WWF cross-section. An example of the energy dependence of a real photonuclear cross section can be seen in Fig. 2.5. [7]

On Multipoles

In the interaction of the "virtual" radiation field of the projectile nucleus with the target nucleus, the term "multipole" can be used in more than one context. In an attempt to clarify which phenomena is being described, a distinction needs to be made between a nuclear multipole transition and multipole radiation.

There are two general categories of electric nuclear multipole transitions and resonances; isovector and isoscalar. In an isovector resonance, the protons in a nucleus can be thought to oscillate against the neutrons whereas in an isoscalar resonance the nucleus vibrates en masse with no distinction between protons and

[7] A. Veyssière *et al.*, Nucl. Phys. , **A159** 561 (1970).

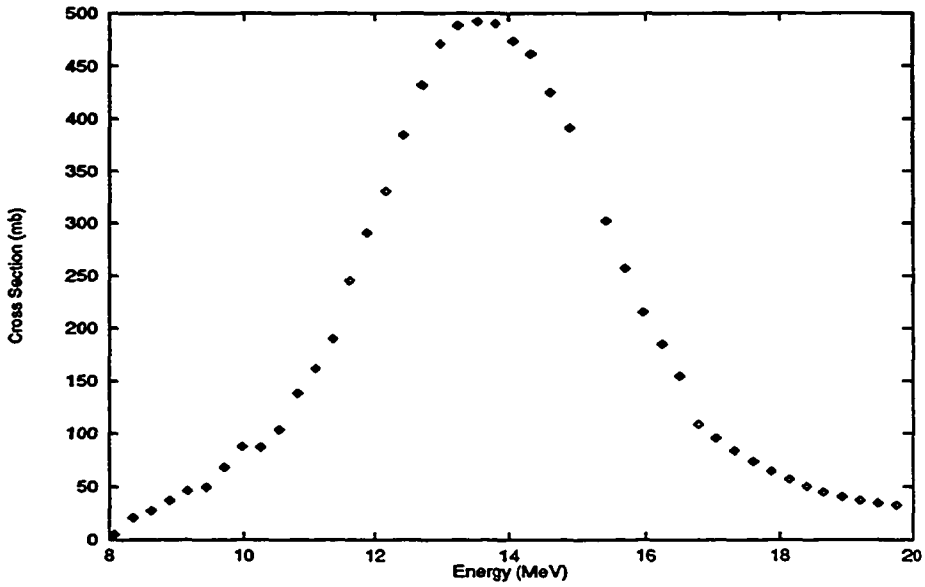

FIG. 2.5. Measured photonuclear cross sections for ^{197}Au, $\sigma(\gamma, n)$.

neutrons. It has been empirically well established that the energy at maximum intensity associated with the so-called giant dipole (isovector) resonance (GDR) follows the formula[8]

$$E = 77(A)^{-1/3} \ MeV.$$

This gives a value for Au of

$$E = 13.2 \ MeV.$$

It is predominantly this resonance in the target nucleus that is excited by the Lorentz contracted electric field of the projectile nucleus.

The dipole resonance of a nucleus such as Au can best be dealt with on a purely quantum mechanical basis. The initial state is the unperturbed ground state of the target Au nucleus. The final state is the nucleus undergoing a GDR. The

[8]S. S. Hanna *Proceedings of the Giant Multipole Resonance Topical Conference, 15-17 Oct. 1979, Oak Ridge Tenn.* : Harwood Academic Publishers, New York 1980.

operator which connects these two states is derived from the electromagnetic field of the projectile nucleus. If we assume that the electromagnetic excitation is a pure plane wave, then this operator can be represented by a multipole expansion of the electromagnetic radiation fields with the addition of photon annihilation operators to represent the absorption of the photon. It is beyond the scope of this thesis to derive an accurate representation of this operator. However, it can be said that if the excitation is a pure plane wave, all multipoles will have an equal weight. As can be seen in figure 2.3a, at high velocities/energies, this approximation becomes more accurate. From the Weisskopf estimates[9] it can be seen that an electric dipole transition is the most probable followed by a magnetic dipole (down 10^{-2}) and an electric quadrupole (down 10^{-5}).[10]Once excited, the GDR decays predominantly by neutron emission in heavy nuclei such as Au. The coulomb barrier inhibits the de-excitation by proton emission.

[9]J. M. Blatt and V. F. Weisskopf, *Theoretical Nuclear Physics*, John Wiley & Sons, New York 1952.

[10]K.S. Krane, *Introductory Nuclear Physics*, John Wiley & Sons, New York 1987.

CHAPTER 3. BACKGROUND

Bevalac

ED was first reported by Heckman and Lindstrom in 1976.[11] In their experiment, conducted at the Bevalac, various targets were bombarded with 1.05 GeV/nucleon ^{12}C nuclei and 2.1 GeV/nucleon ^{12}C and ^{16}O nuclei. They observed an enhancement of the fragmentation cross sections of the beam nuclei with increasing target mass number A. They correctly attributed this enhancement to ED of the beam nuclei by the larger electric fields of the larger A target nuclei.

ED of the beam nuclei was again reported by Westfall *et al.*[12] in 1979, and Olsen *et al.*[13] in 1981 in experiments conducted at the Bevalac. In the first of these, a 1.88 GeV/nucleon ^{56}Fe beam was incident on various targets. An enhancement of the one proton removal cross section for the ^{56}Fe beam nuclei was identified as ED. In the second of these, a 1.7 GeV/nucleon beam of ^{18}O nuclei was incident on various targets. An increase by a factor greater than four was observed for the ratio of the cross section of ^{17}O production using a U target to ^{17}O production using a Be target.

---

[11] H.H. Heckman and P.J. Lindstrom, Phys. Rev. Lett. **37**, 56 (1976).

[12] G.D. Westfall *et al.*, Phys. Rev. C **19**, 1309 (1979).

[13] D. Olson *et al.*, Phys. Rev. C24, 1529 (1981).

ED of the target was first reported by Mercier *et al.*[14] in 1984. There have been reported asymmetries in charge pickup cross sections[15] in RHI fixed target experiments, between the target and the beam. This asymmetry was demonstrated by the fact that the charge pickup cross section for moderately relativistic nuclei (0.9 $\leq$ E $\leq$ 2.0 GeV/nucleon) had a stronger dependence on the projectile than on the target. This dependence increases for both heavier target and projectile nuclei. The Z dependence becomes more pronounced as the energy is decreased. In the work of Mercier *et al.*[16] as well as follow up experiments conducted by Hill *et al.*[17], both performed at the Bevalac, targets of ^{59}Co, ^{89}Y and ^{197}Au were bombarded with projectiles ranging from ^{12}C to ^{139}La with energies ranging from 1.26 GeV/nucleon (La) to 2.1 GeV/nucleon (C). In these experiments, the theoretical treatment known as the WWF (see references 4 and 5 in the Theory chapter) method of virtual photons reproduces the data well. However, with larger projectiles such as La there appears to be an over prediction of the cross section for the one neutron removal. A possible explanation of this effect is related to the phenomena of multiple excitations.

Multiple Excitations

In an attempt to account for differences between theory and experiment, several experimenters have used the concept of multiple excitations. Recently Llope and Braun-Munzinger[18] noticed an underprediction of the total excitation cross sec-

[14]M.T. Mercier *et al.*, Phys. Rev. Lett. **52**, 898 (1984).
[15]B. S. Nilsen *et al.*, Phys. Rev. C **50**, 1065 (1994).
[16]M.T. Mercier *et al.*, Phys. Rev. C **33**, 1655 (1986).
[17]J.C. Hill *et al.*, Phys. Rev. Lett. **60**, 999 (1988).
[18]W.J. Llope and P. Braun-Munzinger, Phys. Rev. C.**41**, 2644 (1990).

tion when using just the GDR contribution to the photonuclear part of the WWF prediction. They use a classical harmonic oscillator model to calculate the probability of a multiple excitation occurring in collisions of 14.6 GeV/nucleon ^{28}Si on targets of ^{27}Al, ^{120}Sn and, ^{208}Pb. These predictions are then compared to data obtained from the RHI experiment E814 at the AGS at BNL. They point out that the ratio of cross sections for different targets could be a promising indicator of higher order processes occurring since first order excitations scale like Z_T^2 while nth order processes scale like Z_T^{2n}. Hence a deviation from Z^2 behavior could be taken as an indicator of multiple excitation occurring. The ratio $\sigma(y, Pb)/\sigma(y, Sn)$ for 14.6 GeV/nucleon ^{28}Si was significantly closer to their predictions than was the ratio $\sigma(y, Pb)/\sigma(y, Al)$. They comment that this is probably an indicator of nonelectromagnetic processes occurring in the lighter target.

In a more recent experiment conducted at the SIS heavy ion synchrotron at GSI Darmstadt by Aumann *et al.*, [19] ^{197}Au targets were bombarded with 1.7 Gev/nucleon ^{20}Ne and 1 Gev/nucleon ^{86}Kr, ^{197}Au, and ^{209}Bi. They point out the trend that, for heavy projectiles, the WWF virtual quanta method leads to overpredictions for the 1n out cross sections and to gross underpredictions for the 2n and 3n out cross sections. They note that higher-order GDR excitations lower the predicted 1n out cross-sections (where one photon excitation contributes most) and raise other xn channels in accordance with the above mentioned discrepancy. To account for this effect they introduce a GDR enhancement factor to increase the two phonon component. Using this method, they more accurately predict experimental ED cross sections.

---

[19] T. Aumann *et al.*, Phys. Rev. C.47, 1728 (1993).

CHAPTER 4. EXPERIMENT

Description

The experiments to be discussed were conducted at the Alternating Gradient Synchrotron (AGS) at Brookhaven National Laboratory (BNL) during the spring of 1992 and the fall of 1993. The beam of projectiles used were Au nuclei with an energy of 10.2 GeV/nucleon. The beam was pulsed with a frequency of approximately 0.3 Hz and a pulse length of approximately 1.0 s. The cross section of the beam was approximately 1cm^2 and the spill intensity varied from 4×10^3 to 1×10^6 projectiles. The individual experiments could be broadly categorized as low and high intensity.

In the high intensity irradiation, Au and Co targets were irradiated. In distinction from the low intensity irradiation, the objective here was not to measure as accurately as possible a large (one neutron out from Au) cross section but to measure some relatively small cross sections. Since the cross sections to be measured were relatively small, the beam intensity was chosen to be a relatively large 1×10^6 nuclei/spill.

In the Au high intensity irradiation three 5cm x 5cm Au targets with areal densities of 36 mg/cm^2, 87 mg/cm^2 and 243 mg/cm^2 were placed in the beam line (see Fig. 4.1(a)). Behind the first and third Au targets were placed Al foil targets concentric with and the same size as the Au targets. These Al foil targets acted as

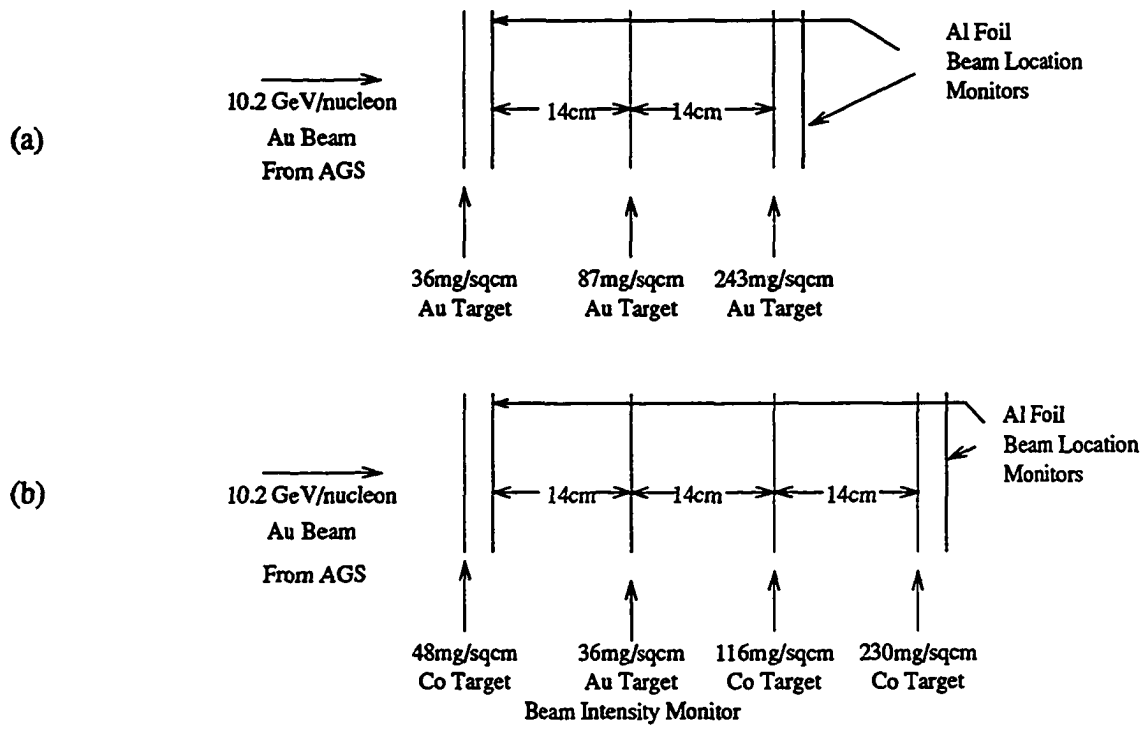

FIG. 4.1. May 1992 high intensity experiment.

Beam Location Monitors (BLMs) as will be explained later. In order to determine the integrated intensity of Au nuclei incident on the targets, the yield of ^{196}Au was determined using gamma-ray spectroscopy on the 36 mg/cm^2 Au target.

The reason for using three different target thicknesses was to be able to determine the correction for secondary reactions. A secondary reaction is defined as one in which the collision is not between an incident projectile and a target nucleus but rather between a fragment from an initial collision from a projectile and a target nucleus. As will be investigated in the data analysis section, the amount of secondary collisions has been found to be a quadratic function of the thickness of the target.

In the Co high intensity irradiation a 48 mg/cm^2, 116 mg/cm^2, and a 230 mg/cm^2 target were placed in the beam line as well as two Al BLMs in much the same fashion as the high intensity Au run (see Fig 4.1(b)). In addition to the above mentioned targets a 36 mg/cm^2 Au target was inserted between two of the Co targets (see Fig. 4.1b) to act as a Beam Intensity Monitor (BIM) not beam *location* monitor.

In the earlier (1992) low intensity irradiation, three 85 mg/cm^2 Au targets were placed in the beam line (see Fig. 4.2). The main objective of this experiment was to measure as accurately as possible the ED cross section for one neutron removal from the targets. The beam intensity was chosen to be a relatively low 4x10^3 nuclei/spill in order to reduce the chance of pileup. The beam intensity was monitored with a two element telescope. The elements of the telescope consisted of a 5 cm x 5 cm scintillator optically coupled to a photomultiplier tube (PMT). The beam position was monitored with a segmented wire ionization chamber (SWIC) approximately five meters downstream from the targets as well as with another Au target foil coincident with the downstream scintillator element. The use of this Au foil beam location monitor (BLM) will be explained in the data analysis section.

For reasons that will be more fully explained later, an additional low intensity run was conducted during Sept 1993. This run was set up similar to the run from May 1992 with some significant differences (see Fig. 4.3). The main difference between the two low intensity runs was that the beam was monitored more accurately in the second run.

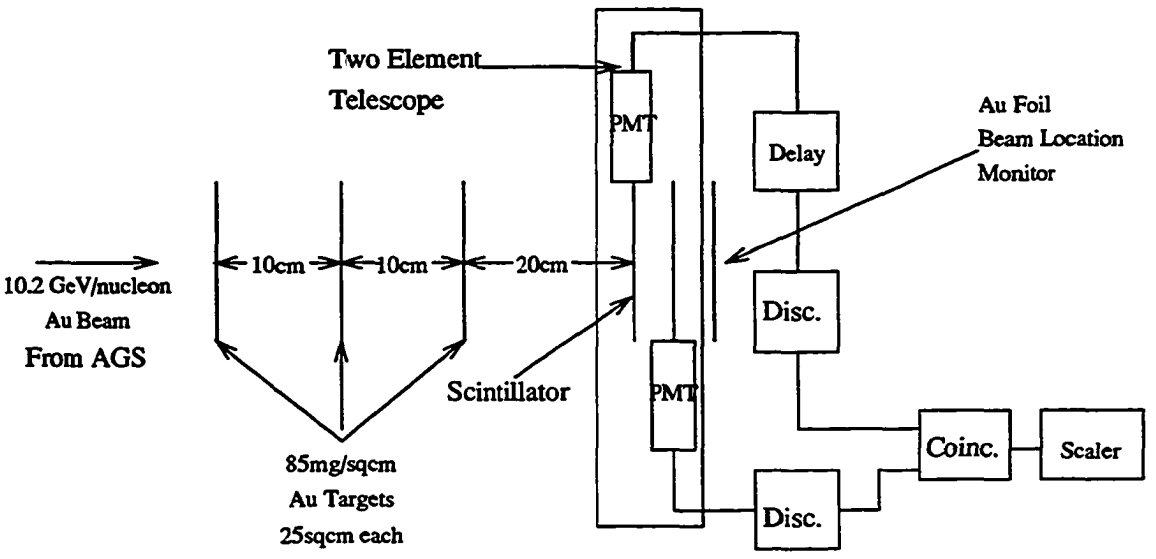

FIG. 4.2. May 1992 low intensity experiment.

Beam Monitoring

Ideally the Au beam traveling in the z direction would have no extent in the x-y plane of the target and could be aimed with infinite precision. In practice, careful attempts must be made to measure the beam size, location and intensity. To this end BLMs, BIMs, a telescope and a UDEW were used to monitor the beam. The operation of these devices will be described in this section starting with how they are used to monitor beam intensity.

In the low intensity runs, of paramount importance was the measurement of beam intensity. As will be shown later, all other measured cross sections were directly determined by the intensity measurements of the low intensity irradiation. Hence the uncertainty in this intensity is a lower limit in other measured cross sections. After the first low intensity run, it was decided that it would be advantageous to be able to

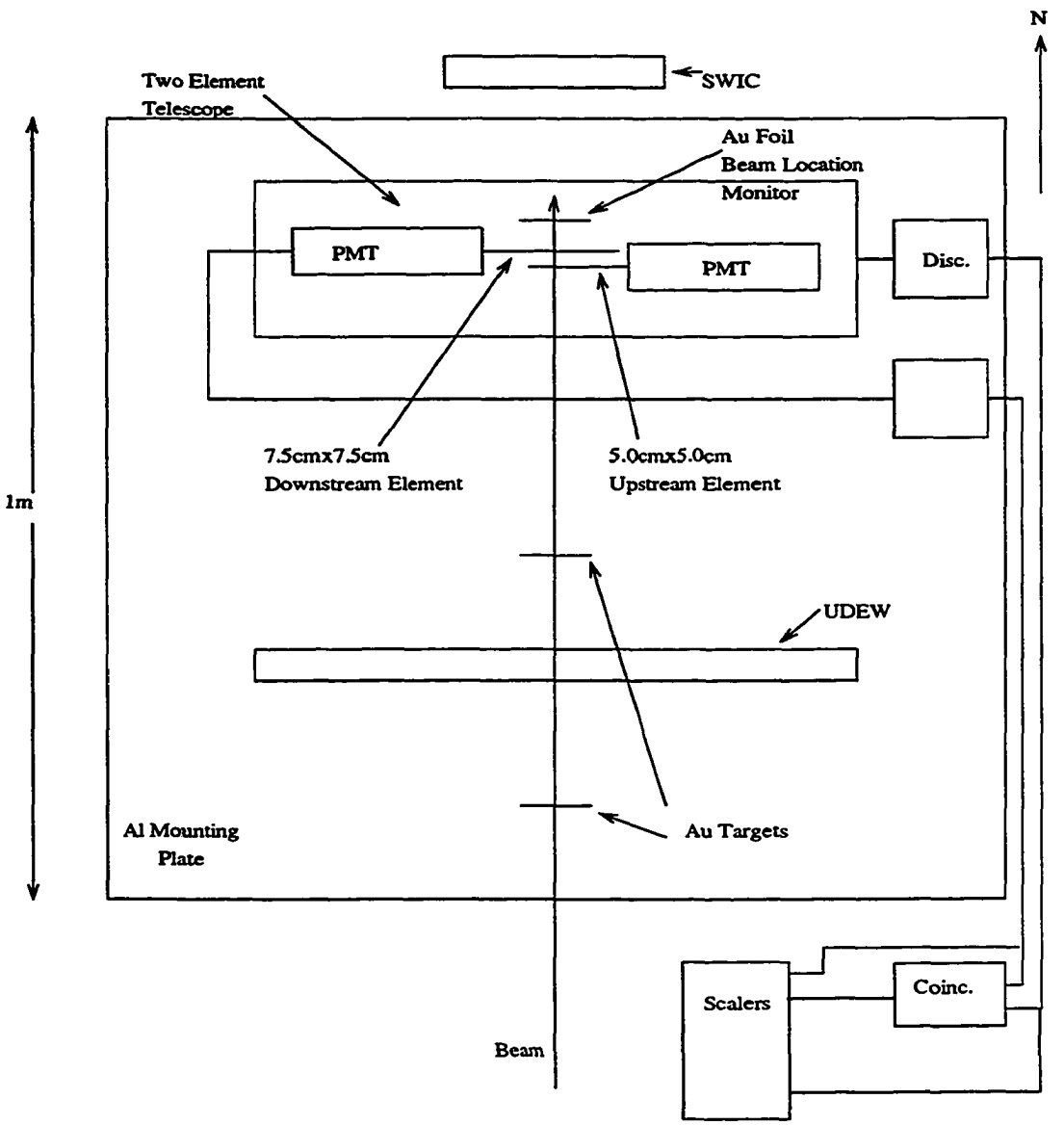

FIG. 4.3. September 1993 low intensity experiment.

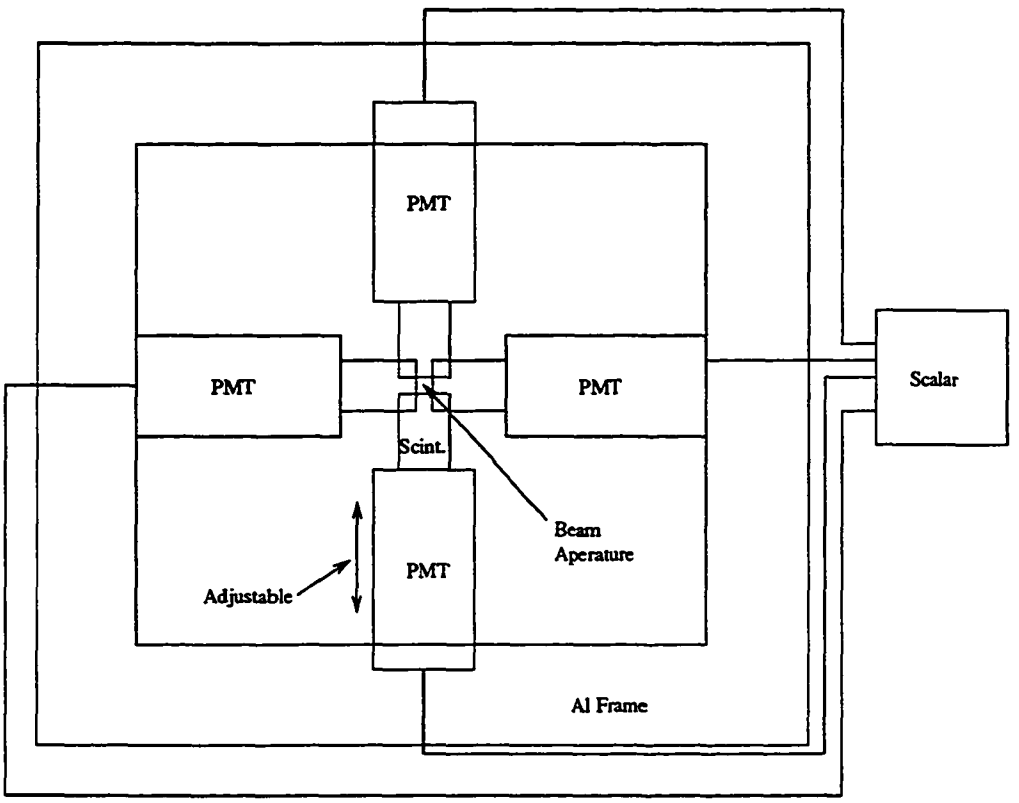

FIG 4.4. UDEW

monitor the position of the beam *while* the experiment was being run. To this end, a device called a UDEW was constructed. UDEW is an acronym for Up Down East West. The UDEW consists of four scintillators coupled to PMT's mounted on an Al frame (see Fig. 4.4). By constructing the UDEW so that the horizontal/vertical position of the PMT's was adjustable, it is possible to create an adjustable aperture through which the beam can be made to pass. If the beam passes "cleanly" through this aperture, i.e. no projectiles hit the scintillators in the UDEW, then the scalars to which the PMT's are connected should in principle read zero. If on the other hand,

a projectile from the beam hits one of the scintillators, then the scalar attached to that scintillator should register and the beam can be adjusted accordingly.

Another difference between the two low intensity experiments was the size of the scintillators used in the telescope. In the first (May 1992) low intensity experiment, the two scintillating elements were of the same area as the Au targets and were concentric with the targets (see Fig. 4.2). In the second (Sept 1993) low intensity experiment, the two scintillating elements were of different size. One had the same area as the Au targets (5cm x 5cm) and was concentric with them. The other was larger in area than the Au targets (7.5cm x 7.5cm) but was also concentric with them (see Fig. 4.3). This asymmetry in the two scintillating sheets allowed the possibility to monitor whether or not the Au beam was hitting the targets. If the beam drifted horizontally or vertically in position so that it was missing the small scintillator, it would still hit the larger scintillator and this fact would represent itself in a larger number of counts registered in the singles rate for the large scintillator. This did not happen.

A more involved difference was related to the thickness of the scintillators in the telescope and the discriminator levels. A projectile nucleus is counted after it passes through each telescope element thereby creating a scintillation flash which the PMT detects and converts into a voltage pulse. The high voltage applied to the PMTs was adjusted to give a one volt pulse for the nominal Au nucleus incident on the scintillators/target (see Fig. 4.5).

A problem can arise due to the interaction of projectile nuclei with the scintillator. Ideally, the electric field of the projectile nuclei will interact with the valence electrons in the plastic scintillator as it passes through each telescope ele-

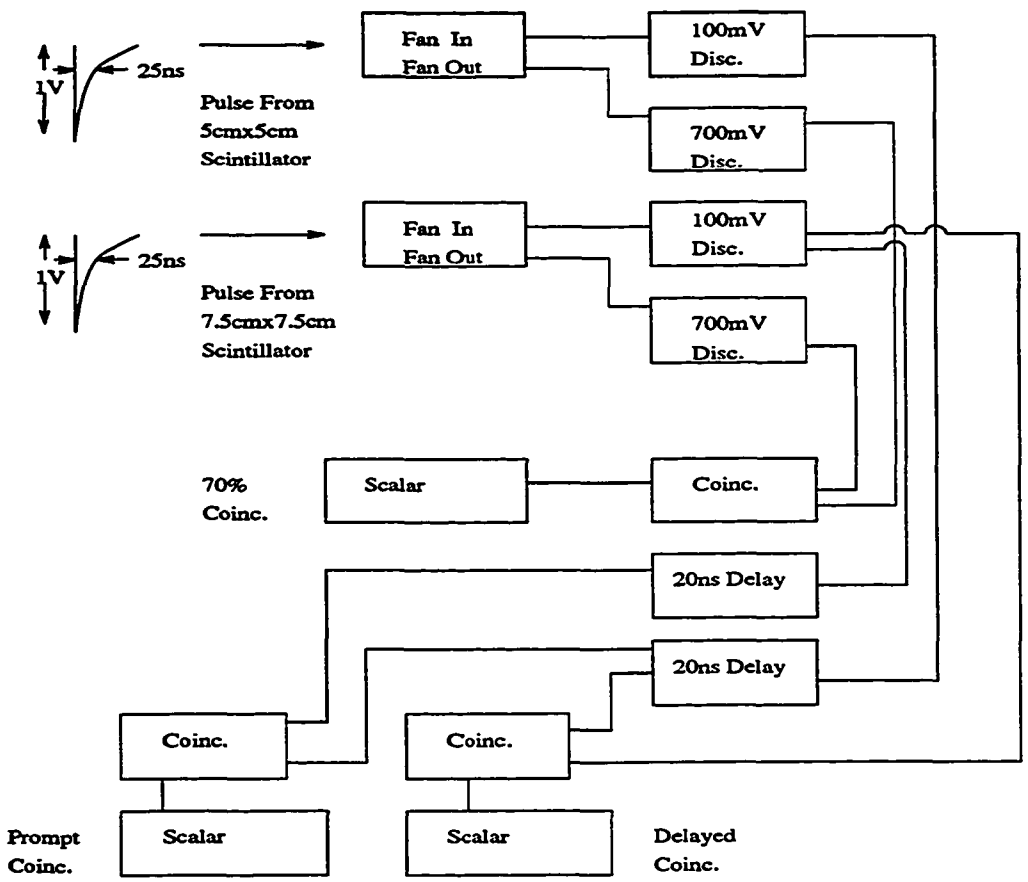

FIG. 4.5. Telescope circuit diagram.

ment and hence be counted. However, it is possible that the projectile nucleus can undergo a *nuclear* interaction with the nuclei in the scintillator. If this happens in the upstream element of the telescope, the resulting fragments that reach the downstream element may not register. This is the classic scenario of the act of measuring affecting the measurement itself. It is possible to get an estimate of the amount of interaction by assuming that the organic plastic scintillator is composed of CH with a ratio of number of H atoms to number of C atoms, H/C, of 1.1 and a density[20] of 1.0 gm/cm^2. We further assume that the C and H nuclei are homogeneously distributed throughout the scintillator so that we can treat each independently. For the radii of the three nuclei we have

$$r_H = 1.2fm(1)^{1/3} = 1.2fm$$

$$r_C = 1.2fm(12)^{1/3} = 2.75fm$$

$$r_{Au} = 1.2fm(197)^{1/3} = 6.98fm$$

so we have for the two geometric cross sections

$$\begin{aligned} \sigma_{geo}(Au, C) &= \pi(6.98fm + 2.75fm)^2 \\ &= 2.98 \times 10^{-28} m^2 \\ &= 2.98 \ \ barns \end{aligned}$$

and

$$\begin{aligned} \sigma_{geo}(Au, H) &= \pi(6.98fm + 1.2fm)^2 \\ &= 2.10 \times 10^{-28} m^2 \\ &= 2.10 \ \ barns. \end{aligned}$$

[20] W.R. Leo, *Techniques for Nuclear and Particle Physics Experiments*, Springer-Verlag, Berlin 1987.

The ratio of nuclei interacting to incident nuclei, n/n_i, is equal to the product of the cross section with the areal nuclei number density of the target (scintillator)

$$n/n_i = \sigma_{geo}\, \rho_A.$$

For a 1.6 mm thick scintillator we have for the areal nuclei number densities

$$\begin{aligned} \rho_A(C) &= \frac{(6.02x10^{23} nuclei/mole * 1.0gm/cm^3 * 0.16cm)}{13.1gm/mole} \times 1C atom/molecule \\ &= 7.35 \times 10^{21} nuclei/cm^2 \end{aligned}$$

and

$$\begin{aligned} \rho_A(H) &= \frac{(6.02x10^{23} nuclei/mole * 1.0gm/cm^3 * 0.16cm)}{13.1gm/mole} \times 1.1H atom/molecule \\ &= 8.09 \times 10^{21} nuclei/cm^2. \end{aligned}$$

So we have for the ratios

$$\begin{aligned} n/n_i(Au\ on\ C) &= \sigma_{geo}\, \rho_A(C) \\ &= 2.98 \times 10^{-24} cm^2 * 7.35 \times 10^{21} nuclei/cm^2 \\ &= 2.19 \times 10^{-2} \end{aligned}$$

and

$$\begin{aligned} n/n_i(Au\ on\ H) &= \sigma_{geo}\, \rho_A(H) \\ &= 2.10 \times 10^{-24} cm^2 * 8.09 \times 10^{21} nuclei/cm^2 \\ &= 1.70 \times 10^{-2} \end{aligned}$$

or a 3.89% (2.19% for C + 1.70% for the H) interaction of the Au nuclei in a 1.6 mm (1/16") thick scintillator. So we see that the downstream telescope element "counts"

a beam in which approximately 3.9% of the beam has had a *nuclear* interaction with the upstream element. In order to reduce this amount of interaction, the telescope elements in the second low intensity irradiation were reduced in thickness to give an interaction of approximately 2.0%. To see how these interactions affects the actual number of nuclei counted requires an examination of the discriminator levels.

Consider a projectile nucleus that passes through the Au targets and is then incident on the telescope. As indicated above, the high voltage applied to the PMT was adjusted to give a one volt pulse for a Au nucleus. Therefore a one volt pulse will be produced when this nucleus passes through the first telescope element. However, as we calculated above, suppose that this nucleus is one of the approximately 3.9 (or 2.0) percent of the projectile nuclei that undergo a nuclear interaction in the first element of the telescope. Since the amount of light produced in a scintillation is proportional to the amount of charge on the projectile, the fragments that reach the second telescope element will produce a smaller pulse than the 1v pulse that a Au nucleus would have produced in the first telescope element. If the discriminator level is set above this reduced voltage, this nucleus will not be counted.

Another scenario which can lead to discrepancies is if the beam contains some nuclei other than Au. These would pass through the Au target but then, depending on their charge, they may or may not get counted in the telescope. It was suggested that a way to reduce the uncertainty associated with this problem would be to set the discriminator levels to very low values (100mV or 10% of the 1.0 V from the PMT) thereby counting "anything" that made it through to the telescope. This would solve the problem of undercounting the number of projectiles, however this situation could lead to the problem of overcounting of Au nuclei incident on the

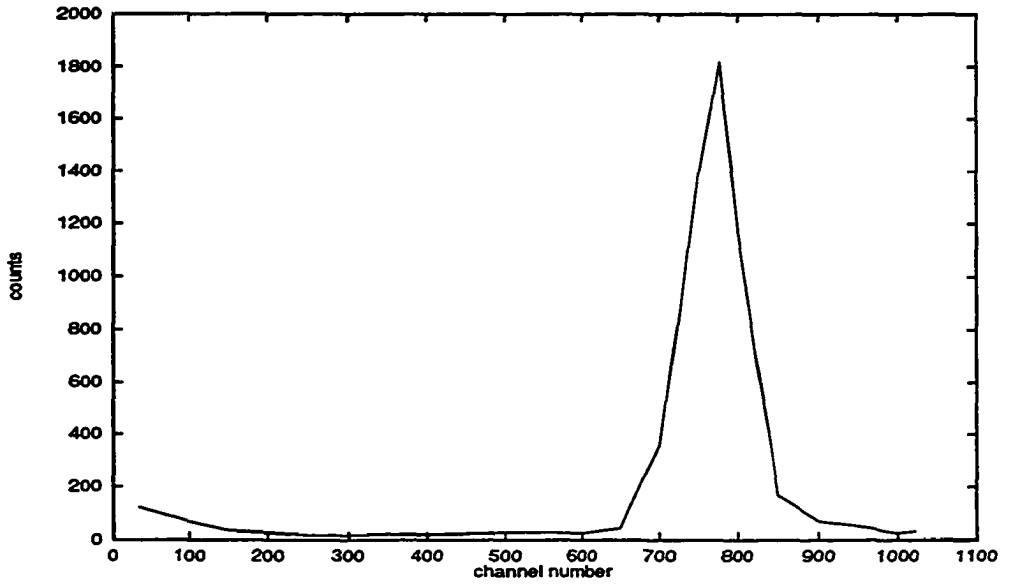

FIG. 4.6. Pulse height spectra for 5cmx5cm Scint. via qVT 3001.

targets. In an attempt to resolve this dilemma a pulse height spectra was obtained using a LeCroy qVT 3001 NIM module (see Figs. 4.6,4.7). As can be seen in the pulse height spectra, the majority of pulses are clustered around the nominal Au peak with some counts below. After taking this information into consideration and after further discussion, it was decided that the discriminator levels would be set at 100 mV or 10% of the nominal Au pulse height. However, as can be seen in Fig. 4.5, the integrated counts at 70% of the nominal Au pulse height were also recorded for comparison. The two numbers for the low intensity irradiation were 2.14×10^8 and 2.00×10^8 for the 100mV and 700mV discriminator levels respectively. This difference will be further discussed in the Error Analysis section of the Results chapter.

Not shown in the telescope circuit diagram (Fig. 4.5) was the fact that in addition to recording the coincidences between the two telescopes elements, the

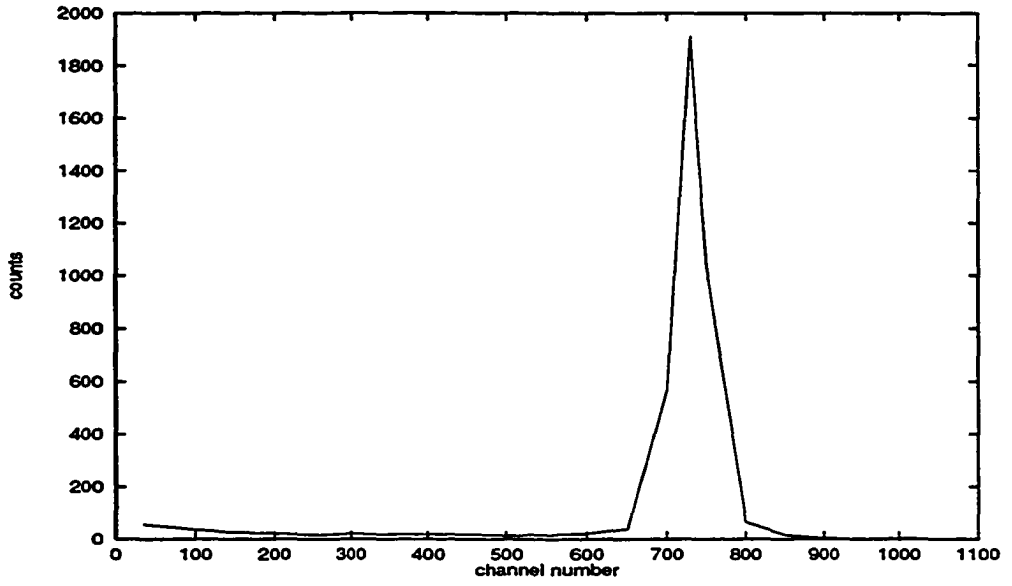

FIG. 4.7. Pulse height spectra for 7.5cmx7.5cm Scint. via qVT 3001.

singles were also recorded. By comparing the singles with the prompt and delayed coincidences, an amount of confidence can be gained in the number of projectiles recorded. As can be seen in Table 4.1, the difference between the prompt coincidences and the upstream element was less than 0.5% while the corresponding difference for the downstream element was slightly more than 1.0%.

In the low intensity runs, a telescope was used to measure as accurately as possible the number of projectiles on the target. As can be seen in Fig. 4.1, there was no telescope in the high intensity irradiations. The reason that a telescope was not used was that the spill intensity was so high ($1x10^6$) that beam pileup would make for an unacceptably high uncertainty in projectile count. In view of this fact, a beam intensity monitor (BIM) was used in the high intensity Co run. This consisted

TABLE 4.1. Projectile count for low intensity 1993 run.

Quantity	Count	% Diff. From Prompt Coinc.
Upstream(5.0cmx5.0cm)	2.141×10^8	0.19
Downstream(7.5cmx7.5cm)	2.161×10^8	1.12
Prompt Coinc.	2.137×10^8	-
70% Coinc.	2.004×10^8	6.22
Delayed Coinc.	2.449×10^5	-

of a 36 mg/cm^2 Au target inserted between the first and third Co targets (see Fig. 4.1). After the irradiation this target was counted to determine the amount of ^{196}Au produced. Since the low intensity experiment already determined the cross section for producing ^{196}Au, the beam intensity can then be inferred. A similar procedure was used for the Au high intensity experiments.

As important as knowing the intensity of the beam was knowing the location and size of the beam. The primary means of determining this information was through the use of beam location monitors (BLM). As can be seen in Fig. 4.2, the BLMs in the low intensity runs consisted of a Au target placed concentric with the experimental Au targets and downstream of the telescope. After irradiation, these Au targets were cut into concentric circles and then monitored for activity using NaI well counters (see Fig. 4.8). By monitoring the activity of the individual sections, it is possible to determine the approximate beam size as well as location. As referred to above, after the 1992 run it was decided to conduct another low intensity run. A reason for this can be seen by contrasting Fig. 4.9 with Fig. 4.10. By comparing the count rate of the BLMs for the different runs, it can be determined that the beam was significantly better centered in the 1993 run.

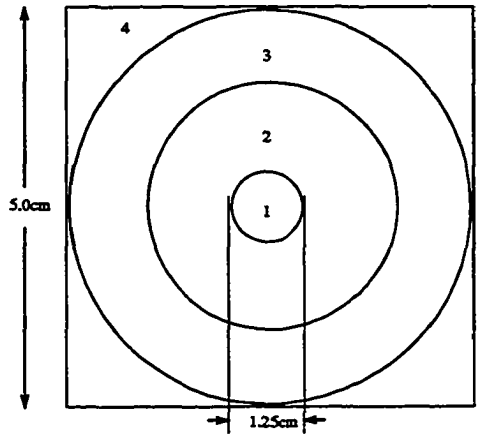

FIG 4.8. Au or Al beam location monitor.

Target Counting

While the analysis of the BLM was carried out at BNL, the main data acquisition was carried out at Iowa State University (see Fig. 4.11). After irradiation, the targets were flown back to ISU to monitor the activity created by the interaction with the RHI Au beam. As can be seen in Fig 4.11, the targets were mounted in front of a solid state gamma-ray detector. In the May 1992 irradiation, there were several Co and Au targets to monitor. To accommodate all of the targets, three detectors were utilized. A relatively old germanium lithium-drifted (GeLi) detector was used to monitor mainly the high intensity Au targets. This was called detector A. Newer high resolution high purity germanium (HPGe) detectors were mainly used to monitor the low intensity Au and high intensity Co targets. These were called detectors B and D respectively. As can be seen in Fig. 4.11, a gamma ray incident on the detector is converted into a voltage pulse. Depending on the energy of this gamma ray and the location of the active detector volume which it impacts, several

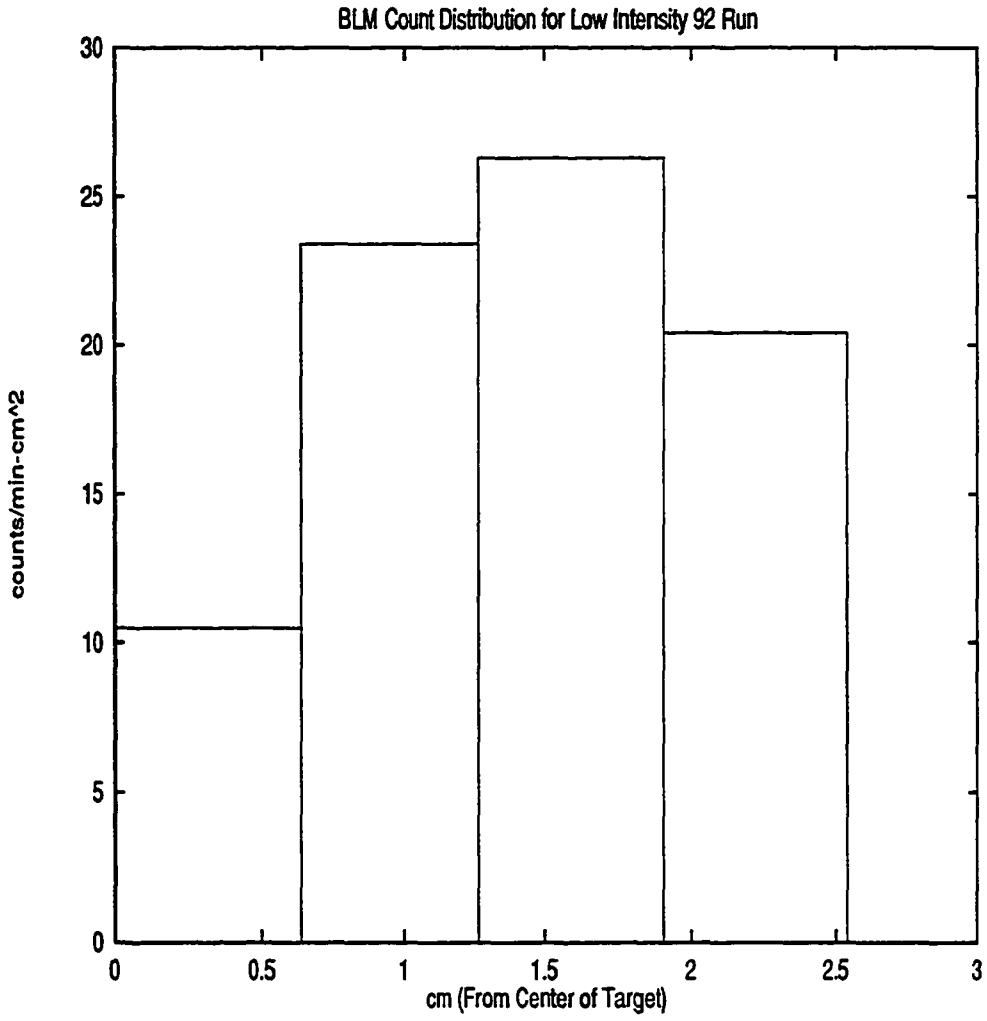

FIG. 4.9. Beam profile for first low intensity run.

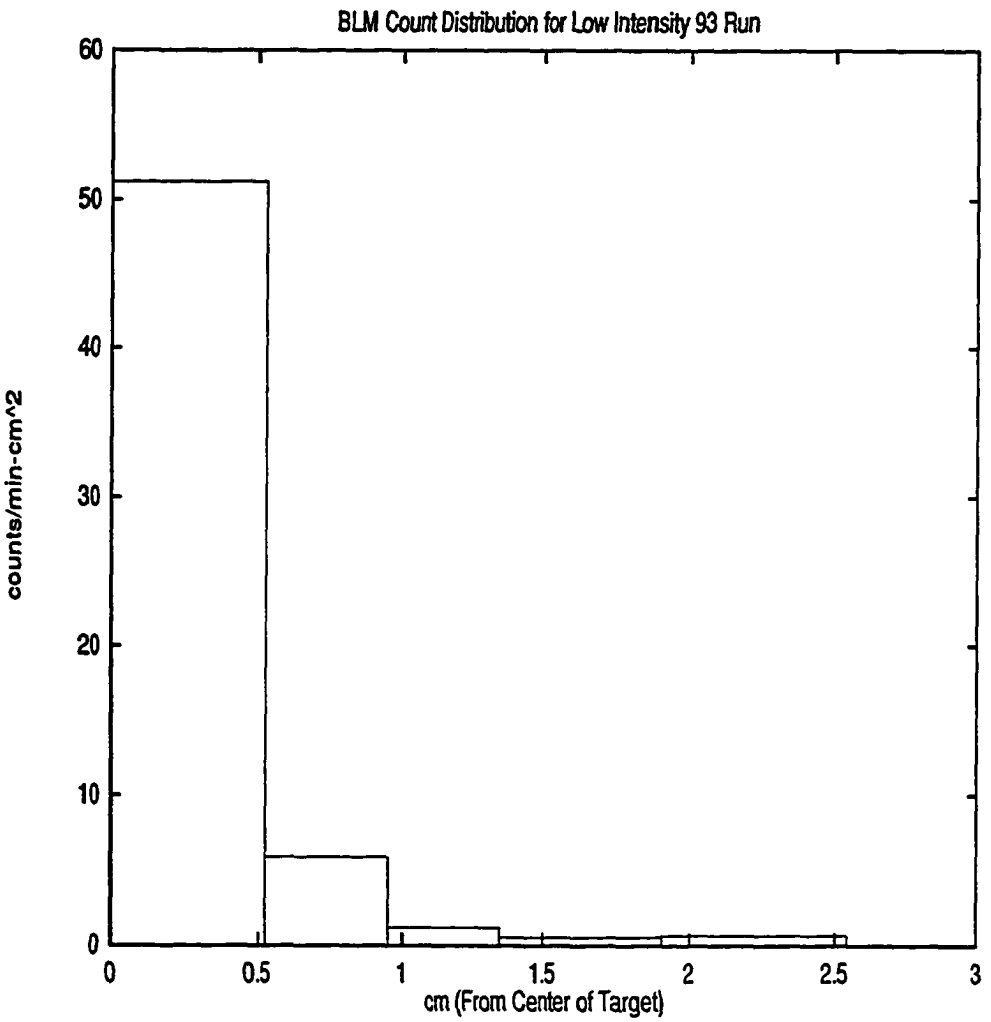

FIG. 4.10. Beam profile for second low intensity run.

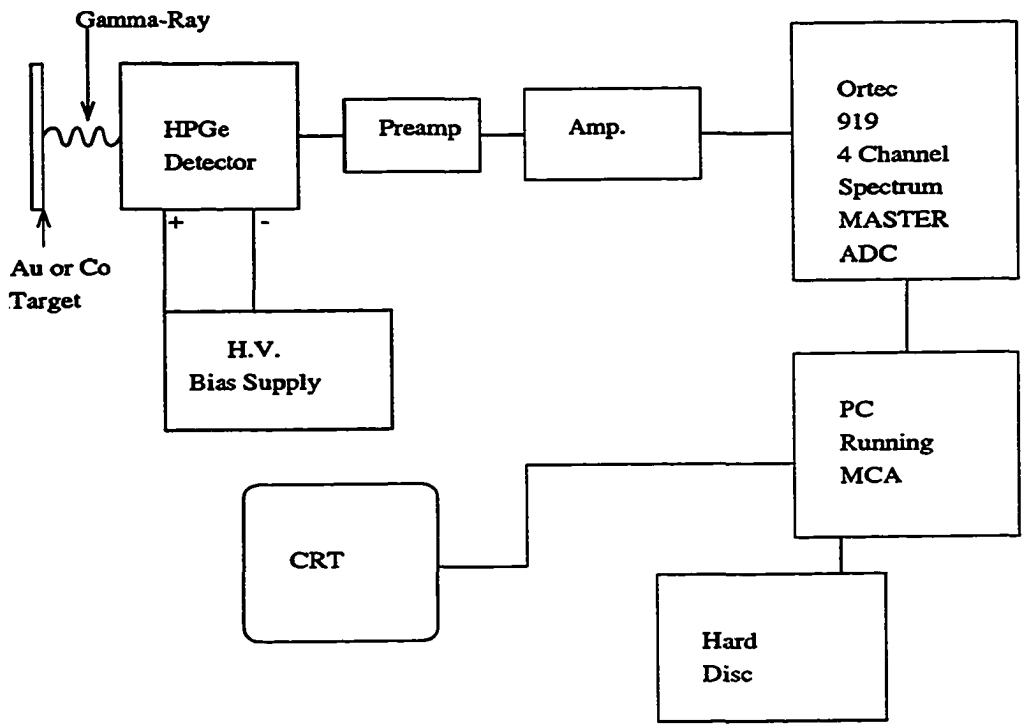

FIG 4.11. Data acquisition diagram.

different things can then happen. If the entire energy of the gamma-ray is absorbed in the detector the resultant voltage pulse contributes to the full energy peak shown in Fig. 4.12 (happens approximately 10 % of the time for a 300-keV gamma ray radiated from a source in contact with the detector face). It is also possible that instead of liberating a photo-electron/hole pair in the active region of the detector, the gamma ray Compton scatters off of an electron and then leaves the detector. In this case, the resultant voltage pulse contributes to the Compton continuum. If the gamma ray has an energy that is greater than 1022 keV, then an electron-positron pair can be created in the detector. If this happens the positron can annihilate with an electron to create two photons of energy $m_e c^2$=511 keV each. If one of the photons leaves the detector the corresponding voltage pulse would contribute to the "single escape peak" superimposed on the Compton continuum with energy 511 keV less than the full energy peak. If both of the photons escape the detector, the same thing would happen at an energy 1022 keV less than the full energy peak, the "double escape peak". Since the gamma-rays of interest were mostly less than 1022 keV, this was not usually considered. The resolution of the detectors was approximately 2 keV FWHM at the energies of interest (few hundreds of keV) for the HPGe detectors and somewhat less (approximately 5 keV) for the GeLi detector.

The HPGe detectors used to count the targets were approximately 3cm diameter x 3cm length and of cylindrical shape. Since the beam was found to be approximately 1cm^2 in size, the efficiency of the detector as a function of the distance from the center of the detector needed to be determined. This was accomplished by the work of an undergraduate physics student, Will Turner. He measured the efficiency of the detector with a small (approx. 1mm in diameter) collimated calibration

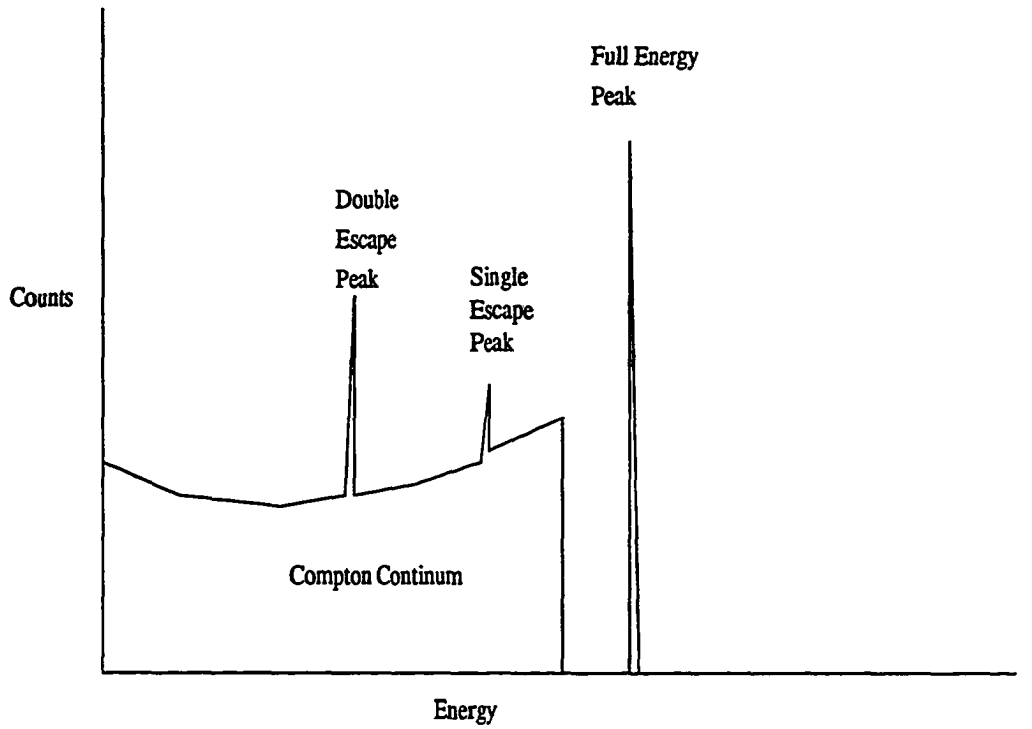

FIG 4.12 Detector response for monenergetic gamma source.

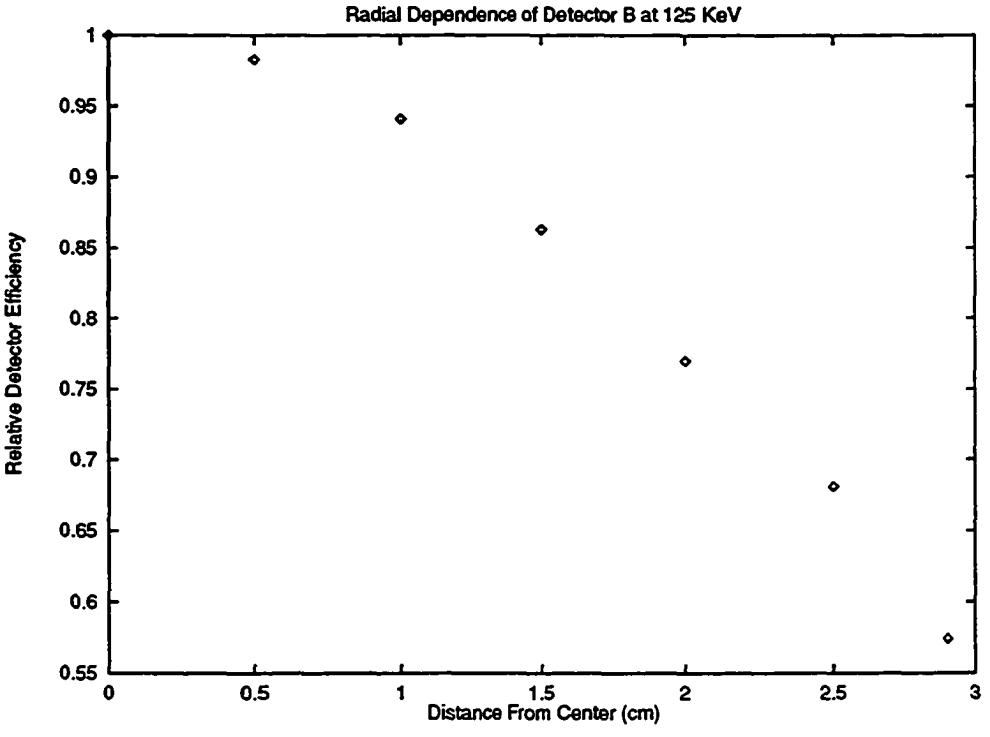

FIG 4.13 Radial detector efficiency.

source. In this way the radial efficiency of the HPGe detectors was determined. The results of this measurement can be seen in Fig. 4.13.

CHAPTER 5. DATA ANALYSIS

Computer Programs

As described in the Experiment chapter, gamma-ray spectroscopy was performed on the irradiated targets in order to determine the yield of various isotopes. In order to determine the number of counts under a particular gamma-ray peak, the peaks were fit using the MASTER software package developed at Iowa State University. This program assumes that the gamma-ray peak to be fit has a Gaussian shape with a low energy tail. This low energy tail is thought to arise from incomplete charge collection in the detector. The low energy tail is modeled in the program by joining a decaying exponential smoothly to the Gaussian main peak. The functional form of the curve used for peak fitting can be seen in Fig. 5.1. τ represents the distance from the centroid x_0 to the point where the Gaussian is joined to the decaying exponential. t is the ratio of the tail height to the peak height h. With these parameters, the curve is fit in the three regions according to the function:

Region I $(x < x_o - \tau)$:

$$f = h(1 - t + a(-z - v)^N)e^{(v(v+2z))} + ht$$

Region II $(x_o - \tau < x < x_o)$:

$$f = h(1 - t)e^{(-z^2)} + ht$$

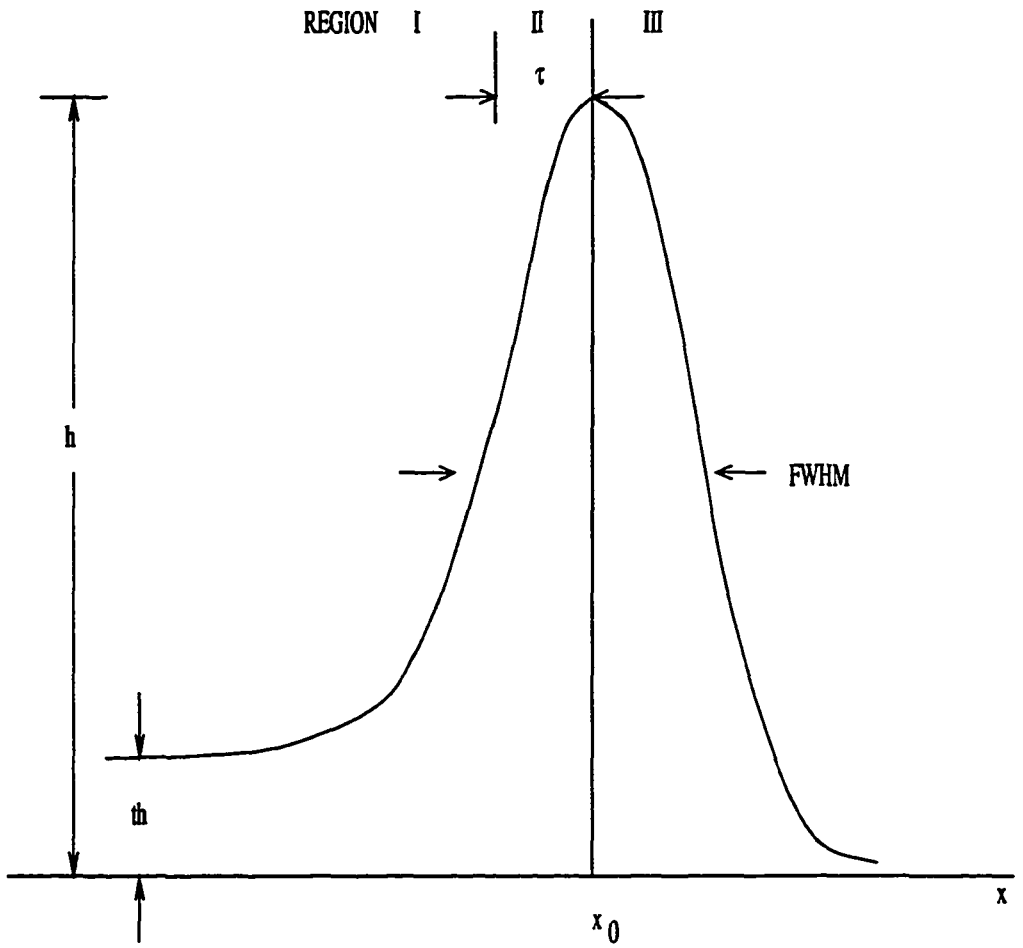

FIG. 5.1. Function used for curve fitting.

Region III $(x_0 < x)$:

$$f = h(1 + bz^M)e^{(-z^2)}$$

where

$$z = (x - x_0)/(\sqrt{2}\sigma)$$

$$v = \tau/(\sqrt{2}\sigma)$$

$$\sigma = (FWHM)/\sqrt{8ln2}.$$

The parameters a and b are related to the upper and lower skewness of the peaks. These were rarely used when fitting the peaks. M and N are fixed integers. If a set of data points y_i that represent counts/channel are desired to be fit, the computer program MASTER calculates the values of the parameters which give the minimum value of the quantity

$$Q = \sum_i w_i(y_i - f(x_i))^2$$

where w_i are the weights of the data points which represents the uncertainty in the measurement of y_i. x_i are the channel numbers. A more detailed description of how this program fits curves can be found in the error analysis section of the Results chapter.

As referred to above, the program MASTER is used to fit the peaks of the gamma-ray spectra obtained from the irradiated targets. This data was taken over a period of 0-6 months after the targets are brought back to Iowa State University. To determine the amount of a particular isotope that was created in the target, the area of a gamma-ray peak associated with that isotope is plotted as a function of time using the computer program MASH. A sample of this plot can be viewed in Fig. 5.2. Since the half-life of ^{196}Au is well known (6.18 days[21]), it is possible to extrapolate

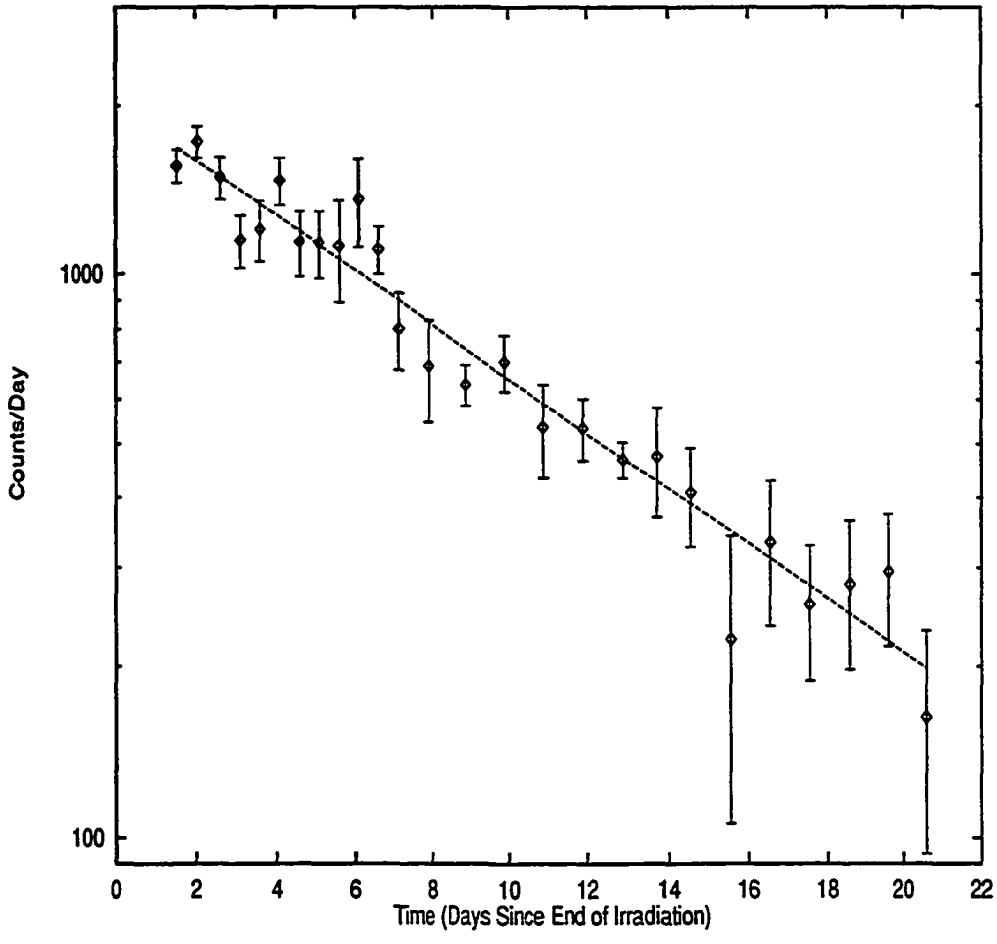

FIG 5.2. Decay of ^{196}Au from MASH output.

the straight line shown in the plot to zero time to determine the saturated activity. Knowing this, among other things, allows the cross section for creating ^{196}Au from ^{197}Au to be determined, as will be discussed in the next chapter.

Gamma-Ray Spectra

A sample background spectrum can be seen in Fig. 5.3. This spectrum represents a 14 day background on detector B. The most prominent peak in this spectrum occurs approximately at channel 1025 and is a gamma-ray from ^{214}Bi, E_γ=609.3 keV, in the decay chain of ^{238}U. In attempting to fit the curves of desired isotopes, it is important to realize that the target spectrum is *superimposed* on top of this background. In Fig. 5.4 we see a one day spectrum from the 36 mg/cm^2 Au target from the 1992 high intensity irradiation 27 days after the end of the irradiation. In comparing the two spectra, one can see many additional peaks in the Au spectrum compared with the background. By fitting these additional peaks and searching nuclear databases, it is possible to determine what isotopes were created in the RHI collisions taking place in the target. As referred to in the experiment chapter, the yield of ^{196}*Au* was crucial to determining many different cross sections. The primary method by which the yield of this important isotope was determined was to fit a gamma-ray peak of energy 355.6 keV given off in the beta-decay (electron-capture) of this unstable Au isotope. It is therefore very important to know the background spectrum in the vicinity of 355.6 keV. In Fig. 5.5 we see an exploded view of this

[21] E. Browne and R.B. Firestone, *Table of Radioactive Isotopes*, John Wiley & Sons, Inc., New York 1986.

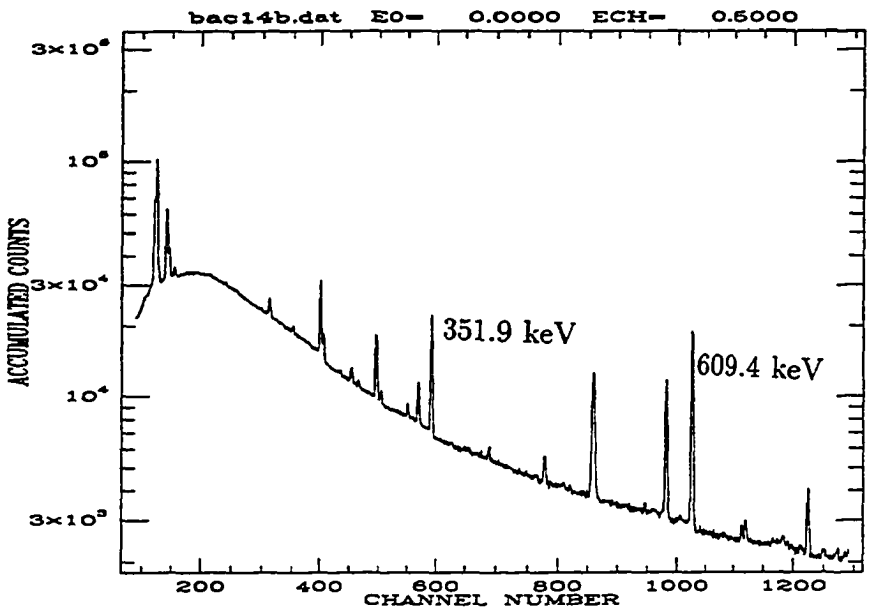

FIG 5.3. 14 day background spectrum on detector B.

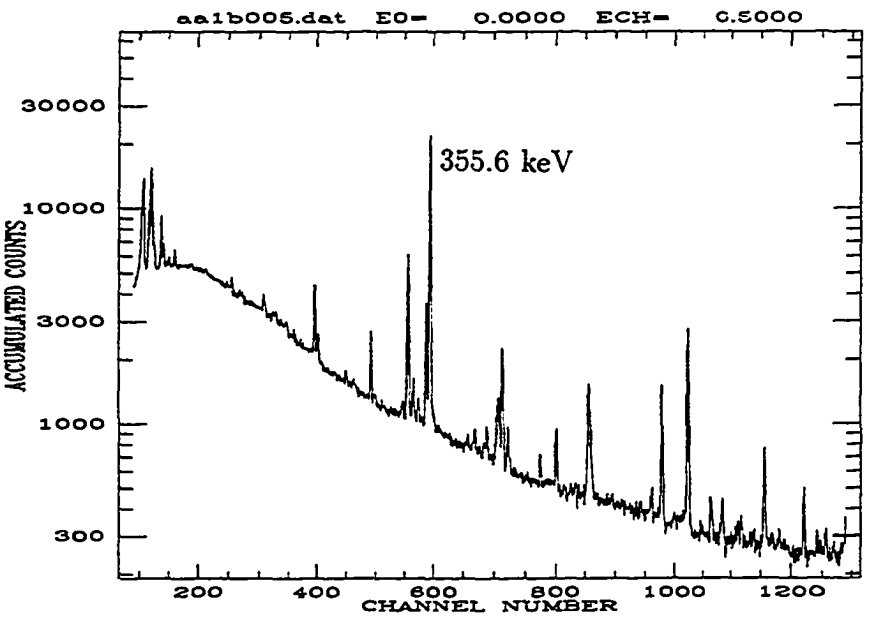

FIG. 5.4. One day spectrum of high intensity Au target on detector B.

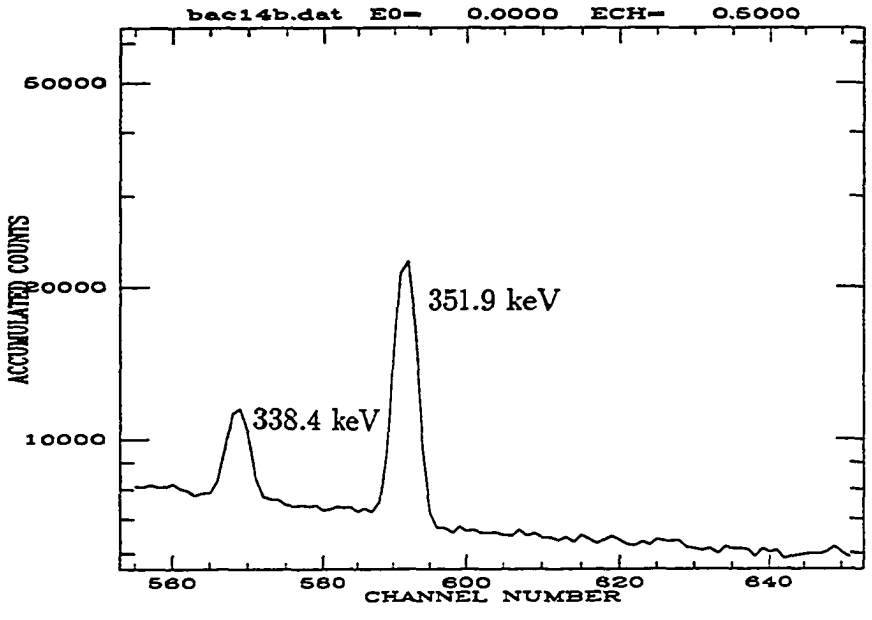

FIG 5.5. Expanded view of vicinity of 355.7 keV on detector B.

area. At channel number 590.6 we see the most prominent background peak which was found to be due to ^{214}Pb, Eγ=351.9 keV, again in the decay chain of ^{238}U. Upon further investigation, this peak was found out to actually be a doublet which included a peak at channel number 589.08 due to ^{211}Bi, Eγ=351.0 keV, in the decay chain of ^{235}U. Since this peak is overwhelmed by the much larger 351.9 keV peak, we must use our knowledge of decay chains and equilibrium to determine the ratio of the peak areas. We know that the ratio of the abundance of ^{235}U to ^{238}U is

$$\frac{N_{235_U}}{N_{238_U}} = \frac{0.7}{99.3} = 7.05x10^{-3}$$

also we have the equilibrium condition for elements in a decay chain

$$N_{211}R_{211} = N_{235}R_{235}$$

and

$$N_{214}R_{214} = N_{238}R_{238}$$

where N_{number} is the number of atoms of a particular isotope and R_{number} is the decay rate of a particular isotope. We thus find that

$$\begin{aligned}\frac{N_{211}R_{211}}{N_{214}R_{214}} &= (7.05x10^{-3})\frac{R_{235}}{R_{238}} \\ &= 4.51x10^{-2}.\end{aligned}$$

For an individual peak we know that the area is proportional to $N \cdot R \cdot BR$ where BR is the branching ratio for the peak in question. We have $BR_{211} = 0.128$ and $BR_{214} = 0.371$ so that if we assume that the detector efficiency is equal at the two energies we have for the ratio of peak areas

$$\begin{aligned}\frac{P.A._{211}}{P.A._{214}} &= 4.51x10^{-2}\frac{0.128}{0.371} \\ &= 0.016.\end{aligned}$$

The program MASTER had the capability to fix the height and position of one peak in relation to another and this was done in fitting this doublet.

Another peak which required close scrutiny was the 98.9 keV peak associated with the two neutron removal product, ^{195}Au. Due to the smaller branching ratio (0.109) and the smaller cross section, a small error would make a relatively large contribution to the estimation of this peak area. In Fig. 5.6 we see a four day spectrum of the high intensity Au target taken 55 days after the end of the irradiation. At a channel of approximately 155 we see the 98.9 keV ^{195}Au peak. To the

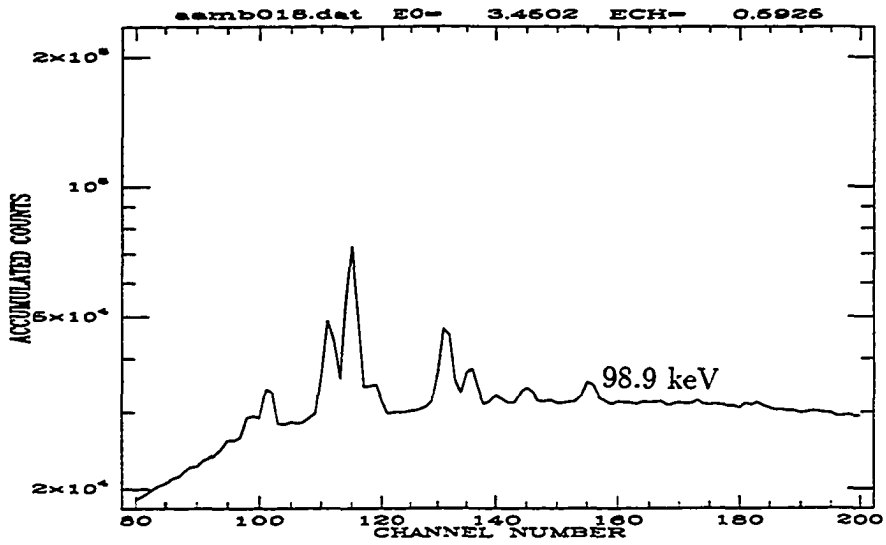

FIG. 5.6. Expanded view of four day spectrum around 98 keV.

left at channel 145 we see a ^{234}Th background peak from the decay chain of ^{238}U followed by a Pb K_β doublet centered at channel 133 and a Pb K_α doublet centered at channel 113 (due to the Pb shielding of the detector). Of concern in calculating a cross section based on this peak was contamination from isotopes other than ^{195}Au. To investigate this possibility, a search of "Nuclear Data Tables" was conducted for isotopes with energy close (within 0.5 keV) to 98.9 keV. A summary of this data can be seen in Table 5.1. % Abun. indicates the relative abundance of the gamma ray near 98.9 keV and Most Abd., E gives the relative abundance and energy of the most intense gamma ray from the corresponding isotope.

Most of these isotopes were found not to contribute to the 98.9 keV ^{195}Au peak. Some, like ^{158}Tb, had a half-life too long to allow for any substantial contribution. For others, like ^{148}Pm, a search was made for the most abundant gamma

TABLE 5.1. Isotopes with gamma rays around 98.9 keV.

Element	$T_{1/2}$	E (keV)	% Abd.	Most Abd., E (keV)
^{188}Pt	10.2 d	98.4	0.34	35.9, 155.0
^{148}Pm	41.3 d	98.5	2.48	95.6, 550.3
^{158}Tb	150.0 y	98.9	4.65	43.1, 944.2
^{195}Pt	4.02 d	98.9	11.4	2.83, 129.7
^{183}Re	70.0 d	99.1	2.70	23.5, 162.3
^{183}Ta	5.1 d	99.1	6.60	26.7, 246.1
^{168}Tm	93.1 d	99.2	4.36	50.0, 198.2
^{186}Re	$2.0\text{x}10^5$ y	99.3	1.11	18.6, 59.0

ray. An upper limit was placed on the area of this gamma-ray and by accounting for the different branching ratios and detector efficiencies for the two gamma-rays, an upper limit was placed on the contribution to the 98.9 keV gamma-ray. If this limit was less than 1.0% of the total counts of the 98.9 keV peak, it was ignored. There were two isotopes which survived these cuts. One was ^{183}Re. By fitting a peak at 162.3 keV, and accounting for different branching ratios and detector efficiencies, approximately 100 counts/day were subtracted from each of the input data points for the MASH computer run for ^{195}Au due to ^{183}Re. The difference between these, no subtraction and subtraction due to ^{183}Re, can be seen in Figs. 5.7 and 5.8 respectively. The corresponding saturated activities were 639,170 and 630,701 counts/day respectively (see Table 6.2 in results section).

The other isotope which survived was ^{168}Tm. A background peak near 198.2 keV made it difficult to determine whether there was a peak there due to ^{168}Tm. An upper limit of 1.1% was determined to be the contribution to the 98.9 keV peak and consequently a 1.1% uncertainty was added in quadrature to the total

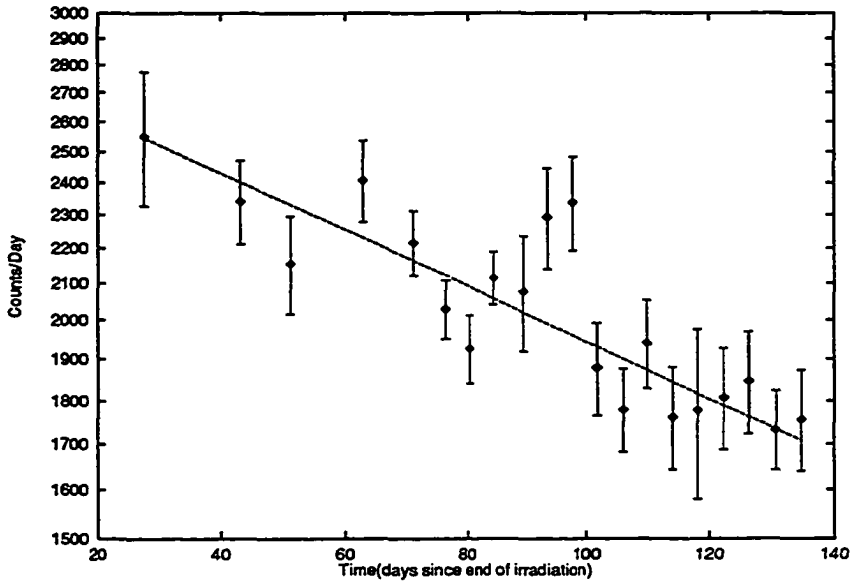

FIG. 5.7. Decay of ^{195}Au before subtraction due to contribution of ^{183}Re.

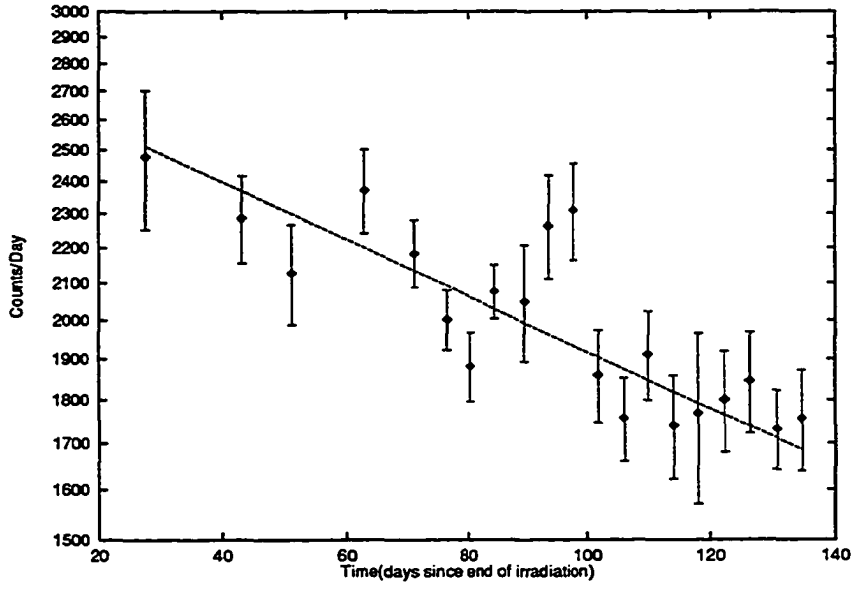

FIG. 5.8. Decay of ^{195}Au after subtraction due to contribution of ^{183}Re.

uncertainty for the calculated value of $\sigma(^{195}\mathrm{Au})$. While other difficulties arose in various stages of the data analysis, the above examples of $^{196}\mathrm{Au}$ and $^{195}\mathrm{Au}$ give a good representation of the obstacles encountered in isotope identification.

Corrections

In the process of calculating various ED cross sections, there were many corrections needed. The first discussed is the nuclear correction. In Figs. 5.9 and 5.10 we see two different types of RHI collisions. In Fig. 5.9 the impact parameter b is greater that the sum of the radii of the projectile and target nuclei. The two nuclei interact through the electromagnetic force. In Fig. 5.10 b is less than $\mathrm{R}_P + \mathrm{R}_T$ and the two nuclei interact through both the electromagnetic and the nuclear force. In attempting to calculate an *ED* cross section, it is impossible to tell which type of collision created a particular fragment. However, if the concept of factorization is used, it is possible to estimate the fraction of a particular isotope due to nuclear collisions. Factorization assumes that the increase in the yield of a particular target fragment in going, for example, from proton to Au projectiles is due solely to the fact that the Au projectiles are larger. Equivalently, the nuclear cross section for producing a particular target fragment factorizes into a projectile dependent part and a target dependent part with no interference between the two. With this assumption, the ratio

$$\sigma[^{197}Au(^{197}Au, X)F_i]/\sigma[^{197}Au(p, X)F_i]$$

should be constant for any fragment, F_i. This ratio was measured for 11 different fragments (See Table 6.1 of results chapter). It ranged from a low of 1.28 ± 0.29

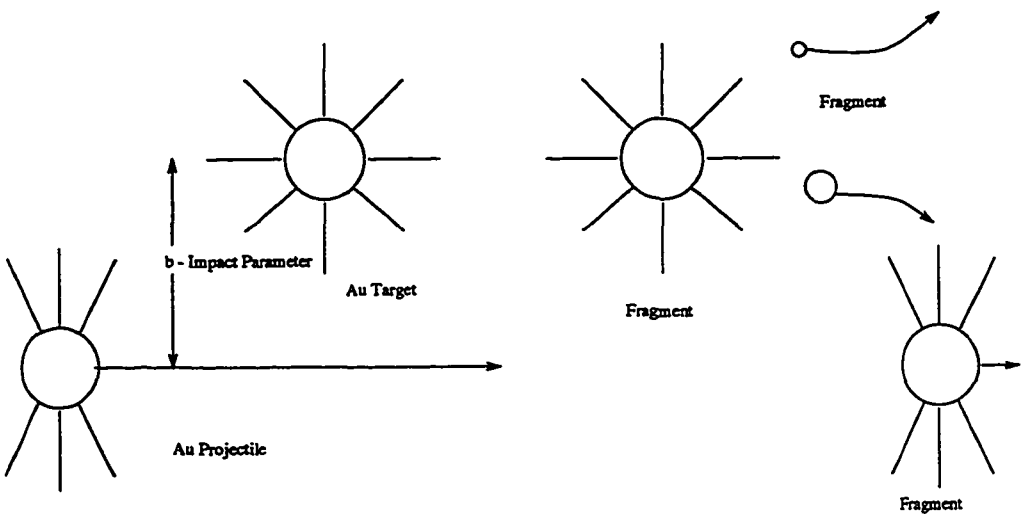

FIG. 5.9 Electromagnetic collision, b > $R_P + R_T$.

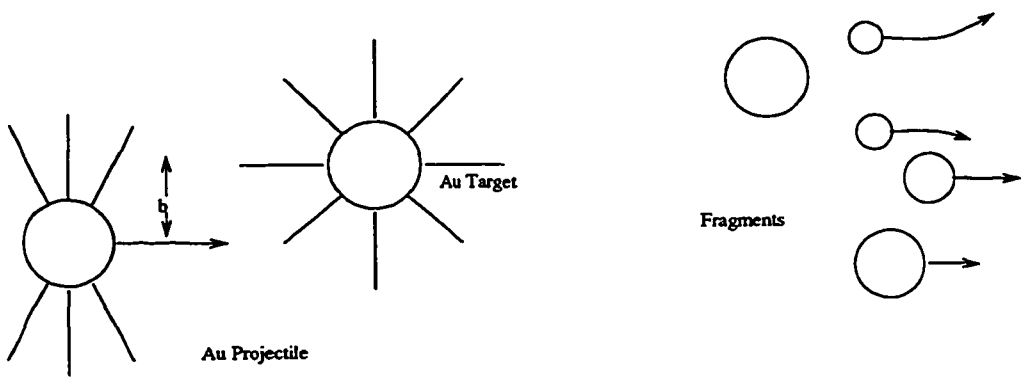

FIG. 5.10 Nuclear collision, b < $R_P + R_T$.

for ^{167}Tm to a high of 4.37 ± 0.67 for ^{188}Pt. The average was 3.58 ± 0.89(0.67 statistical, 0.58 systematic. The systematic error was due to the various uncertainties inherent in the determination of a cross section such as detector efficiency, number of projectiles, etc. This will be discussed in the Error Analysis section of the Results chapter). To then estimate the nuclear cross section

$$\sigma[^{197}Au(^{197}Au, X)^{196}Au]$$

we multiply the average ratio, 3.58, by the proton induced cross section

$$\sigma[^{197}Au(p, X)^{196}Au] = 75mb$$

to obtain the value

$$\sigma[^{197}Au(^{197}Au, X)^{196}Au] = 269 \pm 67mb.$$

In Fig. 5.11 we can see this information plotted graphically. The extreme departure from factorization by ^{196}Au is a clear demonstration of the large ED component of this fragment. The values of the various ED and nuclear cross sections will be given in the results section.

As mentioned earlier, in the high intensity runs three different target thicknesses were used in order to determine the amount of secondary reactions. Since the amount of primary interactions is proportional to the thickness of the target, and the amount of secondary reactions is proportional to the amount of primary reactions, the amount of secondary reactions is expected to be proportional to the thickness squared. By then plotting the intensity of a particular gamma-ray divided by the thickness of the target versus the target thickness and measuring the slope, it is possible to estimate the amount of interactions due to secondary reactions. Such a plot

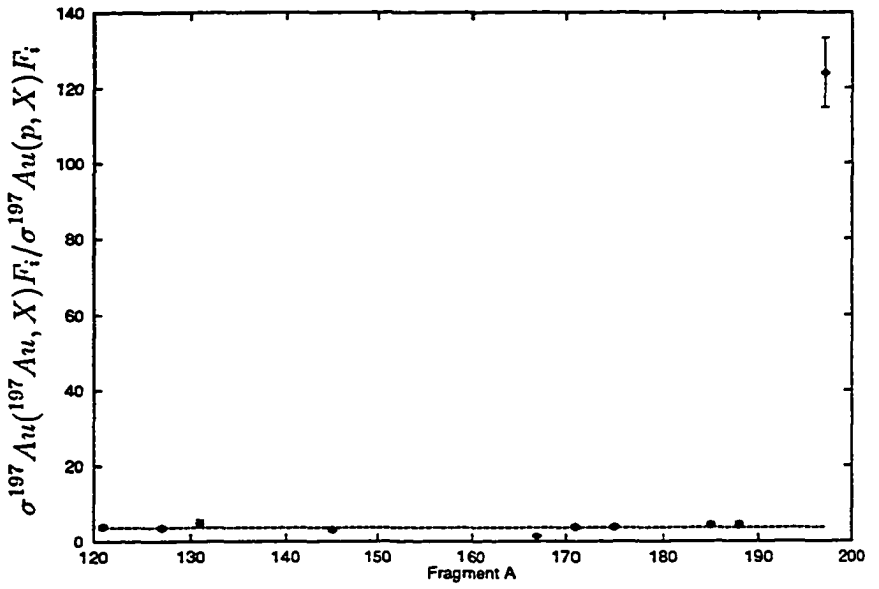

FIG. 5.11. Cross section ratio of Au to p vs. A.

for ^{58}Co (one neutron out of ^{59}Co) and for ^{196}Au (one neutron out of ^{197}Au) is depicted in Figs. 5.12 and 5.13 respectively.

In these plots the line is a weighted least squares fit to the three data points. This line can be expressed as

$$I/t = c + mt$$

where I is the intensity, t is the thickness, c is the y-intercept and m is the slope. To calculate the percentage of secondary reactions that took place in the 47.94 mg/cm^2 target, we determine the amount of deviation of I/t from c. i.e.

$$\begin{aligned} amount\ of\ secondary\ correction &= \frac{mt}{c} \\ &= \frac{(0.1609)(47.94)}{386.86} \\ &= 0.020 \end{aligned}$$

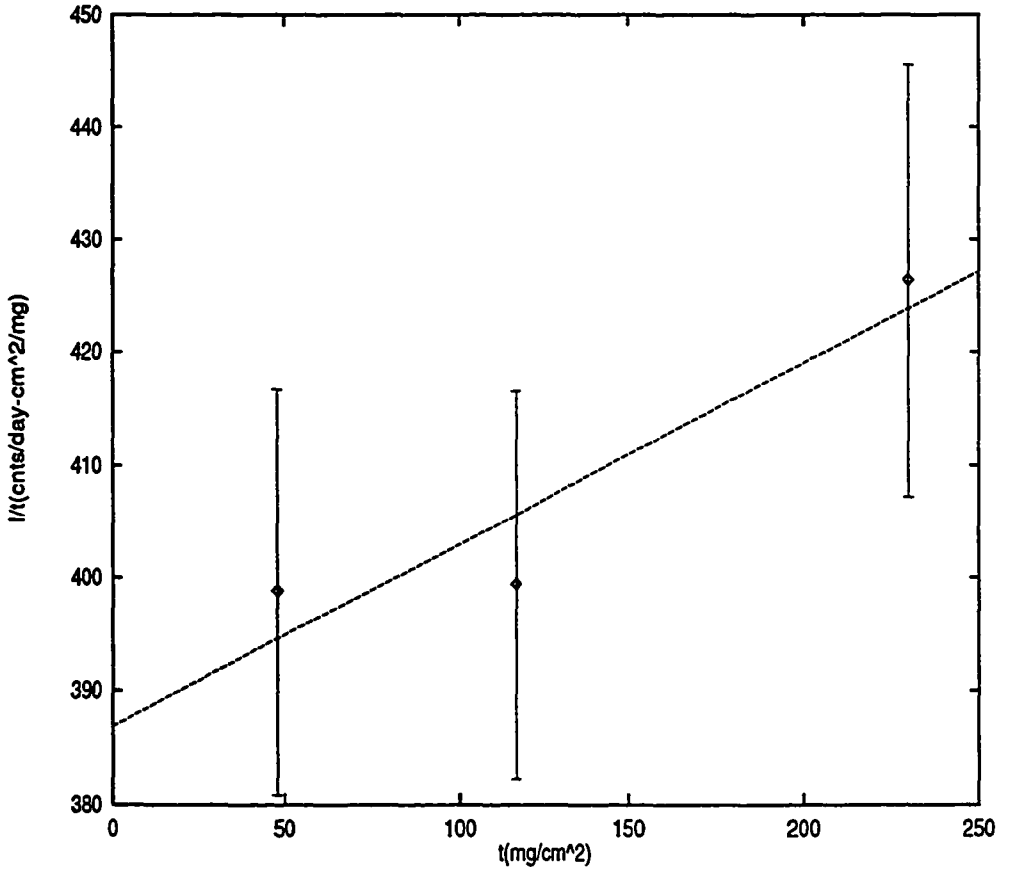

FIG. 5.12. Secondary correction plot for Co.

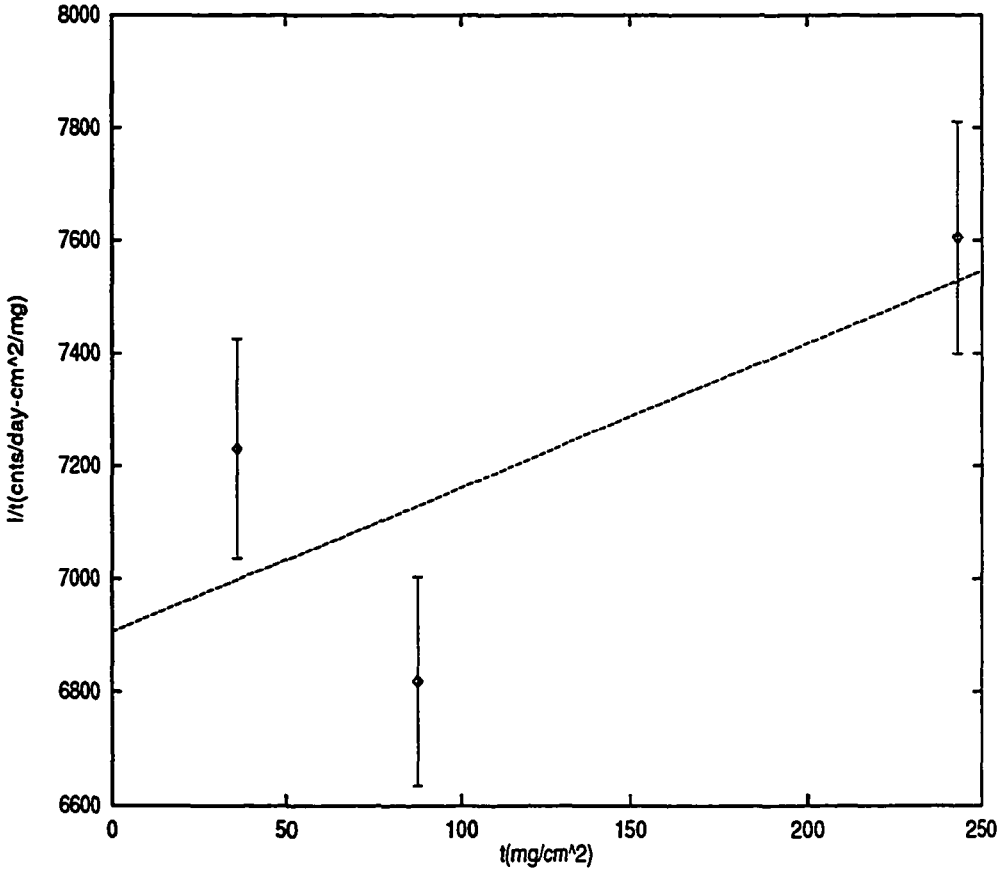

FIG. 5.13 Secondary correction plot for Au.

TABLE 5.2. Secondary corrections for neutron emission products.

Product	E (keV) of γ-Ray Used	% Sec. Reactions	Error ± %
^{58}Co	811.0	2.0	±5.8
^{57}Co	122.0	5.40	±5.3
^{56}Co	847.0	8.90	±61.2
^{196}Au	355.6	1.84	±102.4
^{195}Au	98.9	0.0	±4.2

or 2.0% of the reactions in the 47.94 mg/cm^2 are due to secondary reactions. In Table 5.2 we see the results of the secondary reactions for the Co and Au targets.

The secondary corrections for Co followed the expected trend of the one neutron out product, ^{58}Co, having the smallest secondary correction since it has the largest ED contribution. Compared to a nuclear product, an ED product is expected to have a smaller percentage secondary correction since the particle multiplicity in an ED collision is in general much smaller than for a nuclear collision. The fact that ^{195}Au has a smaller correction than ^{196}Au is difficult to explain. The large error associated with the ^{196}Au correction could mean that in fact neither the one *or* two neutron out Au products had a measurable secondary correction.

Another interaction within the target is gamma ray absorption. A target nucleus that has undergone ED can emit a gamma ray that gets absorbed before exiting the target. This gamma ray would not be counted in the Ge detector leading to an underestimation of the cross section. The absorption of gamma rays by different elements is well documented.[22] The expression for the fractional loss of gamma-ray

[22]K. Way, Nuclear Data Tables, 7, 574 (1970).

intensity is

$$\frac{I(t)}{I_0} = \frac{1}{\lambda t}(1 - e^{-\lambda t}).$$

This correction[23] ranged from a low of 0.998 for a 847 keV gamma-ray in the thin Co target to a high of 0.552 for the 98.9 keV gamma-ray in the thick Au target.

In addition to the target corrections, there were corrections concerning the detector. An important one of these corrections was the summing-out correction. This correction occurs when two gamma rays are emitted from a target and impinge on the HPGe detector and are not resolved in time. If this happens, the detector registers a single gamma ray detected with an energy equal to the sum (or a fraction thereof) of the two gamma rays and the intensity of each of the single gamma rays is under-estimated. This phenomena can be illustrated by viewing the decay diagram Fig. 5.14. As can be seen in this diagram, if the ^{196}Au nucleus undergoes beta decay via electron capture, the resultant excited Pt nucleus decays via gamma-ray emission. This gamma-ray de-excitation occurs by the *coincident* emission of the 355.6 keV and 332.9 keV gamma rays. Since these two gamma rays are emitted in coincidence, there is a relatively high probability of the summing out phenomena occurring if the solid angle for acceptance is large. That this is so can be demonstrated by considering a very efficient 4π detector. If such a detector was available, it would register *only* the sum peak of 689 keV and never the individual 332.9 keV and 355.6 keV peaks. If, on the other hand, the excited Au nucleus undergoes beta decay via

[23]Note: This is actually an upper limit for gamma ray absorption since it is possible for a photon to be scattered through a small angle and still get absorbed in the detector. The absorption coefficient from Ref. 22 has a Rayleigh scattering component of less than 4% for a 100 keV photon in Au where this process (small angle scattering) is most likely to occur.

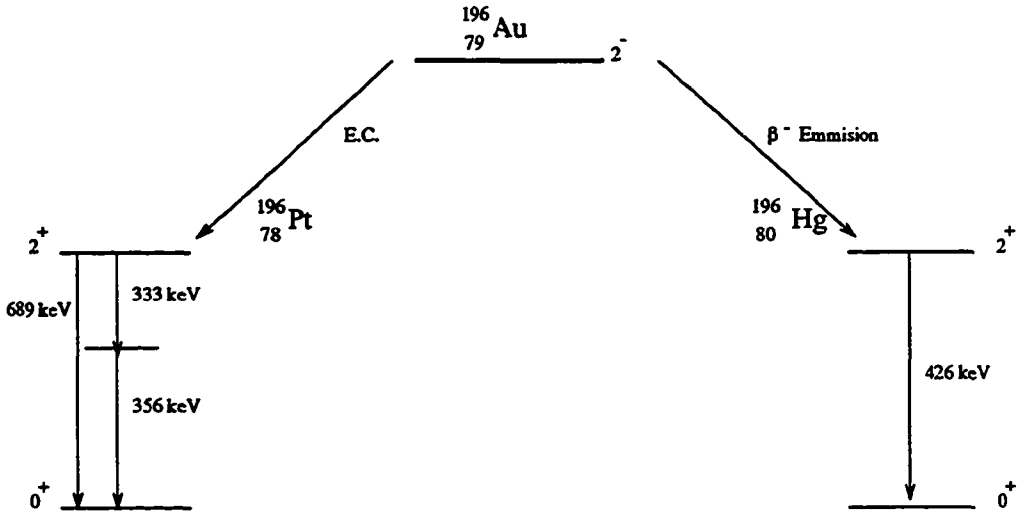

FIG. 5.14. Decay of ^{196}Au.

β^- emission, the de-excitation of the resultant Hg nucleus is by a 426.1-keV gamma ray *not* emitted in coincidence with other gamma rays. By exploiting this difference in the two gamma rays (the 355.6 and the 426.1 keV) we were able to estimate the summing correction to the 355.6-keV gamma ray.

To accomplish this, a Pt target was irradiated with a high intensity proton beam at BNL. This created large amounts [much more (>factor of 10) than the high intensity Au on Au irradiation (see Fig. 4.1 in experiment chapter)] of ^{196}Au. The large amount of ^{196}Au produced allowed this target to be counted at relatively large distances (up to 5.25 in) from the HPGe detector. At these large distances, the summing correction becomes negligible. Hence if we plot the ratio of the area of the 355.6 keV peak to the 426.1 keV peak as a function of the distance from the HPGe detector, the amount of summing can be estimated by comparing the ratio of these two peaks at distances close to and far away from the detector. Such a plot

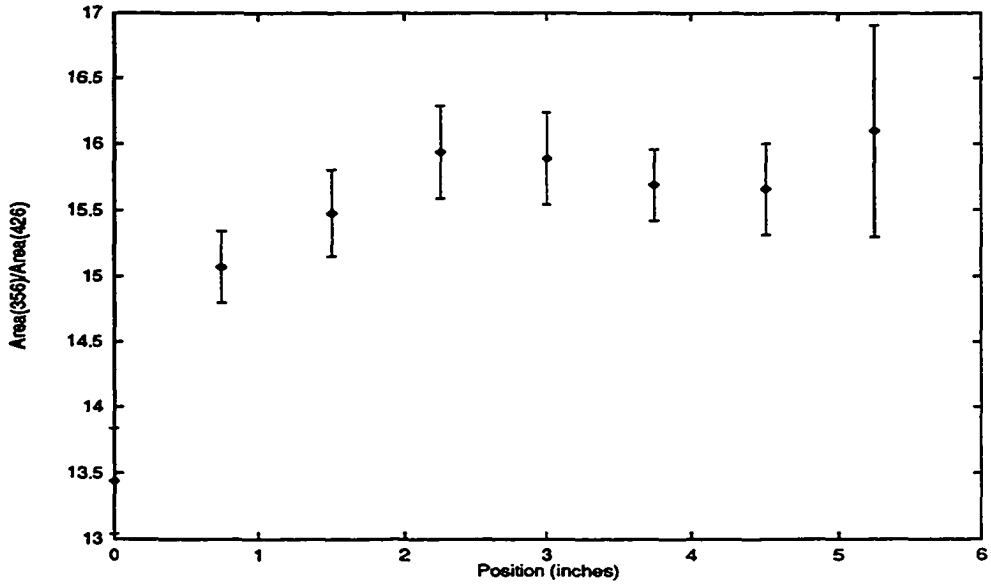

FIG. 5.15. Summing correction plot.

is depicted in Fig. 5.15. Using this plot, the summing correction for ^{196}Au was determined to be 0.835 $\pm$ 0.031 with the target positioned flush with the detector face and 0.936 $\pm$0.026 at a distance of 0.75 inches from the detector face.

The last correction to be discussed is the one due to beam spread and radial detector efficiency dependence. Ideally, the Au beam traveling in the z direction would have very little extent in the x-y plane of the target and could be aimed with infinite precision. In practice neither of these criterion are met and the deviation from them needs to be corrected. As referred to at the end of the Experiment chapter, the radial dependence of the detector efficiency was determined using a small (0.5cm diameter) NBS SRM-4275-B-73 calibration source containing ^{154}Eu and ^{125}Sb (see Fig. 4.12). From Fig. 4.12, the efficiency of the detector at radial distances equal to the radii of the rings into which the BLM was cut was determined (see Fig. 4.8).

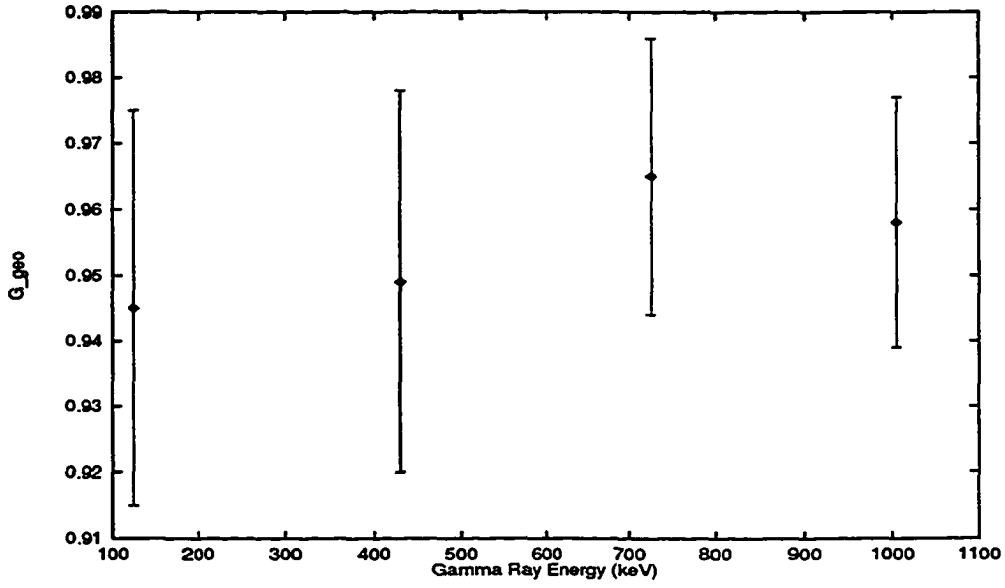

FIG. 5.16. Geometrical beam factor.

The geometrical beam factor, G_{geo} was then calculated according to the formula

$$G_{geo} = \sum_{i=1}^{4} \epsilon_i f_i$$

where ϵ_i is the relative efficiency of the detector at a given radii (see Fig. 4.12) and f_i is the fraction of the total activity in the BLM a given ring contains. This factor is most accurate when the beam is centered on the target as was the case in the second low intensity run (see Fig. 4.10). When the beam is off centered as was the case in the first low intensity run (see Fig. 4.9) there is more uncertainty due to limited knowledge of the target activity location with respect to the gamma ray detector. This additional uncertainty is why the second low intensity run was conducted. This geometrical beam factor was then plotted versus energy to give a plot such as Fig 5.16.

CHAPTER 6. RESULTS

Cross Sections

As the title of this thesis implies, the main objective of these experiments was to measure as accurately as possible the phenomena referred to as electromagnetic dissociation (ED) using a 10.2 GeV/nucleon Au beam to bombard Au and Co targets. The chosen way to characterize these collisions is to measure/calculate the cross sections for various reactions. The ED reactions that are most probable (i.e. have the largest cross sections) are one and two neutron removal from either the target or projectile. This is due to the fact that since neutrons have no net charge, they are not emission inhibited by the coulomb barrier in distinction from protons. As was discussed in the Data Analysis chapter, a significant correction was the contribution to the total cross section from nuclear (non-ED) processes. The production cross section of 11 different nuclear reaction products for Au and 4 for Co were determined by counting gamma rays from the targets from the high intensity runs. A summary of the Au and Co nuclear cross sections can be seen in Tables 6.1 and 6.2.

The ratios of these cross sections to the corresponding proton cross section[24] (last column in Table 6.1) vs. nuclear product A are plotted in Fig 5.11.

[24] S. B. Kaufman *et al.*, Phys. Rev. C. **14**, 1121 (1976).

The cross sections were calculated according to the formula

$$\sigma_{total} = \frac{(A_{sat})(1 - S.C.)(A_t)(T_{rad})}{(N_{ava})(N_{proj})(\rho)(\epsilon)(b)(C_{sum})(G_{geo})(G_\gamma)}$$

with

A_s - Saturated Activity

$S.C.$ - Secondary Correction

A_t - Atomic Weight of Target

T_{rad} - Time of Irradiation

N_{ava} - Avagadro's Number

N_{proj} - Number of Projectiles

ρ - Areal Density of Target

ϵ - Efficiency of HPGe Detectors

b - Branching Ratio of γ-ray Used

C_{sum} - Coincidence Summing Correction

G_{geo} - Geometric (Beam-Target-Detector) Factor

G_γ - γ-ray Absorption in Target.

TABLE 6.1. Parameters for Au nuclear products and cross sections.

Isotope	E (keV)	Det.	$T_{1/2}$ (d)	b ± %	S.C.± % [a]	ϵ ± %
^{121}Te	573	A	16.8	0.80 ± 2.1	3.87 ± 0.8	3.9 ± 4.0
^{127}Xe	202	B	36	0.68 ± 5.0	4.16 ± 0.9	16.0 ± 4.0
^{131}Ba	496	A	12	0.44 ± 9.1	4.36 ± 0.9	4.5 ± 4.0
^{145}Eu	894	A	5.9	0.65 ± 5.0	5.04 ± 1.1	2.4 ± 4.0
^{155}Tb	105	A	5.3	0.23 ± 17.0	5.53 ± 1.2	20.0 ± 4.0
^{167}Tm	208	A	9.2	0.41 ± 15.0	6.12 ± 1.3	11.3 ± 4.0
^{171}Lu	740	A	8.2	0.48 ± 2.0	6.31 ± 1.4	2.9 ± 4.0
^{175}Hf	343	A	70	0.87 ± 1.0	6.51 ± 1.4	6.6 ± 4.0
^{185}Os	646	B	94	0.81 ± 1.2	7.00 ± 1.5	5.8 ± 4.0
^{188}Pt [b]	195	A	10.2	0.19 ± 5.4	7.15 ± 1.5	12.2 ± 4.0
^{191}Pt	539	A	2.9	0.14 ± 5.1	7.29 ± 1.6	4.2 ± 4.0

[a] % error in (1-S.C.).

[b] Only two points in MASH decay curve.

TABLE 6.1 (continued)

Isotope	C_{sum} ±%	G_{geo} ±%	σ (mb)	$\sigma(Au)/\sigma(p)$ [c]	$\sigma(Au)/\sigma(p)$ [d]
^{121}Te	-	0.935 ± 2.9	27.1 ± 3.5	3.82 ± 0.59	4.68 ± 0.67
^{127}Xe	0.87 ± 1.6	0.945 ± 2.6	33.2 ± 4.8	3.49 ± 0.55	-
^{131}Ba	0.76 ± 3.1	0.935 ± 2.9	43.8 ± 7.8	4.71 ± 0.89	5.33 ± 0.99
^{145}Eu	0.96 ± 0.4	0.942 ± 2.9	38.7 ± 5.3	2.98 ± 0.45	4.81 ± 0.76
^{155}Tb	-	0.925 ± 2.9	38.9 ± 9.7	-	3.25 ± 0.77
^{167}Tm	-	0.927 ± 2.9	19.9 ± 4.3	1.28 ± 0.29	1.68 ± 0.38
^{171}Lu	-	0.940 ± 2.9	64.5 ± 8.0	3.73 ± 0.52	4.67 ± 0.79
^{175}Hf	0.99 ± 0.1	0.930 ± 2.9	65.9 ± 8.2	3.72 ± 0.52	2.87 ± 0.40
^{185}Os	-	0.957 ± 2.6	92.6 ± 10.9	4.25 ± 0.60	-
^{188}Pt	-	0.926 ± 2.9	90.4 ± 12.4	4.37 ± 0.67	5.81 ± 0.97
^{191}Pt	-	0.935 ± 2.9	306.9 ± 44.2	-	-

[c]Proton cross sections from Kaufman[24] at 11.5 GeV.

[d]Proton cross sections from Hill (unpublished) at 28.0 GeV.

TABLE 6.2. Parameters for Co nuclear products
and cross sections.

Isotope	E (keV)	Det.	$T_{1/2}$ (d)	b ±%	S.C.±% [a]	ϵ ±%
^{44}Sc	271.1	D	2.44	0.866 ± 1.4	7.0 ± 4.3	7.10 ± 5.0
^{47}Sc	159.4	D	3.34	0.68 ± 2.0	7.5 ± 4.6	11.0 ± 5.0
^{48}V	983	D	15.98	1.00 ± 0.2	7.6 ± 4.7	1.90 ± 5.0
^{52}Mn	744	D	5.59	0.90 ± 2.0	8.3 ± 5.1	2.56 ± 5.0

Isotope	C_{sum} ± %	G_{geo} ± %	σ (mb)	$\sigma(Au)/\sigma(p)$ [b]
^{44}Sc	0.730 ± 3.7	0.955 ± 4.9	40.3 ± 5.7	8.96 ± 1.35
^{47}Sc	-	0.950 ± 4.9	14.8 ± 2.0	6.12 ± 0.92
^{48}V	0.756 ± 3.2	0.970 ± 4.9	40.5 ± 5.9	5.03 ± 0.76
^{52}Mn	0.760 ± 4.2	0.970 ± 4.9	30.9 ± 4.5	6.34 ± 0.94

[a]% error in (1-S.C.).

[b]Proton cross sections from Hill (unpublished) at 28.0 GeV.

TABLE 6.3. ED cross sections.

Isotope	Total Value	Nuclear	ED
^{196}Au	9.43 ± 0.75 barns	267 ± 67 mbarns	9.16 ± 0.75 barns
^{195}Au	2.42 ± 0.30 barns	126 ± 33 mbarns	2.30 ± 0.30 barns
^{58}Co	2.04 ± 0.25 barns	258 ± 60 mbarns	1.78 ± 0.26 barns
^{57}Co	413 ± 52 mbarns	119 ± 28 mbarns	294 ± 59 mbarns

As can be seen in Fig. 5.11, the ratio of Au to p remains constant at about 3 for products other than ^{196}Au. The extreme departure from 3 for ^{196}Au is evidence of the prominent role that ED plays in the creation of that isotope.

Once the nuclear part of the cross section was determined, the ED cross section was calculated by subtracting the nuclear part from the total

$$i.e.\ \sigma_{ED} = \sigma_{total} - \sigma_{nuclear}.$$

The ED cross-sections are summarized in Table 6.3. A summary of the parameter values used for the one and two neutron out Au and Co reaction products can be seen in Table 6.4. The last row of the table gives the energy of the gamma-ray used.

Error Analysis

As can be seen in Table 6.3, the uncertainty in the ED cross sections ranges from a low of 8.2% for $\sigma(^{196}\text{Au})$ to a high of 20.0% for $\sigma(^{57}\text{Co})$. In each of these cases (as well as all the rest of the cross section calculations) the error is a combination of statistical and systematic errors. While the analysis of statistical errors is often more

TABLE 6.4. Parameters used in cross section calculations.

Parameter	^{196}Au	^{195}Au
A_s (cnts/d)	58,576 ± 2.3%	630,701 ± 1.8%
$S.C.$	0.018 ± 102%	0.0 ± 4.2 %
A_t (g/mole)	197	197
T_{rad} (d)	0.306 d	1.188 d
N_{proj}	2.14x10^8 ± 4.0%	1.77x10^{11} ± 10.4%
$\rho(mg/cm^2)$	99.08 ± 0.58%	36.07 ± 1.4%
ϵ	0.0369 ± 4.0 %	0.173 ± 4.0%
b	0.870 ± 1.2%	0.109 ± 4.6%
C_{sum}	0.936 ± 2.7%	0.835 ± 3.1%
G_{geo}	0.973 ± 3.8%	0.934 ± 2.6%
G_γ	0.987 ± 0.05%	0.907 ± 0.3%
Eγ(keV)	355.6	98.9

Parameter	^{58}Co	^{57}Co
A_s (cnts/d)	2.94x10^6 ± 0.13%	3.74x10^6 ± 0.24%
$S.C.$	0.020 ± 3.8%	0.054 ± 1.1%
A_t (g/mole)	58.9	58.9
T_{rad} (d)	1.135 d	1.135 d
N_{proj}	1.60x10^{11} ± 10.4%	1.60x10^{11} ± 10.4%
$\rho(mg/cm^2)$	47.94 ± 1.4%	47.94 ± 1.4%
ϵ	0.022 ± 5.0%	0.153 ± 5.0%
b	0.995 ± 0.3%	0.855 ± 0.4%
C_{sum}	0.95713 ± 0.45%	1.00
G_{geo}	0.968 ± 4.3%	0.950 ± 4.9%
G_γ	0.998 ± 0.0	0.993 ± 0.0
Eγ(keV)	810.8	122.1

mathematically complex, it is less subjective and therefore more reliable.

There were several parameters for which a statistical error was appropriate. An example of such an error is the geometrical beam factor. As was discussed in the experiment chapter BLMs were placed in the beamline and then cut into concentric sections each of which were counted for activity in a NaI well counter (see Figs. 4.1 and 4.8). The center section of the BLM located behind the 36 mg/cm^2 was counted one hour and 48 minutes after the end of the irradiation. It had a total number of counts equal to 9356 over a 20 minute period (N=9356) or a total count rate of

$$count\ \ rate = \frac{9356\ counts}{20\ min} = 467.8\ CPM.$$

We assume a gaussian distribution for the count rate so that the uncertainty in N is equal to $\sqrt{N}$. The background rate was determined (with negligible error due to a very large number of counts) to be 97 CPM. We have then for the net count rate above background for the center section

$$\begin{aligned} count\ \ rate &= (467.8\ \ CPM - 97\ \ CPM) \pm \frac{\sqrt{9356}\ \ counts}{20\ \ min} \\ &= 370.8 \pm 4.8\ \ CPM. \end{aligned}$$

Another area in which a statistical analysis is needed is in a least squares fit. In the secondary correction (second row in Table 6.3), a weighted linear least squares fit was performed for the gamma-ray peak intensity of different target thicknesses. This is displayed in Fig. 5.12. Since the desired equation is linear in the parameters which are to be varied, the method of normal equations and subsequent Gaussian elimination on the coefficient matrix[25] was used to determine the coefficients c and

[25]D. Kahaner, C. Moler and S. Nash, *Numerical Methods and Software*, Prentice Hall, Englewood Cliffs, New Jersey 1989.

m in the equation

$$I/t = c + mt.$$

The statistical error in c and m was then calculated according to[26]

$$(\Delta c)^2 = \frac{1}{\rho}\sum \frac{t_i^2}{\sigma_i^2}$$

$$(\Delta m)^2 = \frac{1}{\rho}\sum \frac{1}{\sigma_i^2}$$

where σ_i is the uncertainty associated with t_i and ρ is the difference

$$\rho = \sum \frac{1}{\sigma_i^2}\sum \frac{t_i^2}{\sigma_i^2} - \left(\sum \frac{t_i}{\sigma_i^2}\right)^2$$

Since the fit function used in determining the area of gamma-ray peaks was not linear in its parameters (see Fig. 5.1), a nonlinear least squares method was used by the program MASTER[27] to arrive at the optimal fit function. The count intensity for a particular target was determined by counting that target for gamma-ray activity as depicted in Fig. 4.10. A typical spectra of these data consisted of 4096 channels with a number of counts associated with each one. As discussed above, the uncertainty in the number of counts N is equal to $\sqrt{N}$ so that the length of the error bars on the fit depicted in Fig. 6.1, for example, represent twice this error (i.e. number of counts in a channel = N $\pm\sqrt{N}$). The error bars on the points in Fig. 6.1 were the major contributor to the weights in the equation

$$Q = \sum_i w_i[y_i - f(x_i)]^2.$$

---

[26]P.R. Bevington, *Data Reduction and Error Analysis for the Physical Sciences*, McGraw-Hill, New York 1969.

[27]M.E. Nieland and C.A. Peterson, Master Fit Users' Guide, Ames Laboratory and Iowa State University, 1985.

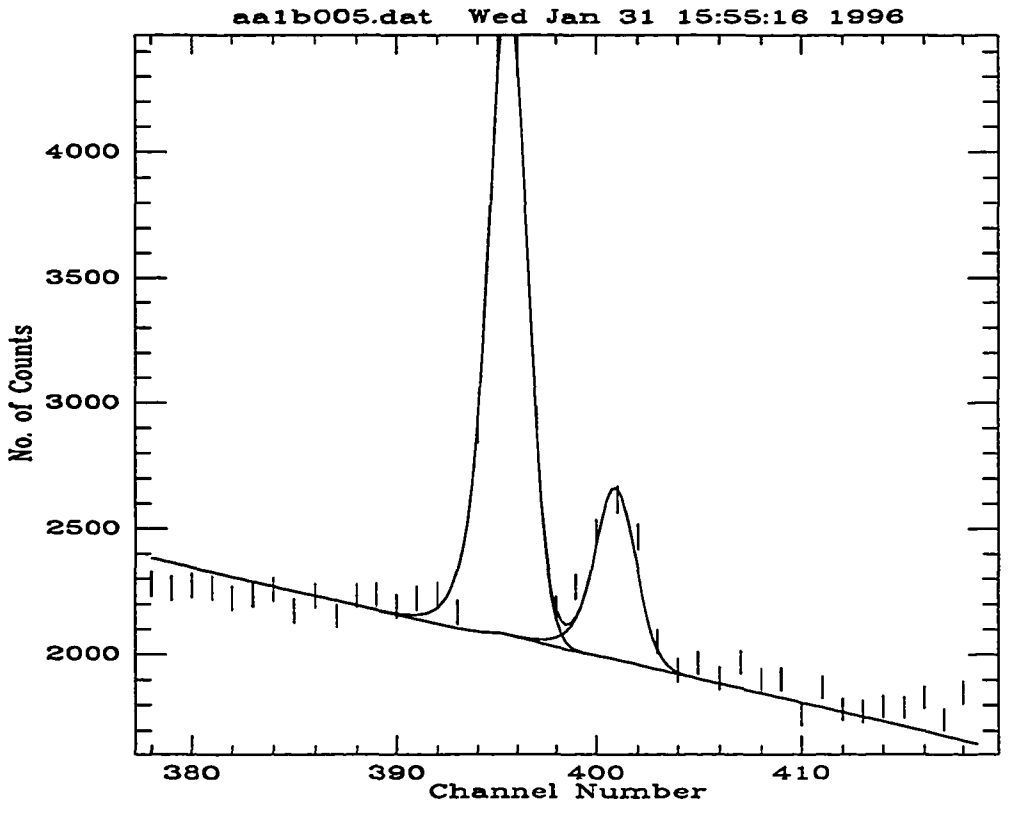

FIG. 6.1. Gamma ray peak fit showing error bars.

where in order to obtain the best fit, the value of Q should be a minimum. This involves solving a set of non-linear differential equations. To this end, a Taylor series expansion of Q is performed[28] about the initial guesses for the parameters α_{jo} in powers of the difference $\Delta = \alpha_j - \alpha_{jo}$. In this way a matrix equation is obtained, the solution of which yields new (and hopefully better) values of the parameters α_j. This process is iterated until convergence is achieved (defined by $\Delta <$ a chosen value) or a preset number of iterations have been performed. The error in the parameters are the diagonal elements of the inverted coefficient matrix.

The last statistical error is that calculated for the saturated activity (first row in Table 6.3). As was discussed in the data analysis chapter, the computer program MASH was used to extrapolate the saturated activity from the decay curve of a given target spectra (see Fig. 5.2). The error bars in figure 5.2 become the weights in a linear least squares fit and the error in the saturated activity is calculated in a fashion similar to the secondary correction discussed above.

The systematic errors are necessarily more subjective. The two most important were in the number of projectiles and in the detector efficiency. Since the low intensity run of 1993 was used as a "calibration" run for the other high intensity runs, the systematic error specific to it should first be discussed. As can be seen in Table 4.1 the difference in projectile count between the upstream telescope element and the prompt coincidences was 1.12% and between the 70% coincidences and the prompt coincidences the difference was 6.22%. The average of the two was 3.67%. As was

[28]W.C. Schick, Jr., "Skewgaus: A Fortran Program for Fitting Peaks in Semiconductor Detector Spectra"; report for The U.S. Atomic Energy Commission of Research under contract W-7405-eng-82; Ames Laboratory, Iowa State University, Ames, Iowa: 1974.

discussed in the Experiment chapter an interaction of approximately 2% of the beam nuclei with the scintillator nuclei in a telescope element could be expected based on the geometric cross section. Adding these two uncertainties in quadrature gave the 4.0% value for the final number of projectiles seen in the first column of Table 6.3. For the high intensity runs, there was no telescope to measure the beam intensity. As was discussed in the Experiment chapter, Beam Intensity Monitors (BIMs) were used to monitor the number of projectiles (see Fig. 4.2). Since the cross-section for producing ^{196}Au is used in determining the number of projectiles, the uncertainty in it is a lower limit for the uncertainty in the number of projectiles in the high intensity runs. This uncertainty added in quadrature with all of the other uncertainties in a cross section calculation lead to the 10.4% numbers seen in the number projectiles in the high intensity runs in Table 6.4.

In order to determine the efficiency of the HPGe detectors, a calibration source, Amersham QCD.1 Mixed Radionuclide Gamma-Ray Reference Source, was counted for gamma-ray activity. The results of these efficiency measurements can be seen in Table 6.2. These data were plotted on a log-log plot (see Fig. 6.2) and the efficiency for the 355.6 keV gamma-ray, for example, was interpolated between the two closest points. To arrive at the figure of 4% uncertainty seen in the seventh column of Table 6.1, an average of the uncertainty the efficiency of the four calibration points closest to 355.6 keV (165.9, 279.2, 391.7 and 514) was taken to get 3.63. This was rounded up to 4.0 to allow for error in interpolation. The uncertainty in the efficiency of detector D which was used to count the cobalt targets and detector A which was used to count the high intensity gold targets was computed in a similar fashion. The uncertainty in the summing corrections and the geometrical factors

TABLE 6.5. Amersham calibration source - detector B efficiency.

Isotope	E (keV)	$T_{1/2}$ (d)	11/1/94 dN/dt(s^{-1})	5/19/95 dN/dt(s^{-1})	Δ dN/dt %
^{109}Cd	88.1	462	685	508	4.0
^{57}Co	122.1	272	624	375	2.1
^{139}Ce	165.9	138	733	268	2.0
^{203}Hg	279.2	46.6	2119	108	2.5
^{113}Sn	391.7	115	2235	670	4.9
^{85}Sr	514.0	64.8	4304	507	2.3
^{137}Cs	661.7	30.2 (y)	2633	2600	2.4

	Position 1				Position 0			
Isotope	Area (cnts$\times 10^4$)	Δ Area (%)	ϵ (%)	$\Delta\epsilon$ (%)	Area (cnts$\times 10^5$)	Δ Area (%)	ϵ (%)	$\Delta\epsilon$ (%)
^{109}Cd	11.8	1.1	6.66	4.1	2.61	1.6	15.0	4.3
^{57}Co	10.2	7.8	7.80	8.1	2.53	0.9	19.7	2.3
^{139}Ce	6.65	0.9	7.14	2.2	1.72	1.3	18.7	2.4
^{203}Hg	1.70	4.3	4.65	5.0	0.463	0.8	12.5	2.6
^{113}Sn	7.63	0.6	3.28	4.9	2.05	0.6	8.91	4.9
^{85}Sr	4.61	0.6	2.66	2.4	1.21	0.7	6.95	2.4
^{137}Cs	18.6	0.9	2.02	2.6	4.85	0.5	5.44	2.5

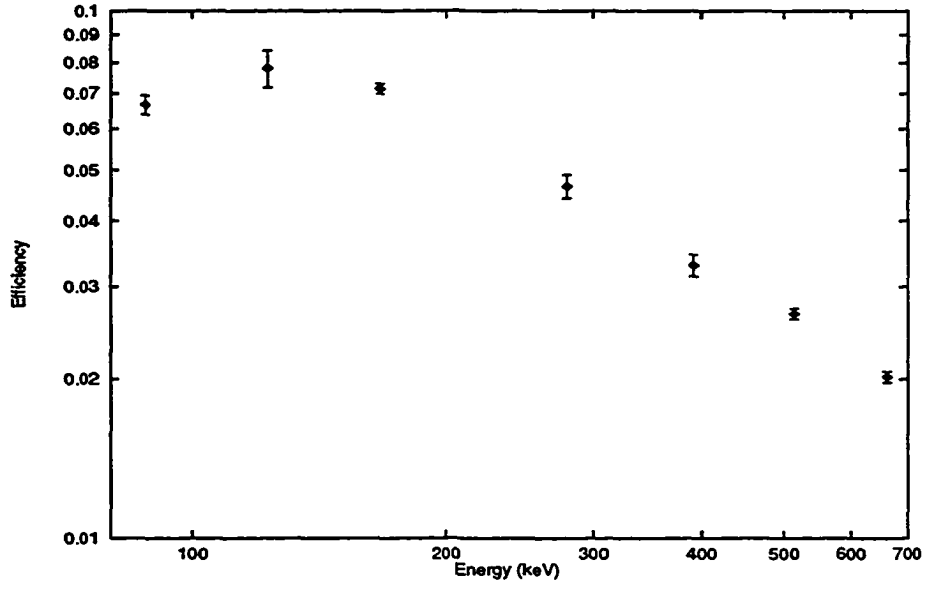

FIG. 6.2. Log-log plot of Efficiency of detector B using Amersham calibration source.

came from the fits used to determine the area of the gamma-ray peaks which were used in the graphs from which these corrections were determined. This is illustrated in Figs 5.15 and 5.16 respectively.

Interpretations

As mentioned in the theoretical chapter, the predictions of the WWF method are sensitive to the choice of minimum impact parameter b_{min}. The default value chosen for the predictions here is the one derived by Benesh, Cook and Vary[29]. The value is

$$b_{min} = r_0[A_t^{1/3} + A_p^{1/3} - x([A_t^{-1/3} + A_p^{-1/3})].$$

[29]C.J. Benesh, B. Cook and J. P. Vary, Phys. Rev. C 40, 1198 (1989).

TABLE 6.6. ED cross sections and
minimum impact parameter dependence.

Isotope	σ_{ED} (measured)	σ_{ED} (WWF) (b_{min}=default)
^{196}Au	9.16 ± 0.75 barns	10.52 barns (15.3 fm)
^{195}Au	2.30 ± 0.30 barns	1.64 barns (15.3 fm)
^{58}Co	1.78 ± 0.26 barns	2.13 barns (12.6 fm)
^{57}Co	294 ± 59 mbarns	284 mbarns (12.6 fm)

The first two terms represent the geometrical target/projectile size while the third term represents a curvature correction which becomes important for light nuclei. The parameters r_0 and x were varied to achieve a least squares fit to calculated (Glauber model) total cross sections for nucleus-nucleus interactions taking into account only the nuclear force. The nuclear densities used in the Glauber calculation were determined from electron scattering data. The best fit values are 1.34 fm and 0.75 for r_0 and x respectively. Using this equation for the minimum impact parameter, values for b_{min} of 15.3 fm and 12.6 fm were determined for Au on Au and Au on Co respectively. The predictions of the WWF theory using this value for the minimum impact parameter are summarized in Table 6.6. The value of minimum impact parameter needed to match theory with experiment becomes unphysical for neutron removal cross sections other than two neutron removal from Co. For the one neutron removal cross section, the value of b_{min} needed to match with experiment is 20.5 fm and 18.0 fm for Au and Co respectively. It is 7.5 fm for the two neutron removal from Au. The default impact parameter predicts a cross section 15.6% larger than the measured experimental value for ED one neutron removal from a Au target. Con-

TABLE 6.7. Relation of WWF predictions to experiment.

Cross Section	WWF Default	% Over/Under from Experiment
$\sigma(^{196}Au)$	10.5 b	+15.6
$\sigma(^{195}Au)$	1.6 b	-31.9
$\sigma(^{58}Co)$	2.1 b	+18.0
$\sigma(^{57}Co)$	284 mb	-3.4

versely, the two neutron cross section is underpredicted by the WWF method. The default impact parameter predicts a cross section 31.9% smaller than the measured experimental value. These predictions for Co and Au are summarized in Table 6.7.

The trend depicted by Table 6.7 is a familiar one. In a series of RHI experiments performed at the Bevalac with energies in the range of 1 to 2 GeV/nucleon, there has been a history of the WWF theory overpredicting the one neutron out cross section for the reaction $^{197}Au(RHI,X)^{196}Au$ if the RHI has $A \geq 56$ (see Ref. 15 and Ref. 16 in Background chapter). However for $A<56$ the WWF theory underpredicts the one neutron out cross section (see also Ref. 15 and Ref. 16 in Background chapter). The two neutron out cross section[30] does not have a similar cross over dependence on target A with similar previous measurements reporting an underprediction of the two neutron out cross section regardless of projectile A. A similar phenomenon occurs for Co with an overprediction for the reaction $^{59}Co(^{56}Fe,X)^{58}Co$ and an under prediction for the reaction $^{59}Co(^{20}Ne,X)^{58}Co$ (see Ref. 15 in Background chapter). The two neutron Co cross section reported here is difficult to compare to previous measurements since it is only with this experiment that the ED cross section significantly (greater than a factor of two) exceeds the nuclear cross section.

[30] J. C. Hill *et al.*, Phys. Rev. C **39**, 524 (1989).

It is of interest to compare the results of this experiment with a similar one conducted at a lower energy. Recently Aumamann *et al.*[19] bombarded ^{197}Au targets with a 1 GeV/nucleon Au beam as well as with other beams at the SIS synchrotron at GSI Darmstadt. In Fig. 6.3 we see a plot of the Au one and two neutron removal cross section as a function of the Au beam energy. As can be seen in the plot, at higher energies the deviation (over prediction) from the WWF predictions becomes more pronounced in the one neutron case. However, in the two neutron case the WWF prediction underpredicts the cross section for both low (46 %) and high (32 %) energies.

There is, unfortunately, no low energy (1 GeV) data for a Au beam on a Co target with which to compare this data. The energy dependence of the one and two neutron removal cross sections along with the experimental values for Co can be seen in Fig 6.4.

Recently Benesh[31] has raised the idea of quadrupole (as opposed to just giant dipole resonance) contributions to the ED cross sections. However, since this would raise the already overpredicted one neutron out cross section, it is unclear if this would help the WWF predictions. It could do so for the two neutron out cross section though. In addition to quadrupole corrections, a fully quantum mechanical treatment has been developed which seems to better predict the data.[32] In this work no reference is made to a classical trajectory so the kinematics can be treated correctly. The exchanged photon has a spacelike momentum ($q^2 < 0$) so that the cross section is not just a simple integral over the real photon cross section. The

[31] C. J. Benesh, Phys. Rev. C 46, 2635 (1992).

[32] C. J. Benesh and J.L. Friar, Phys. Rev. C 48, 1285 (1993).

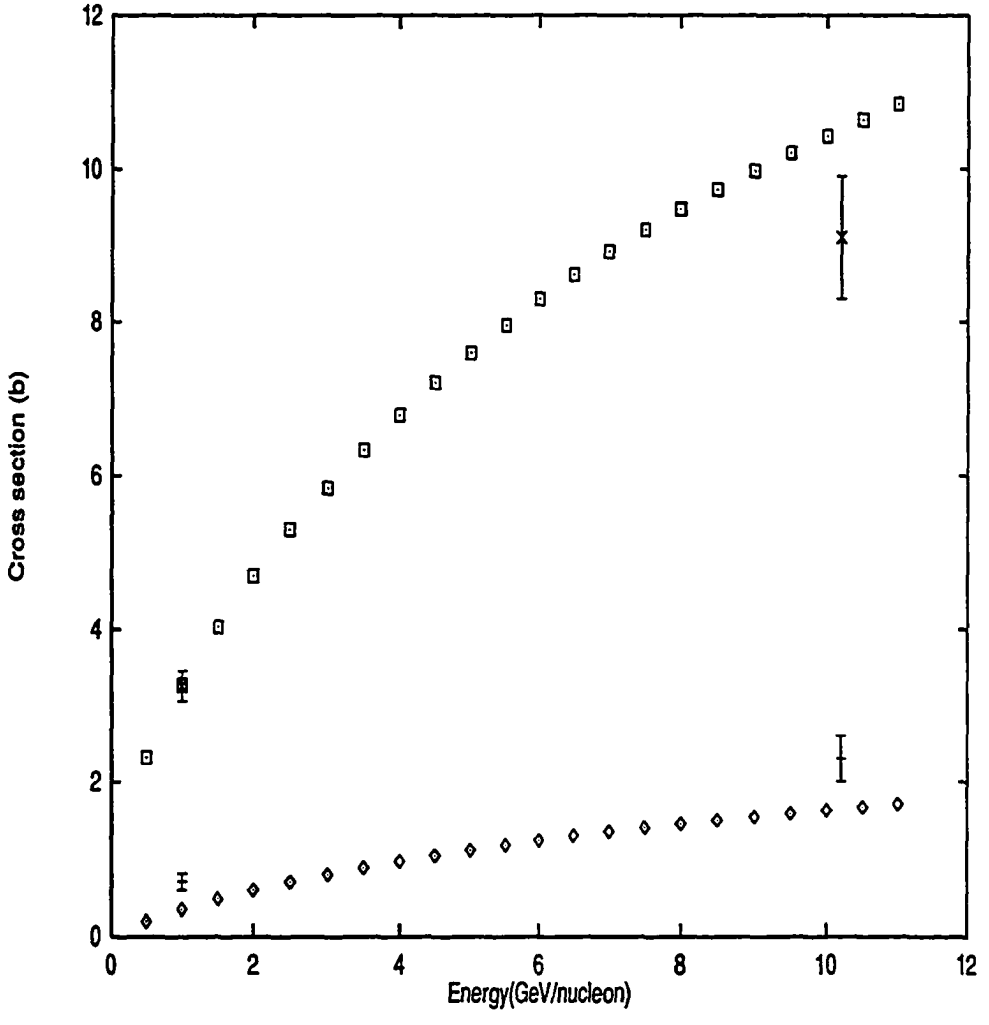

FIG. 6.3. Top: WWF energy dependence for one neutron removal ED cross section from a Au target by a Au beam. Experimental values at 1 GeV/nucleon from Aumann *et al.*[30] and at 10.2 GeV/nucleon from this work. Bottom: WWF energy dependence for two neutron removal ED cross section from a Au target by a Au beam. Experimental values at 1 GeV/nucleon from Aumann *et al.*[30] and at 10.2 GeV/nucleon from this work.

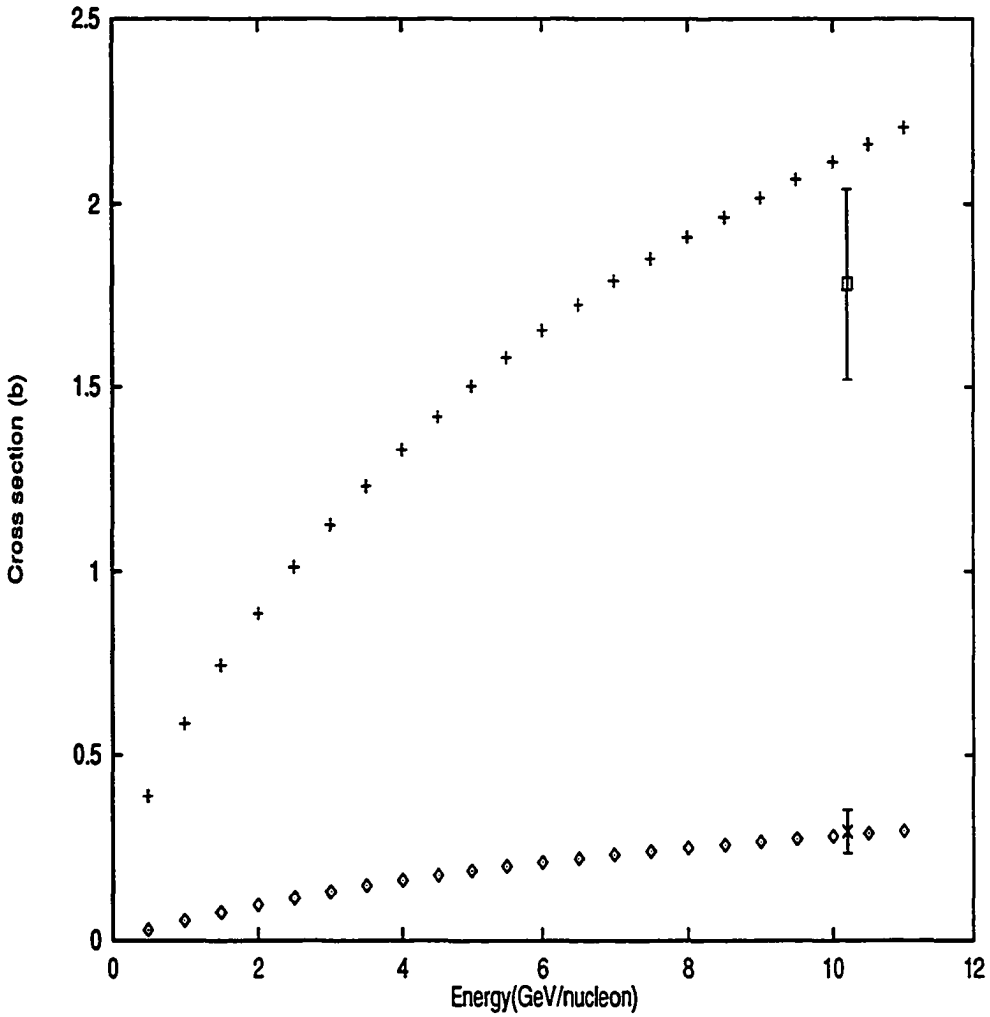

FIG. 6.4. Top: WWF energy dependence for one neutron removal ED cross section from a Co target by a Au beam and experimental value. Bottom: WWF energy dependence for two neutron removal ED cross section from a Co target by a Au beam and experimental value.

minimum impact parameter gets replaced by a maximum momentum transfer

$$i.e.\ q_{max} = 1/b_{min}.$$

If this q_{max} is used as a cutoff for the maximum transverse momentum transfer, the one neutron ED removal cross section for a 10 GeV/nucleon Au beam on a Au target is reduced by approximately 10% in better agreement with the data than the semi-classical WWF.

CHAPTER 7. TESTING OF LATE ENERGY TRIGGER BOARDS FOR STRANGELET SEARCH EXPERIMENT E864

Introduction to Strange Matter

Beginning with cosmic-ray experiments conducted in the late 1940s,[33] it has been observed that certain particles behave unusually. This "strange" behavior is manifested in the fact that although the particles are created via the strong force (inferred from their copious production) their relatively long lifetime, $\sim 10^{-10} sec$, indicates that they decay via the weak force. It is now well known and experimentally verified that this behavior results from the existence of the strange quark. Ten years ago, Witten proposed that strange quarks could combine with up and down quarks to form Strange Quark Matter (SQM) which, under certain conditions, could have a lower energy per baryon than regular matter[34]. This is due to the fact that although strange quarks have a larger mass[35] than up or down quarks ($\sim 100 MeV$ *vs.* $\sim 10 MeV$), up and down quarks occupy low level energy states and the Pauli exclusion principal limits the number of up and down quarks in these states. In contrast strange quarks can occupy the same low lying states since they are

[33] R.P. Feynman, *The Theory of Fundamental Processes*, Addison-Wesley, Inc., Redwood City, CA 1987.

[34] E. Witten, Phys. Rev. D 30, 272 (1984).

[35] Hikasa *et al.*, Phys. Rev. D 45, VI.44 (1992).

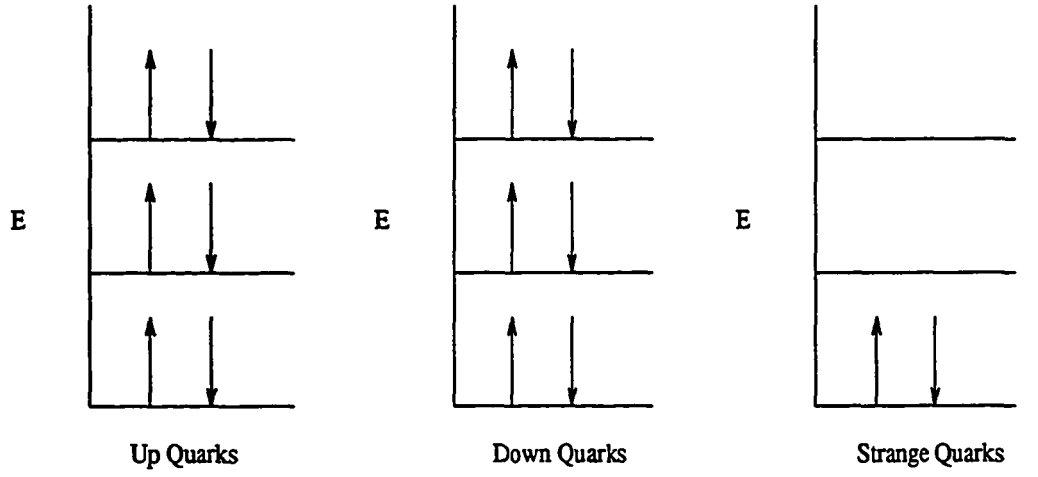

FIG. 7.1. Energy diagram for a non-interacting Fermi gas model of SQM.

not identical to up and down quarks. That this could be true can be seen by applying the model of an interacting Fermi gas to a system of quarks as is depicted in Fig. 7.1. If in fact SQM (with large A) does have a lower energy per baryon than ^{56}Fe (lowest energy/baryon of regular matter), it would be the true ground state of any matter. This possibility, if true, would have profound consequences. Among them are a possible new understanding of the astrophysics of neutron stars and pulsars and a whole new field of nuclear physics unconstrained from the coulomb repulsion imposed size restriction of nuclei, as will be explained later in this section.

In this chapter, the testing of a custom made circuit board (Late Energy Trigger (LET) board) to be used in experiment E864 (strangelet search) at the AGS at BNL will be described. First a general review of strange matter searches will be given, followed by a description of the experiment in which the above referred to circuit boards will be utilized. The testing equipment and procedure will then be described in detail followed by a discussion of the results.

There have been several different search methods that attempted to discover SQM. A method in the field of astrophysics involves the search for pulsars with very short periods. Currently, a pulsar is thought to be a neutron star that is rapidly rotating. This rapid rotation, along with the intense magnetic fields believed to exist at the surface of the star, lead to the periodic electromagnetic signals associated with a pulsar. If SQM exists in the universe, it has been proposed that a strange matter star (a neutron star with a core partially or wholly composed of SQM) could create a pulsar with a very short period (sub-millisecond). This would be due to the extreme density that would characterize a strange matter pulsar. To date, no sub-millisecond pulsars have been detected[36].

Another search method is via heavy ion bombardment[37]. If strange matter exists on earth, a sample of material that may contain it could be bombarded with low energy heavy ions. The coulomb barrier would prevent these ions from interacting with any normal matter that the sample contains. However strange matter is predicted to have a lower energy coulomb barrier. This is due to the fact that since the strange quark has a charge of (-1/3)e, strange quark matter would have a lower positive charge than regular nuclear matter and in fact would be electrically neutral if it had an equal number of up, down and strange quarks. Since it would have a lower coulomb barrier, a low energy (few MeV/nucleon) nucleus that would be repelled by nuclear matter could penetrate SQM. Then, depending on the size (A large $\rightarrow$ low E/A) of the SQM and the mass of the strange quark (small $m_s \rightarrow$ low E/A) [38] it is possible that SQM could be the true ground state of all matter. If this

[36]H. J. Crawford and C.H. Greiner, *Scientific American*, January, 1994, 72-77.

[37]E. Farhi and R.L. Jaffe, Phys. Rev. D **32**, 2452 (1985).

[38]J. Madsen, *Proceedings of the International Workshop on Strange Quark Matter*

were true, since the low energy nucleus has more energy/baryon than the strange matter that it penetrated, it would be converted into strange matter and the excess energy would be radiated in an isotropic burst of photons. This method of detection has been attempted with no positive result[36]. Another consequence of this lower coulomb charge would be the fact that large A chunks of strange quark matter would be more stable against fission than regular nuclear matter. This is due to the lower value of coulomb repulsion which limits the size of regular stable nuclear matter to $A \sim 300$.

Experiment E864

As distinct from a strange matter search, experiment E864 is designed to *create* strange matter and then detect it. In Fig. 7.2 we present a schematic as viewed from above of experiment E864. In the experiment, a 10 GeV/nucleon Au ion from the AGS collides with a target in the target box to (possibly) form strange matter. The formation of strange matter would take place with highest probability in a central collision due to the high strangeness and baryon number density. To this end the experiment uses a multiplicity trigger.

The multiplicity trigger is designed to trigger on only the 10% most central events. To determine how to achieve this cut, a Monte Carlo simulation was conducted which produced a scatter plot of integrated dE/dx (total energy lost in the scintillator) vs impact parameter for 1000 Au-Au collisions. For impact parameters ≤ 10 fm, the relationship between integrated dE/dx and impact parameter is approx-

in Physics and Astrophysics, Aarhus, Denmark, 1991, eds. J. Madsen and P. Haensel [Nucl. Phys. B (Proc. Suppl.) **24B** (1991)].

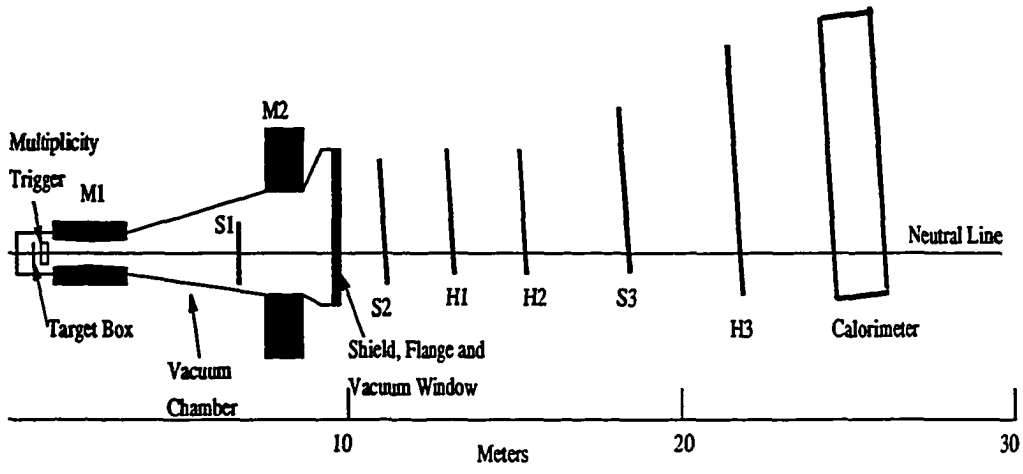

FIG. 7.2. M1 and M2 are dipole spectrometer magnets; H1, H2, H3 are scintillation counter hodoscopes; S1, S2, S3 are straw tube arrays.

imately linear. From the scatter plot a value of integrated $dE/dx = 0.16$ was found to give the desired 10% cut on centrality.[39] Physically the multiplicity trigger consists of a radially segmented scintillator with some lead shielding to block the delta rays formed when a Relativistic Heavy Ion (RHI) traverses the target. In operation, an RHI from the AGS would hit a target in the target box, and (hopefully) create a small piece of strange matter or "strangelet". This strangelet (if charged) would be deflected by M1 and M2, the dipole spectrometer magnets, and would eventually be deposited in the calorimeter if long lived enough, or decay in flight.

The calorimeter uses the "longitudinal spaghetti" design. It thus consists of long ($\approx$ 1m) thin (1mm diameter) scintillating fibers embedded in a Pb matrix and formed into 10cm by 10cm by 1m towers. The entire calorimeter consists of 754 towers. After drifting approximately thirty meters from the target to the calorimeter

[39] R.D. Majka and J. Sandweiss (Yale University) Spokesmen, E864 Proposal for Brookaven National Laboratory, 1991.

the putative strangelet would deposit its energy in the calorimeter. The strangelet would have sufficient energy so that a fraction of that energy would be deposited in the scintillating fiber as well as the larger cross-sectional area Pb matrix, thus creating a signal. This signal would be used for both Time Of Flight (TOF) and energy measurements. A characteristic the strangelet is predicted to have is that it will be relatively heavy and slow moving. Therefore, the experiment is designed to look for objects which are relatively heavy ($\geq$ 3GeV energy deposited in calorimeter) and relatively slow ($\geq$ 2.5ns longer drift time from interaction point to the calorimeter than a speed of light particle).

Late Energy Trigger (LET)

The LET consists primarily of 39 circuit boards (LET boards) mounted in three 9U VME crates along with two multiplicity boards and two OR boards. The 39 individual LET boards will have 16 time and 16 energy channels each, for a total of 39x16=624 (the actual number of channels in the fiducial volume will only be 616). The TOF measurement will begin with a start pulse from a beam counter gated by the multiplicity trigger. This will start a time to amplitude converter (TAC) on the LET board, TAC start. The TAC has a range of 50ns. The TOF measurement will end, TAC stop, with a stop pulse from the calorimeter. After the TAC stop signal has been received, the output of the TAC will be fed into a Flash Analog to Digital Converter (FADC). The energy measurement is determined using an integrator (INT). The INT is enabled by a signal from the beam counter. After the INT is enabled, integration is accomplished by collecting charge on an integrating capacitor and then measuring the voltage on the capacitor. The capacitor is charged by a current that is proportional

to the input voltage generated by the scintillation detected by a photomultiplier tube (PMT) from the calorimeter. The INT has 90ns in which to complete integration. The output of the INT is fed into a FADC. The FADC outputs of the TAC and energy signals form an ordered pair of numbers. The ordered pair corresponds to a location in a Look Up Table (LUT). A sample LUT configuration can be seen in Fig. 7.3. If the pair of numbers fall in the accept region of the LUT, i.e. the region occupied by 1's in Fig. 7.3, the LUT outputs a yes bit. If the pair of numbers fall in the reject region of the LUT, i.e. the region occupied by 0's in Fig. 7.3, no yes bit is output. The output of the LUT's are strobed using a pulse derived from the multiplicity pulse but delayed by 180ns. All of the 616 LET channels are ultimately OR'd together. If any one of the channels generates an OR, the event is saved. If not, the multiplicity board issues a fast clear to reset the system.

Each LUT consists of a 64Kx4 bit RAM and its data control circuitry. Only one quarter of the RAM is used. The LUT is computer controlled so that the contents can be loaded automatically. In this way it is possible to tailor a particular experimental run to look for different flight times, energies etc.

LET Board Testing

Test Setup

Prior to actually being used in experiment E864, the LET boards were thoroughly checked out. It is this board testing that forms the main topic of this chapter. The diagram in Fig. 7.4 illustrates how this testing was accomplished. As

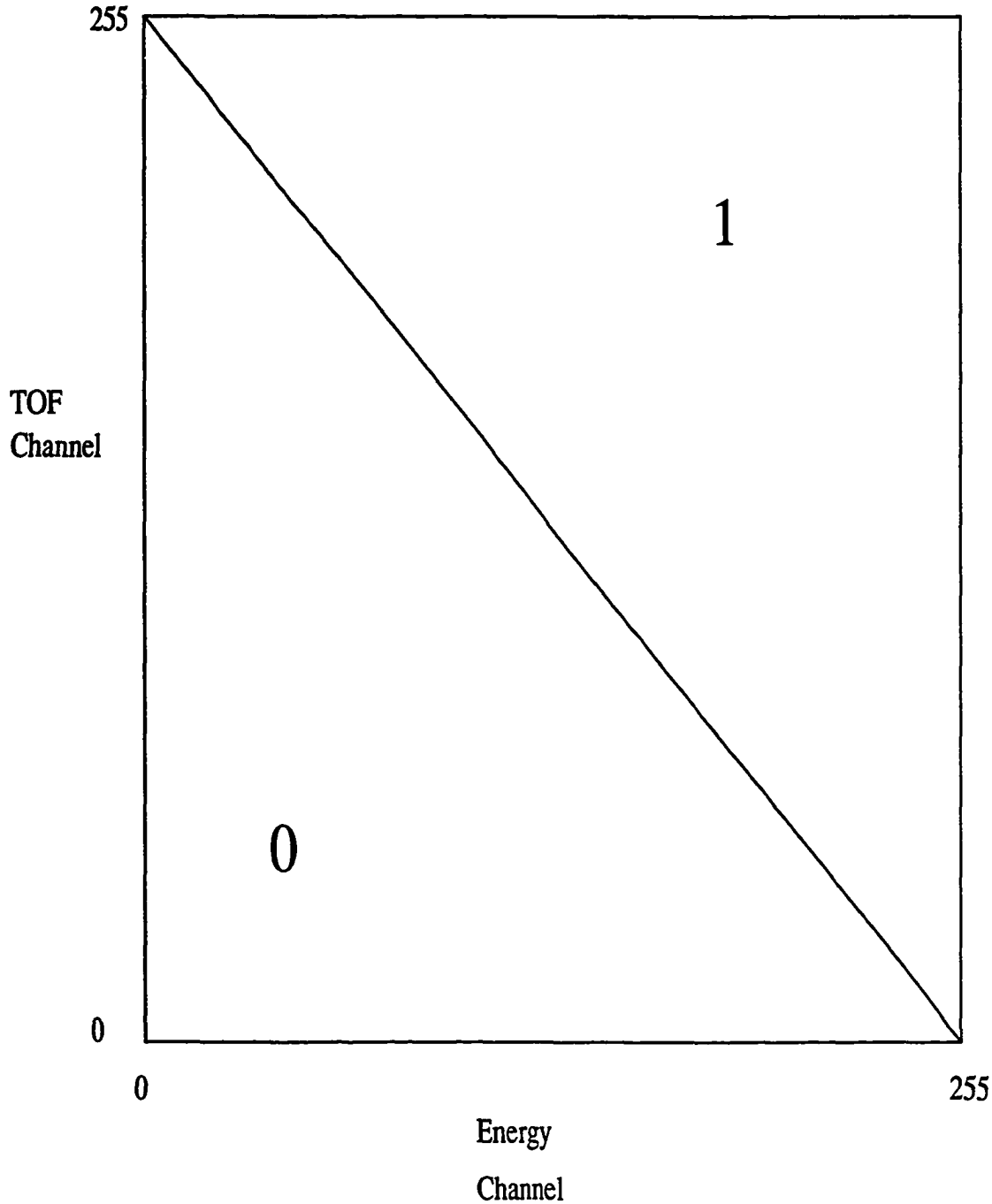

FIG. 7.3. Sample look up table configuration.

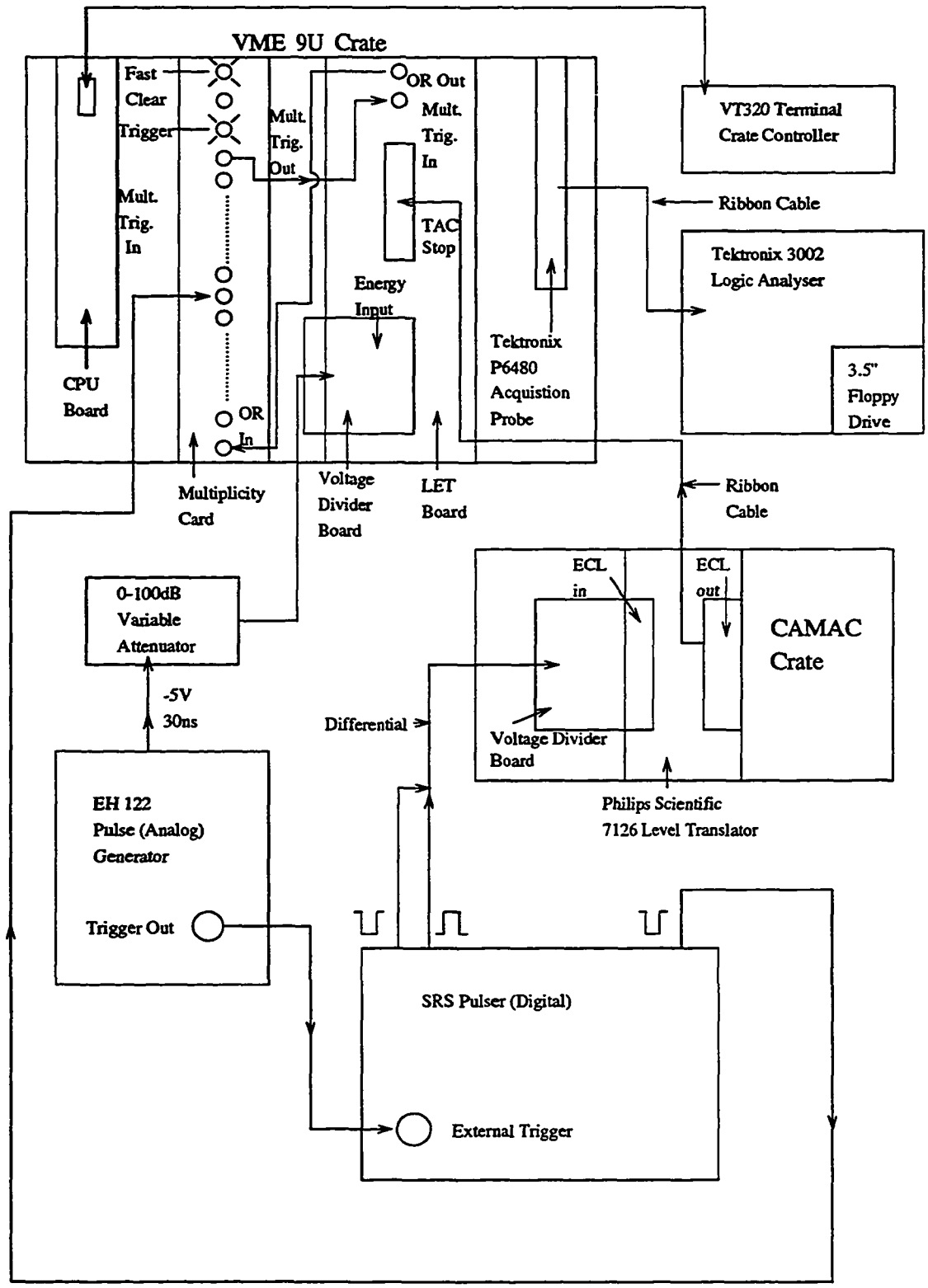

FIG. 7.4. LET board test set-up.

can be seen, a board to be tested was mounted in a slot in a 9U VME crate identical to the crate in which it would be mounted for the actual experiment. In addition to the LET board a multiplicity board was mounted in the crate. The multiplicity board acts as a fan out for the multiplicity pulse. In addition to being a fan out, the multiplicity board has lights indicating a trigger or a fast clear. The trigger light comes on if the multiplicity board gets an input signal that is consistent with the multiplicity pulse (30ns wide, -1.3V square pulse) and an OR pulse from the LET board. The fast clear light comes on if no OR pulse is detected after the LUTs have been strobed.

On the left side of the VME crate in Fig. 7.4 can be seen the CPU board. This board enabled communication to and from the LET board that was under test. Using the VxWorks operating system along with the VT320 terminal seen in the upper right-hand corner of Fig. 7.4, it was possible to read and write to the LUTs as well as read the status registers which contained the output of the FADCs.

When operating in the actual experiment, the function of the LET board is to distinguish between many different voltage pulses which may be interesting. These different voltage pulses will ostensibly represent the different TOFs to, and energy deposited in, the calorimeter of particles and interesting candidates created in the RHI collision. To test the LET board, these various different pulses needed to be recreated in the test laboratory. The three types of pulses needed were: 1) Multiplicity pulse - this pulse was input to the multiplicity board. It was meant to mimic the beam counter pulse . Once the multiplicity board receives this signal, it sends a TAC start signal to the LET board under test. 2) TAC stop - This is a digital pulse. The type of logic used is differential ECL. The timing relationship of

this pulse to the multiplicity pulse needs to be known very accurately ($\approx$ 1ns) since it is this pulse that measures the TOF of the RHI collision fragments. 3) Energy - This is an analog pulse. It is meant to mimic the energy pulse from the PMTs in the calorimeter.

In contrast to the digital pulser, the analog pulser did not need extremely precise timing characteristics. This was due to the fact that there was a 90ns window during which the energy pulse was to be integrated. The gross characteristics of the energy pulse should be similar to a PMT pulse, i.e. negative polarity, and roughly 30ns wide with an amplitude that could be varied from 0.0 to 1.0 V. The LET board has sixteen energy channels so that to satisfy the power needs of all sixteen channels, an analog pulser with a large power output (EH-122 vacuum tube pulser) was used. This pulser had the capability to deliver a -5V 100ns wide pulse. Even after this signal was split sixteen times to be delivered to each LET energy input, the signal proved to be large enough to drive the FADC into saturation.

Impedance Matching

To enable the analog voltage pulse to be delivered to the LET board, a passive voltage splitter was designed to impedance match the signal. A diagram of this system is shown in Fig. 7.5. As can be seen in the figure, it was necessary to match the single 50 ohm BNC output from the analog pulser to the 34 pin input on the LET board with each of the sixteen individual two pin inputs having an input impedance of 100 ohms. The seventeenth two pin input was grounded. The resistance value R on the voltage divider board is in series with the input impedance of 100

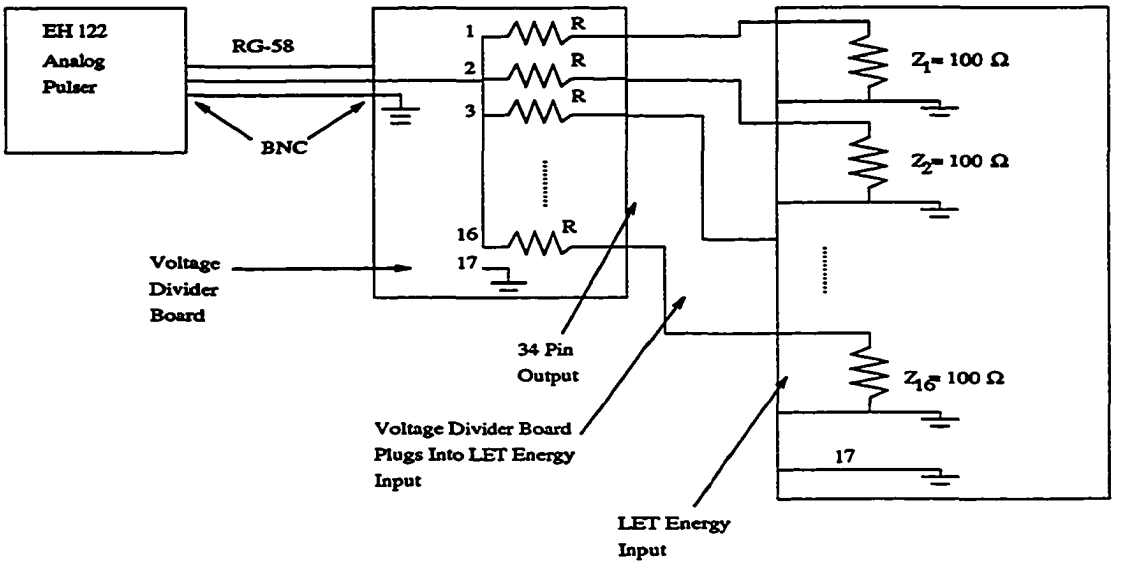

FIG. 7.5. Impedance matching network for energy input.

ohms in the LET board. These two series resistances were in parallel with each of the other fifteen inputs. Therefore, we require

$$\frac{R+100}{16} = 50 \Rightarrow R = 700.$$

A value of 680 ohms was readily available and this proved sufficient to successfully match the input.

In distinction from the analog/energy voltage divider, the digital TAC-stop signal required an active splitter. This active voltage splitter was constructed using a passive voltage divider board in conjunction with a Phillips Scientific CAMAC Model 7126 Level Translator. This is pictured schematically in Fig. 7.6. The digital pulser that was used was a Stanford Research Systems (SRS) DG535. It had the capability to output a differential ECL logic pulse. The accuracy of the pulser was ± 500ps for delay times less than 100ns. While this pulser was sufficient to drive a single TAC-stop signal, it did not have sufficient power to drive all sixteen TAC

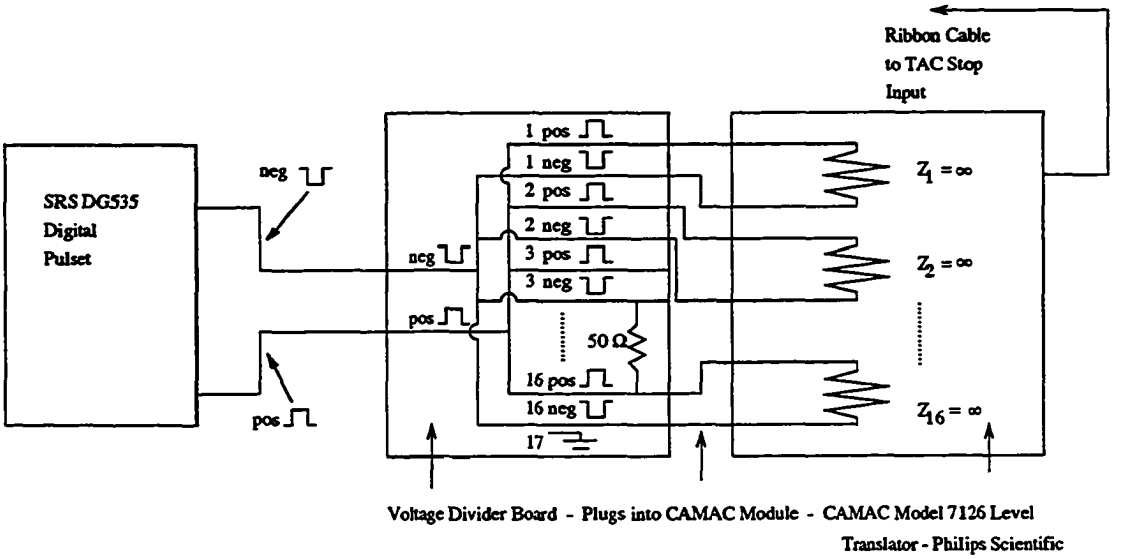

FIG 7.6. Impedance matching network for TAC stop input.

channels. If a channel by channel test was to be conducted, no further modifications to the system was needed. However, since a total of forty four boards were to be tested, with each board containing sixteen time and sixteen energy channels, testing each of them channel by channel was prohibitively time consuming. Therefore, to keep the precise timing requirements of the TAC stop signal and to be able to test all sixteen TAC channels simultaneously, an active voltage splitter was needed. From basic resistance and current circuit laws we know that power is equal to voltage times current, i.e.

$$P = IV.$$

For a fixed voltage, we require that the current drawn from the supply be below a maximum value, i.e.

$$I \leq I_{max}.$$

From Ohm's law, we also know that voltage is equal to current times resistance, i.e.

$$V = IR \ \ or \ \ I = V/R.$$

We see that for a fixed voltage, a low value of resistance requires a high value of current and visa versa. The Phillips Scientific CAMAC module had an input resistance which could be set at 5MΩ. By choosing this input resistance, the load impedance seen by the SRS pulser was made effectively infinite, much higher than the 100Ω input impedance of a single TAC stop channel. By constructing this type of network, the current drawn from the pulser was kept below the maximum value and in effect an active voltage splitter was created. To match the 50 Ω output impedance from the SRS pulser, a 50 Ω resistor was shunted across the positive and negative signals on the voltage divider board. This was in parallel with the ∞ input impedance of the CAMAC logic translator resulting in a 50 Ω load being seen by the SRS digital pulser.

Triggering/Timing

As referred to earlier, the time between the multiplicity pulse and the TAC stop pulse needed to be very precise. This relationship was an important consideration when configuring the trigger setup. The vacuum tube analog pulser was found to need a large pulse to externally trigger it. The digital pulser was again found to have insufficient power. In view of this fact, the analog pulser was used to trigger the digital pulser. This established a constant time relationship between the LET board under test, the analog pulser and the digital pulser. This relationship can be seen in Fig. 7.7. As can be seen in the figure, the pulse from the analog pulser

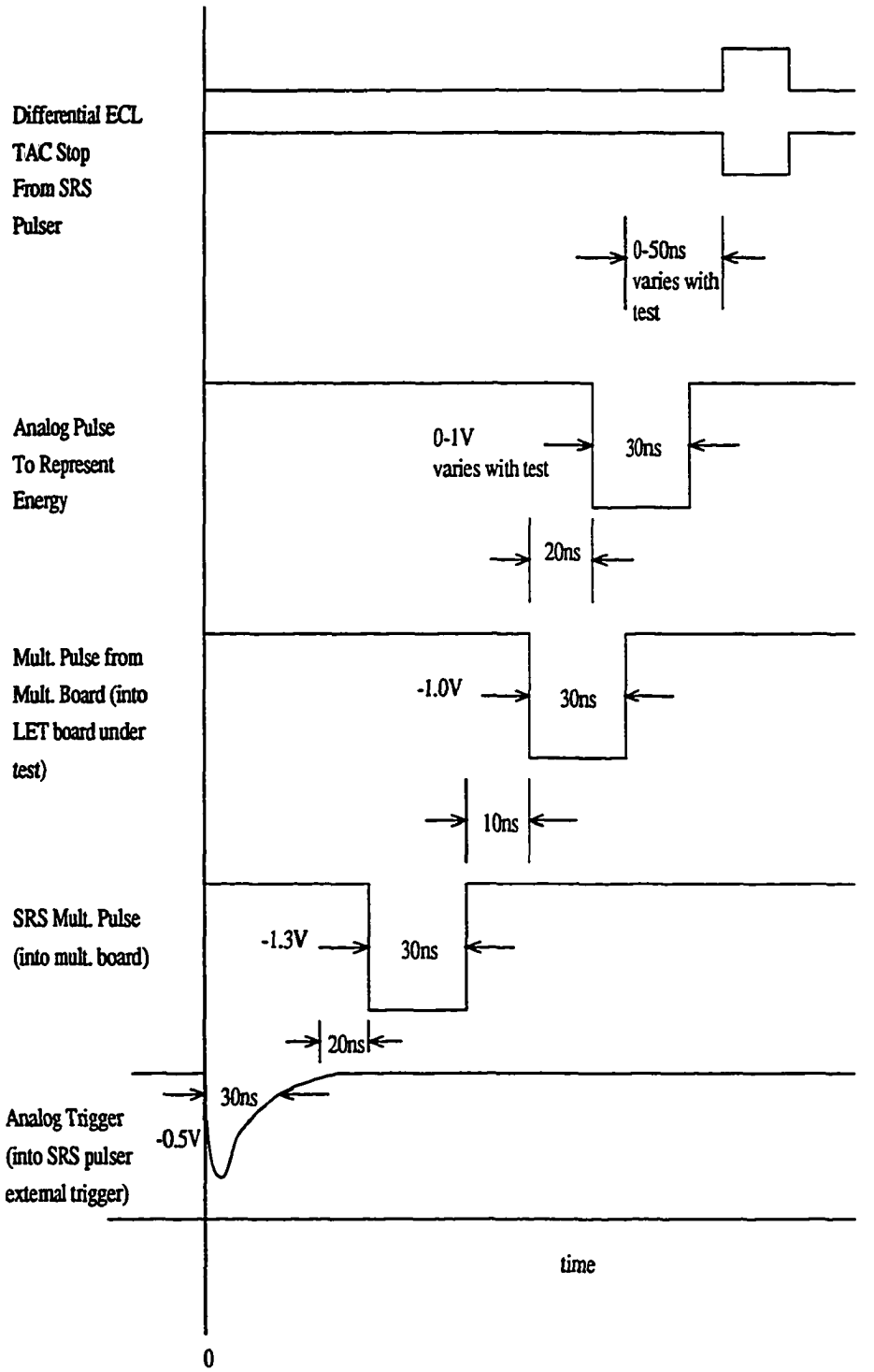

FIG. 7.7. Timing relationship for various pulses.

starts the whole process by externally triggering the SRS digital pulser. This in turn sends a pulse to the multiplicity board which then sends a trigger pulse to the LET board under test. Approximately 20ns after the leading edge of the trigger pulse from the multiplicity board, the analog energy pulse is sent from the EH-122 pulser. As was indicated earlier, there is a 90ns window for integration of the analog pulse to occur which allows for some variability in the timing of the analog energy pulse. The TAC stop pulse is generated by the SRS digital pulser between 0 and 58ns after the leading edge of the multiplicity pulse. The timing of this pulse with respect to the multiplicity pulse needs to be precise. Since the SRS digital pulser is responsible for both the multiplicity pulse and the TAC stop pulse, the only error introduced is due to the SRS pulser. By triggering in this fashion, it was possible to avoid the relative imprecision of the high power vacuum tube pulser.

Initial Board Inspection

Before the boards were tested, they were inspected and checked for flaws. This consisted of both visual and electrical tests. The visual inspection consisted of closely looking over all of the components on the board to insure that the assembly process was completed nominally. Since there were hundreds of components on each board, the possibility of a mistake happening in the manufacturing process was significant. An error that was found on several boards was solder bridges. This occurred when solder used to make electrical/mechanical connections for board components unintentionally shorted the electrical connection between individual component leads. This happened on approximately three boards. The visual inspection process also

found a broken resistor, missing screws and some missing leads among the 44 boards that were tested.

In addition to the visual inspection, there were electrical tests performed on the boards prior to taking data. One electrical test was associated with the address switches. The address switches were used by the computer controller to locate the LUT on different boards. They consisted of eight individual switches mounted on a single 1cmx2cm board component. The resistance across the leads corresponding to an individual switch should nominally read 10kΩ if it was open and $\sim 3\Omega$ if it was closed. The address switches were checked and all but one were found to be in working order. The other electrical test performed on the boards was to check the input into the FADCs.

The input to the FADCs comes through a fourteen pin op-amp SD5401CY. For either the TAC stop signal or the energy signal, the way in which the voltage pulse is characterized is to measure the amount of charge on a capacitor. In the case of the TAC stop, the amount of charge on the capacitor is made to be proportional to the time a collision fragment takes to reach the calorimeter and in the case of the energy signal, the amount of charge is proportional to the energy deposited in the corresponding tower of the calorimeter. To view this signal out of the op-amp, a Tektronix 2465 300MHz oscilloscope externally triggered by the multiplicity pulse was used. As can be seen in Fig. 7.8, the FADC input starts out at zero volts and charges to a maximum value of about 2.5V in a time of 50ns after the start of the charging process. Thus 50ns corresponds to the full range of the 8-bit FADC output. If a TAC stop signal is received earlier, or a smaller voltage energy pulse is delivered to the LET input, the voltage level seen by the FADC will be less. Although in Fig.

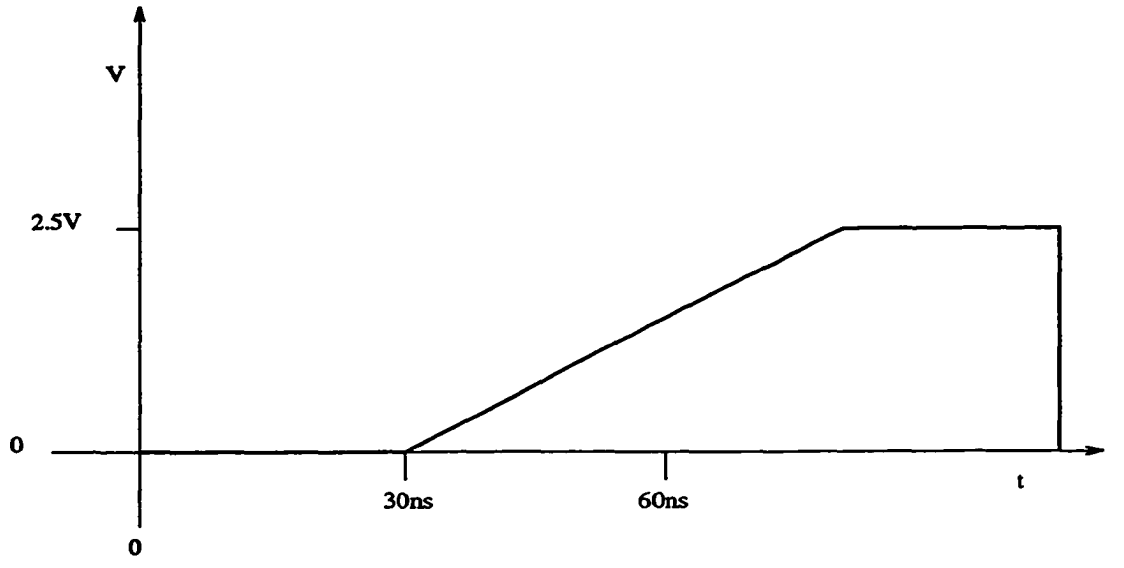

FIG. 7.8. Input to FADC.

7.8 the voltage level at zero time is zero, in general this turned out not to be the case. A small ($\sim$ 20mV) D.C. offset was usually present. Mounted on the board was a potentiometer that was used to set this D.C. level. On all of the boards, the potentiometers were adjusted so that this D.C. offset was zero for each of the sixteen energy and TAC stop channels. After this inspection was complete, the boards were ready to be tested with real data.

Data Taking

The energy and TOF channels were tested for linearity and rms fluctuations. To test the linearity of the channels, the input signals were varied in a linear fashion and the output of the channels was monitored. In Table 7.1, the various settings for the amplitude of the analog voltage pulse and the delay between the mul-

TABLE 7.1. Settings for LET board test.

Setting Number	1	2	3	4	5	6	7	8	9	10	11	12	13	14	15	16	17
Energy Atten (dB)	50	40	30	25	20	17	15	12	10	8	7	6	5	4	3	2	1
Time Delay (ns)	0	2	4	8	12	16	20	24	28	32	36	40	44	48	52	56	58

tiplicity pulse and the TAC stop pulse is given. With pulser output corresponding to setting number 1, both the analog energy and the TAC stop signals generate FADC outputs at pedestal values, i.e. $\approx$ 50 channels, for all 16 channels of all 44 boards. With pulser output corresponding to setting number 17, both the analog energy and the TAC stop channels generate FADC maximum outputs. This will be illustrated when the data results are reviewed.

The rms fluctuation tests were intended to measure the limits to the reproducibility of output due to inherent noise in the system. To test this, the pulser outputs were adjusted to setting number 9 and the test was repeated thirty times. This allowed a histogram to be plotted the width of which was proportional to the rms fluctuation. Again, this will be illustrated when the data results are reviewed.

The output of the FADCs is written to a status register located on the LET board. The CPU board mounted in a special slot in the 9U crate was utilized to read this data. By issuing commands from the keyboard that was connected to the CPU board it was possible to write from the status registers to the buffer on the CPU board. The contents of this buffer was then displayed on the VT320 terminal also connected to the keyboard. While this setup was sufficient for judging the performance of individual boards point by point, the amount of data that was to be taken for all of the boards made necessary a more automated setup. In particular, it was desired

to have a graphical display of the board performance. To this end a Tektronix 3002 Logic Analyzer with a 3.5" floppy drive was connected to the backplane of the VME crate via a Tektronix P6480 Acquisition Probe. This can be seen in the diagram of the entire setup in Fig. 7.4. During a board test, the logic analyzer reads signals transmitted over the backplane of the VME crate and then writes them to its own buffer. From there, they are displayed on the terminal screen to be monitored and written to floppy disc. With the data from the linearity and RMS fluctuation tests on floppy disc, it was much easier to graphically display this data in an efficient manner.

The output data from the FADC is written in hexadecimal format. This presented a minor problem in converting back to decimal format for graphical display. A slightly more serious problem involved extracting the real data from the surrounding superfluous data. This extra data resulted from the Tektronix probe picking up extra signals from the backplane of the crate and writing them to disc. To alleviate this problem, a computer program was written by postdoctoral associate Athan Petridis which extracted the needed data.

Testing Results

As referred to earlier, two tests (linearity and rms fluctuation) were performed on each of the channels of each of the LET boards that were tested. Figs. 7.9 and 7.10 display typical results of the linearity tests for the first channel of the TAC and energy signals for board number 1. As can be seen, the output of the LET board is linear over the range of interest. Figs. 7.11 and 7.12 display the results of the rms fluctuation tests of the first channel of the TAC and energy signals for board number 1. As can be seen, the rms fluctuation of the energy signal,

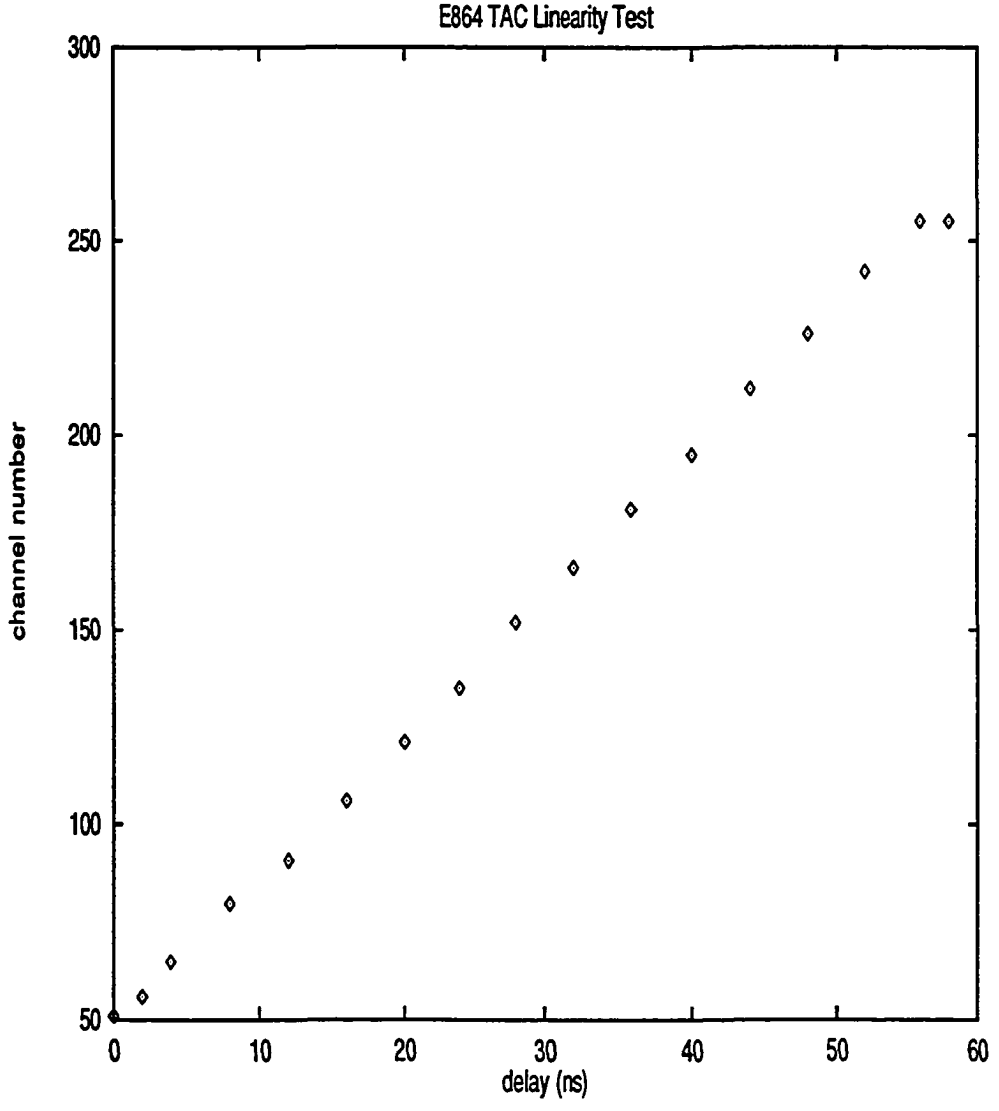

FIG. 7.9. Results of TAC linearity test.

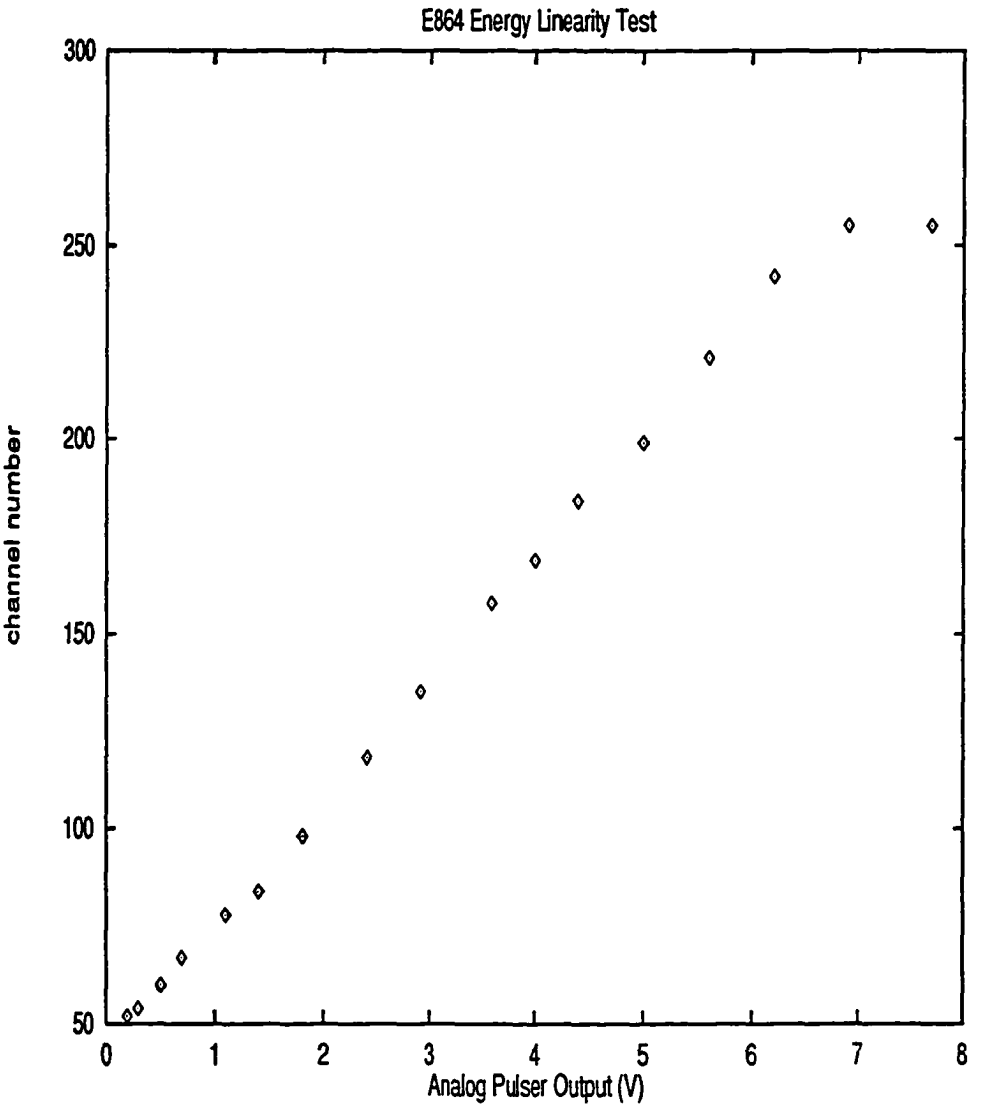

FIG. 7.10. Results of energy INT linearity test.

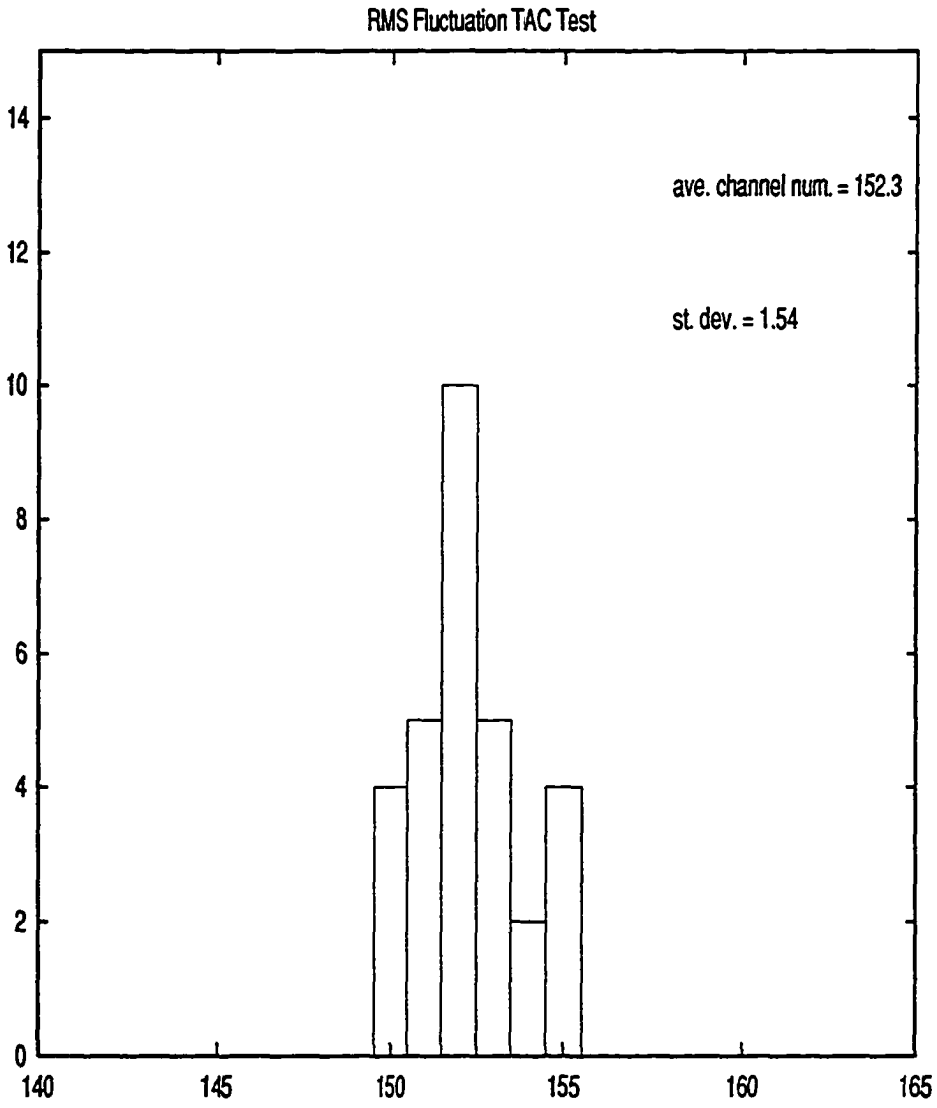

FIG. 7.11. Results of RMS TAC fluctuation test.

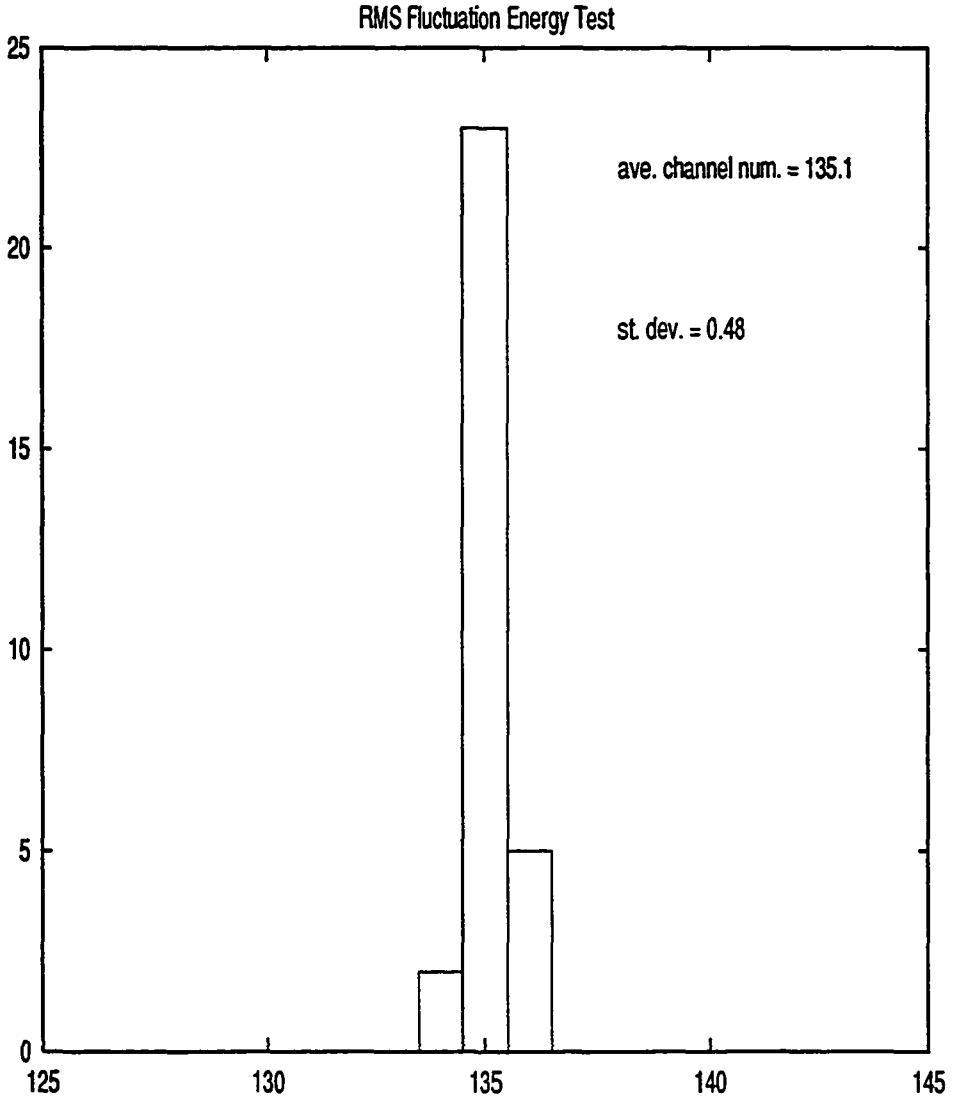

FIG. 7.12. Results of energy INT fluctuation test.

0.48 channels, is significantly better that the rms fluctuation of the TAC signal, 1.54 channels. This proved to be true for most channels of all of the boards that were tested. Since the mechanism for measuring the signal is the same for both the TAC and energy channels, namely measuring the charge on a capacitor, this difference was attributed to an instability in the test timing pulses.

Board Troubleshooting

The most common problem found when testing the boards was that one or more channels were found to be inoperative. Through the diligent work of Harold Skanks (the electrical engineer who designed the boards) and Gary Sleege, both engineers employed at the Ames Laboratory, these problems were traced and fixed. In most cases, the problem originated in a lead on a surface mount component that was not making proper contact. Another problem was that initially, in contrast to Fig. 7.8, a number of the TAC "ramps" were found to look like Fig. 7.13. This type of waveform was found to correlate with erratic performance on TAC channels. Upon further investigation, it was found that a capacitor and resistor involved with the TAC abort signal had improper values. The TAC abort signal is given if no TAC stop signal is received in a channel. If no TAC stop signal is received, the TAC abort prevents the voltage level from exceeding approximately 2.5 volts so as not to damage the FADC. The improper values of resistance and capacitance caused the voltage level of this signal to be low. Due to this low signal, the TAC abort circuit was not properly reset, therefore conditions were not right for acceptance of the next input signal. This resulted in the waveform seen in Fig. 7.13. as opposed to the proper waveform seen in Fig. 7.8. After replacing the resistor and capacitor

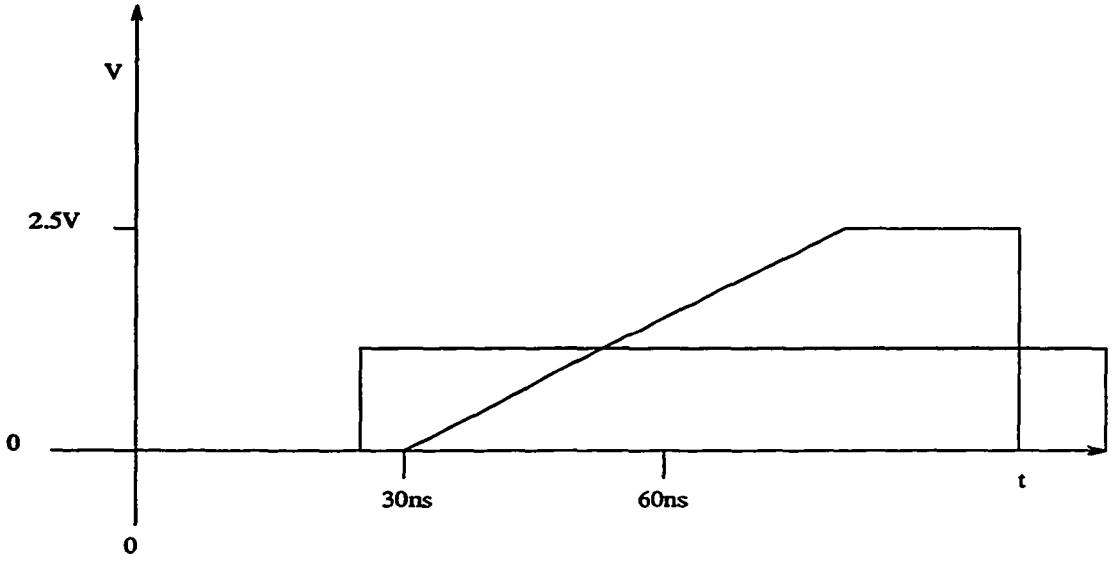

FIG. 7.13. Erratic waveform TAC input to FADC.

in question, this problem was solved.

Conclusion

Testing 44 LET boards for experiment E864 proved to be a remarkable learning experience. After manually testing the prototype LET board and graphing the output point by point, an appreciation develops for the efficiency of the final testing process. Additionally, after viewing the numerous problems associated with initial testing, the sense of relief after successfully completing the testing of 41 boards is significant. Initial indications are that the LET boards performed well in their first run in experiment E864. The final judgment will have to wait for further data analysis.

BIBLIOGRAPHY

T. Aumann *et al.*, Phys. Rev. C.**47**, 1728 (1993).

C. J. Benesh, Phys. Rev. C **46**, 2635 (1992).

C.J. Benesh, B. Cook and J. P. Vary, Phys. Rev. C **40**, 1198 (1989).

C. J. Benesh and J.L. Friar, Phys. Rev. C **48**, 1285 (1993).

C. Bertulani and G. Baur, Physics Reports **163** Nos. 5 & 6 (1988) 299-408.

C. Bertulani and G. Baur, Physics Today, **47**, 22 (1994).

H.A. Bethe and E.E. Salpeter, *Quantum Mechanics of One-and Two-Electron Atoms*, Plenum Publishing, New York 1977.

P.R. Bevington, *Data Reduction and Error Analysis for the Physical Sciences*, McGraw-Hill, New York 1969.

J. M. Blatt and V. F. Weisskopf, *Theoretical Nuclear Physics*, John Wiley & Sons, New York 1952.

E. Browne and R.B. Firestone, *Table of Radioactive Isotopes*, John Wiley & Sons, Inc., New York 1986.

H. J. Crawford and C.H. Greiner, *Scientific American*, January, 1994, 72-77.

J.P. Dufour et al, p321 *Proceedings of The First International Conference of Radioactive Nuclear Beams, 16-18 Oct. 1989* Teaneck N.J.: World Scientific Publishing Co., 1990.

E. Farhi and R.L. Jaffe, Phys. Rev. D **32**, 2452 (1985).

E. Fermi, Zeit. Physik., **29**, 315 (1924).

H. Gutbrod and H. Stöcke, *Scientific American*, November, 1991, 58-66.

S. S. Hanna *Proceedings of the Giant Multipole Resonance Topical Conference, 15-17 Oct. 1979*, Oak Ridge Tenn.

Hikasa *et al.*, Phys. Rev. D **45**, VI.44 (1992).

J.C. Hill *et al.*, Phys. Rev. Lett. **60**, 999 (1988).

J. C. Hill *et al.*, Phys. Rev. C **39**, 524 (1989).

H.H. Heckman and P.J. Lindstrom, Phys. Rev. Lett. **37**, 56 (1976).

J. D. Jackson, *Classical Electrodynamics.* John Wiley & Sons, Inc., New York 1975.

D. Kahaner, C. Moler and S. Nash, *Numerical Methods and Software*, Prentice Hall, Englewood Cliffs, New Jersey 1989.

S. B. Kaufman *et al.*, Phys. Rev. C. **14**, 1121 (1976).

W.L. Kehoe, "PHENIX Conceptual Design Report"; Brookhaven National Laboratory, Upton, N.Y. 1993.

T. Kobayashi, p325 *Proceedings of The First International Conference of Radioactive Nuclear Beams, 16-18 Oct. 1989* Teaneck N.J.: World Scientific Publishing Co., 1990.

K.S. Krane, *Introductory Nuclear Physics*, John Wiley & Sons, New York 1987.

L.D. Landau and E.M. Lifshitz, *The Classical Theory of Fields*, Pergamon Press, New York 1975.

W.R. Leo, *Techniques for Nuclear and Particle Physics Experiments*, Springer-Verlag, Berlin 1987.

W.J. Llope and P. Braun-Munzinger, Phys. Rev. C.**41**, 2644 (1990).

R.D. Majka and J. Sandweiss (Yale University) Spokesmen, E864 Proposal for Brookhaven National Laboratory, 1991.

J. Madsen, *Proceedings of the International Workshop on Strange Quark Matter in Physics and Astrophysics,* Aarhus, Denmark, 1991, eds. J. Madsen and P. Haensel [Nucl. Phys. B (Proc. Suppl.) **24B** (1991)].

M.T. Mercier *et al.*, Phys. Rev. Lett. **52**, 898 (1984).

M.T. Mercier *et al.*, Phys. Rev. C **33**, 1655 (1986).

B. S. Nilsen *et al.*, Phys. Rev. C **50**, 1065 (1994).

M.H. Nayfeh and M.K. Brussel, *Electricity and Magnetism*, John Wiley & Sons, New York 1985.

D. Olson *et al.*, Phys. Rev. **C24**, 1529 (1981).

M.E. Nieland and C.A. Peterson, Master Fit Users' Guide, Ames Laboratory and Iowa State University, 1985.

J.J. Sakurai, *Advanced Quantum Mechanics*, Addison- Wesley, Redwood City, CA 1967.

W.C. Schick, Jr., "Skewgaus: A Fortran Program for Fitting Peaks in Semiconductor Detector Spectra"; report for The U.S. Atomic Energy Commission of Research under contract W-7405-eng-82; Ames Laboratory, Iowa State University, Ames, Iowa: 1974.

A. Veyssière et al, Nucl. Phys. , **A159** 561 (1970).

K. Way, Nuclear Data Tables, **7**, 574 (1970).

G.D. Westfall *et al.*, Phys. Rev. C **19**, 1309 (1979).

E. J. Williams, Proc. Ray. Soc., **A139**, 163 (1933).

E. Witten, Phys. Rev. D **30**, 272 (1984).